

AD/A-007 035

MESO-SCALE AND SMALL-SCALE INTER-  
ACTIONS ON GLOBAL CLIMATE. VOLUME II.  
RADIATION TRANSPORT EFFECTS ON GLOBAL  
CLIMATE

John Schaibly

Systems, Science and Software

Prepared for:

Air Force Office of Scientific Research  
Advanced Research Projects Agency

28 February 1975

DISTRIBUTED BY:

**NTIS**

National Technical Information Service  
U. S. DEPARTMENT OF COMMERCE

UNCLASSIFIED

SECURITY CLASSIFICATION OF THIS PAGE (When Data Entered)

REPORT DOCUMENTATION PAGE		READ INSTRUCTIONS BEFORE COMPLETING FORM
1. REPORT NUMBER <b>AFOSR - TR - 75 - 0398</b>	2. GOVT ACCESSION NO.	3. RECIPIENT'S CATALOG NUMBER <b>AD/A-007035</b>
4. TITLE (and Subtitle) <b>Meso-Scale and Small-Scale Interactions on Global Climate Vol. II - Radiation Transport Effects on Global Climate</b>		5. TYPE OF REPORT & PERIOD COVERED <b>Final Report 1 Nov 1973 - 31 Dec 1974</b>
7. AUTHOR(s) <b>John Schaibly</b>		6. PERFORMING ORG. REPORT NUMBER <b>SSS-R-75-2556</b>
9. PERFORMING ORGANIZATION NAME AND ADDRESS <b>Systems, Science and Software P.O. Box 1620 La Jolla, CA 92038</b>		8. CONTRACT OR GRANT NUMBER(s) <b>F44620-74-C-0035</b>
11. CONTROLLING OFFICE NAME AND ADDRESS <b>Advanced Research Projects Agency/NMR 1400 Wilson Boulevard Arlington, VA 22209</b>		10. PROGRAM ELEMENT, PROJECT, TASK AREA & WORK UNIT NUMBERS <b>ARPA Order No. 2609 Program Code 4P10</b>
14. MONITORING AGENCY NAME & ADDRESS (if different from Controlling Office) <b>Air Force Office of Scientific Research/NP 1400 Wilson Boulevard Arlington, VA 22209</b>		12. REPORT DATE <b>28 Feb 1975</b>
		13. NUMBER OF PAGES <b>204</b>
		15. SECURITY CLASS. (of this report) <b>Unclassified</b>
16. DISTRIBUTION STATEMENT (of this Report)  <b>Approved for public release Distribution is unlimited</b>		15a. DECLASSIFICATION/DOWNGRADING SCHEDULE
17. DISTRIBUTION STATEMENT (of the abstract entered in Block 20, if different from Report)		
18. SUPPLEMENTARY NOTES		
19. KEY WORDS (Continue on reverse side if necessary and identify by block number) <b>Radiation Transport Atmospheric Scattering</b>		
20. ABSTRACT (Continue on reverse side if necessary and identify by block number) <b>This report summarizes the three-year research program at Systems, Science and Software to investigate the effects of meso-scale and small-scale interactions on global climate. The research concentrated on two areas, orographic effects on the wind patterns and effects of radiation transport on the climate. Volume I describes the orographic research and includes the theory of momentum transport due to mountain ranges, the formulation of several computer codes to calculate the effects for realistic topography and wind profiles, and the application of these codes to various problems and comparison with other</b>		

calculations as well as experimental results. Volume II describes the radiation transport research which produced a benchmark code against which more simplified models can be compared. This code, ATRAD, is characterized by high angular and frequency resolutions and by the ability to calculate radiative atmospheric heating rates taking into account molecular absorption and scattering from arbitrary distributions of aerosols and particulates.

*(continued)*

1a

## TABLE OF CONTENTS

	<u>Page</u>
ABSTRACT. . . . .	vii
1. INTRODUCTION. . . . .	.1-1
1.1 Radiative Transport Effects on Climate . . . .	.1-3
2. ATRAD THEORY. . . . .	.2-1
2.1 Assumptions. . . . .	.2-1
2.2 Basic Radiative Transfer Equations . . . . .	.2-4
2.3 Specifications of Atmospheric Structure. . . .	.2-10
2.4 Boundary Conditions. . . . .	.2-10
2.5 Transmission Functions . . . . .	.2-19
2.5.1 Exponential-Sum Fitting . . . . .	.2-24
2.5.1.1 A Global Minimization Procedure for Polynomials. . . . .	.2-28
2.5.1.2 Splitting the Polynomial . . . .	.2-34
2.5.1.3 Exponential Fits of Representa- tive Transmission Functions. . .	.2-40
2.5.1.4 Tables of Fitting Parameters . .	.2-57
2.5.2 Treatment of Overlapping Bands. . . . .	.2-58
2.6 Separation of Intensity into Solar and Diffuse Parts. . . . .	.2-59
2.7 Scattering Treatment . . . . .	.2-62
2.7.1 Rayleigh Scattering . . . . .	.2-62
2.7.2 Mie Scattering, Single Sphere . . . . .	.2-63
2.7.3 Mie Scattering, Polydispersion. . . . .	.2-66
2.7.4 Numerical Integration Over Aerosol Size Distribution. . . . .	.2-69



	<u>Page</u>
2.7.5 Phase Function Truncation . . . . .	.2-74
2.7.6 Azimuthal Integration . . . . .	.2-77
2.7.7 Renormalization of the Phase Function . . . . .	.2-78
2.7.8 Total Phase Function. . . . .	.2-82
2.7.9 Tables. . . . .	.2-83
2.8 Solution to the Radiation Transfer Equation. . . . .	.2-83
2.8.1 Layer Composition . . . . .	.2-87
2.8.2 Source Doubling . . . . .	.2-93
2.8.3 Forward and Backward Passes . . . . .	.2-101
2.8.4 Special Case of No Scattering in the Grant-Hunt Algorithm. . . . .	.2-105
2.9 Flow Diagram of ATRAD. . . . .	.2-106
3. ATRAD APPLICATIONS. . . . .	.3-1
3.1 The Mintz-Arakawa Radiation Subroutine . . . . .	.3-1
3.2 Calculations . . . . .	.3-6
3.3 Arctic Stratus Problem . . . . .	.3-21
3.3.1 Comparison of ATRAD with Experiment . . . . .	.3-21
3.3.2 Dependence of Surface Flux on Solar Ele- vation. . . . .	.3-29
3.3.3 Comparisons of ATRAD with Simpler Models. . . . .	.3-31
3.4 ATRAD Compared with Katayama Models for Clear- Sky Cases. . . . .	.3-45
3.5 ATRAD Compared with Katayama Model for Arctic Stratus Problem. . . . .	.3-70
3.5.1 Scattering in the IR. . . . .	.3-71
3.5.2 Sensitivity to Surface Temperature. . . . .	.3-73
3.5.3 Cloud Albedo. . . . .	.3-74
3.5.4 Albedo of a Cloudy Atmosphere . . . . .	.3-76
REFERENCES. . . . .	.R-1

## LIST OF FIGURES

	<u>Page</u>
2.1 ATRAD Coordinate System. . . . .	2-5
2.2 Geometry of Reflection . . . . .	2-12
2.3 Graph of $F(z)$ . . . . .	2-73
2.4 Exact $(P_{v,M})$ and Truncated $(P_{v,M}^t)$ Phase Func- tion . . . . .	2-75
2.5 Diagram of Interaction Principle . . . . .	2-86
2.6 Homogeneous Zone Composed of $2^N$ Primary Layers . .	2-94
2.7 ATRAD Code Organization, Showing the Role of the Three Auxiliary Table-Making Codes . . . . .	2-107
3.1 Test Problem Temperature Profiles. . . . .	3-7
3.2 Test Problem Water Vapor Density Profiles. . . . .	3-8
3.3 Test Problem Ozone Density Profile . . . . .	3-10
3.4 Total (Frequency-Integrated) Radiative Flux Profile from ATRAD, Problem 1. . . . .	3-12
3.5 Radiative Flux Spectrum at the Surface and at the Top of the Atmosphere from ATRAD, Problem 1. . . . .	3-14
3.6 Total (Frequency-Integrated) Radiative Flux Profile, Problem 2. . . . .	3-17
3.7 Radiative Flux Spectrum at the Surface and at the Top of the Atmosphere, Problem 2 . . . . .	3-18
3.8 Number Distribution of Arctic Stratus Clouds at Barrow . . . . .	3-25
3.9 Multiple Cloud-Ground Reflection Model of Weller .	3-32
3.10 Multiple Cloud-Ground Reflection Model . . . . .	3-36
3.11 Multiple Reflection Model which includes the Effects of Absorption and Back-Scattering . . . . .	3-38

## LIST OF TABLES

	<u>Page</u>
2.1 Results of Exponential Fitting of Transmission Functions in Five Spectral Intervals . . . . .	2-43
2.2 Coefficients and Exponents for the Exponential Fits of Transmission Functions in the Five Spectral Intervals. . . . .	2-49
2.3 Coefficients and Exponents for the Exponential Fits of Transmission Functions in the Three Spectral Intervals. . . . .	2-51
3.1 Comparison Between ATRAD and Mintz-Arakawa Fluxes and Heating Rates, Problem 1 . . . . .	3-15
3.2 Comparison Between ATRAD and Mintz-Arakawa Fluxes and Heating Rates, Problem 2 . . . . .	3-19
3.3 Comparison of Flux Measurements of Weller with Flux Predictions of ATRAD . . . . .	3-22
3.4 Actual ATRAD Atmospheric Structure used in Arctic Stratus Problem. . . . .	3-24
3.5 ATRAD Predicted Down-Fluxes at the Ground. . . . .	3-30
3.6 Ratio of the Down-Flux at the Ground to the Down-Flux at the Arctic Stratus Cloud Top . . . . .	3-34
3.7 Comparisons of ATRAD and Eq. (3.17) Predictions of Flux Ratio . . . . .	3-43
3.8a Atmospheric Profiles of Altitude, Pressure, Temperature, Water Vapor, Ozone Density, and Aerosol Density for Chad Problem. . . . .	3-46
3.8b Atmospheric Profiles of Altitude, Pressure, Temperature, Water Vapor, Ozone Density, and Aerosol Density for Bolivia Problem . . . . .	3-47
3.9 Solar Elevation, Albedo, and Surface Temperature for Chad and Bolivia Problems. . . . .	3-48
3.10 Comparison Between ATRAD and Older Katayama Model Flux Predictions for Chad and Bolivia Problems . . .	3-50

Page

- 3.11 Flux Differences and Surface Fluxes for Chad as Predicted by ATRAD with and without an Ozone Profile, and by the Newer and Older Katayama Models . . . . .3-57
- 3.12 Flux Differences and Surface Fluxes for Bolivia as Predicted by ATRAD with and without an Ozone Profile, and by the Newer and Older Katayama Models . . . . .3-58
- 3.13 Effective Water Vapor Amounts  $\text{g/cm}^2$  in Upper and Lower Levels for Chad and Bolivia, for Pressure Scaling Factors of 0.6 to 1.0 and for ATRAD. . . . .3-61
- 3.14 Flux Differences in the near-IR and 'Visible' for the Chad and Bolivia Problems. . . . .3-63
- 3.15  $2640 - 11,120 \text{ cm}^{-1}$  Down-Fluxes in  $\text{Watts/m}^2$  at the Top of the Atmosphere and at  $\sigma = 0, 1/2, \text{ and } 1$ , and Down-Flux Differences Across the Upper and Lower Levels for the Chad and Bolivia Problems . . . . .3-66
- 3.16 Predictions of Eqs. (3.28) and (3.29) for Solar Flux Differences Across Upper and Lower Layers. . . . .3-69
- 3.17 Comparison Between ATRAD Predictions for Down-Flux, Up-Flux, Net Flux, and Net Flux Differences. . . . .3-72
- 3.18 The ATRAD-Predicted Ratio of Up-Flux at the Cloud-Top to Down-Flux at the Cloud Top for Arctic Stratus Problem, for Various Values of Solar Elevation  $\theta$  and Surface Albedo  $\beta$  . . . . .3-75
- 3.19 Comparisons of Cloudy Atmospheric Albedo  $\alpha_{\text{atm}}$  as Calculated by Eq. (3.36) and by ATRAD. . . . .3-77



## ABSTRACT

This report summarizes the three-year research program at Systems, Science and Software to investigate the effects of meso-scale and small-scale interactions on global climate. The research concentrated on two areas, orographic effects on the wind patterns and effects of radiation transport on the climate. Volume I describes the orographic research and includes the theory of momentum transport due to mountain ranges, the formulation of several computer codes to calculate the effects for realistic topography and wind profiles, and the application of these codes to various problems and comparison with other calculations as well as experimental results.

Volume II describes the radiation transport research which produced a benchmark code against which more simplified models can be compared. This code, ATRAD, is characterized by high angular and frequency resolution and by the ability to calculate radiative atmospheric heating rates taking into account molecular absorption and scattering from arbitrary distributions of aerosols and particulates.

## 1. INTRODUCTION

The numerical prediction of the general circulation of the atmosphere predates most of the other applications of high speed computers to physical problems. The codes which exist at several major research centers have reached levels of considerable sophistication. These codes are used to solve time-dependent equations describing atmospheric motion in a three-dimensional representation. Parametric descriptions are included to take into account the effects of insolation, turbulent transport, and moisture.

There are two aspects of current computational capabilities, however, which have been treated rather crudely in the past, and which have been the subject of the present research program at Systems, Science and Software ( $S^3$ ): orographic effects and effects of radiative transfer on the climatology. Orographic (mountainous) effects are mesoscale phenomena, i.e., occurring on a distance scale of a few kilometers which is smaller than the typical grid size in the Global Circulation Models (GCM). Qualitatively, the effect of mountains is to transport horizontal momentum to high altitudes over the mountains and long distances down wind. This perturbation in the flow field can cause moisture to be advected to high altitudes and cloud formation is common. The clouds and moisture, on the other hand, can alter the climatic conditions over areas large compared to the mountainous source.

For the application to short period forecasts, covering the time interval shorter than a few days, the details of the atmospheric heating by solar insolation are probably not

necessary. Over longer periods of time, however, the processes which transform the solar energy into motion of the atmosphere are much more important and more sophisticated models are necessary.

The research effort described in this report has led to the development of computer codes capable of calculating the orographic effects and radiative effects in considerable detail. S<sup>3</sup> has used its extensive hydrodynamics and radiation modeling capabilities to produce codes that include descriptions of most of the physical processes which are relevant. Through test calculations the accuracy of various physical and mathematical approximations was determined, allowing simplification in the models. Finally, parameterized models have been developed for the RAND Mintz-Arakawa two-level Global Circulation Model (GCM) which provide increased accuracy in the momentum transport and radiative heating calculations at a nominal increase in computation time.

The present report is a comprehensive summary of nearly four years of research. The editors have attempted to discard the many blind alleys encountered and reported in the various semi-annual reports, and to condense the material as much as possible, but the sheer volume of useful results has required publication in two volumes. Volume I describes the work on orographic modeling, and the radiation transport work is described in Volume II.

## 1.1 RADIATIVE TRANSPORT EFFECTS ON CLIMATE

In several intensively investigated problems of atmospheric motion, the role of radiative transfer is an important one. One of these is the global circulation of the atmosphere in which short and long wave radiation form a major subsystem of the strongly interactive radiative-fluid dynamic atmospheric system. In investigations of climate the geographical and seasonal dependence of the heating of the atmosphere interacting with surface albedo and cloud cover provides the source of energy for the atmospheric circulation. Another actively investigated field of fluid dynamics in which radiation plays a role is the planetary boundary layer. Diurnal changes within this layer give rise to winds and clouds having profound influence on Man. To mention a few of the phenomena induced by the heating of the atmosphere near the ground, there are slope winds, land-sea breezes, heat island effects, and radiation and advection fogs. Finally, on the micro-scale the environment of plants and animals is largely determined by the radiation properties of their immediate surroundings.

An atmospheric radiative transfer computer code, ATRAD, has been developed, tested, and applied to the calibration of the radiative transfer subroutine of one of the climate dynamics computer codes. The code has the objective of calculating radiative fluxes of short and long wave radiation in order to determine highly accurate atmospheric heating rates. Through this formulation, which takes account of frequency and angular dependence, scattering from molecules and aerosols, and general surface boundary conditions, we have made available a radiative transfer benchmark code serving as a standard for comparison with calculations containing less comprehensive treatments.

The assumptions and physical considerations forming the basis for the ATRAD formulation are given in Section 2. Also,



given in that section are the numerical approximations in the present code. In Section 3 applications of the code to a variety of problems are presented, including comparisons with other, less accurate treatments.

## 2. ATRAD THEORY

### 2.1 ASSUMPTIONS

The fundamental assumptions involved in the formulation of the ATRAD equations are:

- (1) plane-parallel atmosphere (rather than spherical) and horizontal surface,
- (2) horizontal homogeneity,
- (3) local thermodynamic equilibrium, so that true emission is described by the Planck function,
- (4) unpolarized radiation field ,
- (5) non-refractive air (rays are not curved),
- (6) spherical aerosol scatterers of uniform composition,
- (7) point source sun (no angular width), and
- (8) multiplying together the transmissions of individual molecular constituents yields the total transmission.

Assumptions (1) and (5) are only violated for large-zenith-angle rays, and such rays make only a very small contribution to vertical fluxes.

Assumption (2) probably represents the most serious approximation in the code, one whose impact has been largely ignored in the literature. The effect of the most important form of horizontal inhomogeneity, partial cloudiness, is customarily accounted for by taking a weighted sum of clear-air and totally-cloudy fluxes,

$$F = \alpha F_{\text{cloud}} + (1-\alpha) F_{\text{clear}}$$

where  $\alpha$  is the fractional cloudiness. The only virtue of this scheme is that it reduces properly in the limits  $\alpha = 0$  and  $\alpha = 1$  and, therefore, cannot err too greatly for  $0 < \alpha < 1$ . A more reasonable scheme, in the context of ATRAD's numerical algorithm, would be to take the weighted sum of the reflection and transmission matrices of a partially cloudy zone. This difficulty could be resolved with a three-dimensional Monte Carlo code such as that of Cox and McKee,<sup>\*</sup> which should help to ascertain the relative importance of horizontal inhomogeneity and whether it is really significant for weather and climate radiation subroutines.

Assumption (3), which requires sufficiently high pressures that collisions maintain thermodynamic equilibrium in excited states, is valid below about 70 km.

Assumption (4) has been examined by several investigators, for example Howell and Jacobowitz,<sup>[1]</sup> who find that, especially in the presence of aerosols, the flux errors resulting from a polarization-independent treatment are generally less than one percent in the visible spectrum. Averaged over the whole spectrum, these errors are considerably smaller.

A standard Mie theory treatment<sup>[2]</sup> of aerosol scattering is made possible by assumption (6). Uniform composition is not essential, since layered spherical particles can be handled with some increase in computational complexity (see Kerker<sup>[3]</sup>). However, there is practically no experimental data on layered (water-sheathed, etc.) aerosol particles. Neither is sphericity essential since Mie theory has been extended to ellipsoids and circular cylinders. However, solid aerosol particles (with the exception of cirrus ice needles) are no more accurately representable as ellipsoids or

---

<sup>\*</sup>S. Cox, Colorado State University, Fort Collins, Colorado, private communication.

cylinders than as spheres. And liquid aerosol particles are very nearly spherical, although the larger ones will tend to be slightly flattened by the air flow around them. Furthermore, as Hodkinson<sup>[4]</sup> argues, randomly oriented irregular particles produce the same forward diffraction, the same scattering due to external reflection, and the same scattering due to the first refraction as equivalent spheres (spheres having the same distribution of projected area). For moderately absorbing irregular particles, this would lead to a complete equivalence of scattering patterns. Measurements of Hodkinson,<sup>[4]</sup> Ellison,<sup>[5]</sup> and Holland and Gagne<sup>[6]</sup> tend to confirm the usefulness of Mie theory (with equivalent spheres) for predicting the scattering from irregular particles into the forward hemisphere, which contains almost all the scattered photons.

The one aerosol which, by virtue of its importance to the global radiative energy budget,<sup>[7,8]</sup> should probably not be approximated as spherical is cirrus cloud. Jacobowitz<sup>[9]</sup> has computed the phase function of randomly oriented hexagonal ice cylinders, typical of cirrus, and has found that as much energy is scattered into the halo, around  $22^\circ$ , as into the main diffraction peak. This effect is entirely missed by an equivalent sphere model.

The error incurred by assumption (7), ignoring the angular width of the sun, has been estimated and found to be negligible as far as vertical fluxes are concerned.

Assumption (8), that individual transmissions are multiplicative, is firmly grounded in experiment,<sup>[11]</sup> and has virtually no detectable experimental error associated with it.



## 2.2 BASIC RADIATIVE TRANSFER EQUATIONS

The radiative transfer problem in the Earth's atmosphere reduces to the solution of the seemingly simple equation<sup>[12]</sup>

$$\frac{dI_\nu}{ds} = J_\nu - \kappa_\nu I_\nu \quad (2.1)$$

which states that the monochromatic (frequency  $\nu$ ) radiant intensity  $I_\nu$ , in traversing the element of length  $ds$ , will be augmented by sources in the amount  $J_\nu ds$  and diminished by extinction in the amount  $\kappa_\nu I_\nu ds$ . In general, the radiant intensity and  $J_\nu$ , the source function, depend on both a spatial coordinate  $\vec{r}$  and an angular coordinate (direction)  $\vec{\Omega}$  at the point  $\vec{r}$ , as well as upon the frequency  $\nu$ . The time dependence of these quantities is ignored because the radiative state of the atmosphere is established, for all practical purposes, instantaneously.  $\kappa_\nu$  is the extinction coefficient, which describes the relative depletion in the intensity of the beam,  $dI_\nu/I_\nu$ , upon traversing the element of distance  $ds$ .  $\kappa_\nu$  is in general the sum of an absorption part and a scattering part.  $J_\nu$  describes the additions made to the beam intensity along  $ds$  by thermal (Planckian) emission and by scattering.

In ATRAD's plane-parallel geometry, which is illustrated in Figure 2.1,  $\vec{r}$  is replaced by  $z$ , which is measured from the top of the atmosphere, and  $\vec{\Omega}$  is represented as usual by the spherical coordinates  $\mu = \cos\theta$  and  $\phi$ . Using Kirchhoff's Law to obtain the source function  $J_\nu$ , the radiative transfer equation (2.1) becomes in this geometry<sup>[13]</sup>

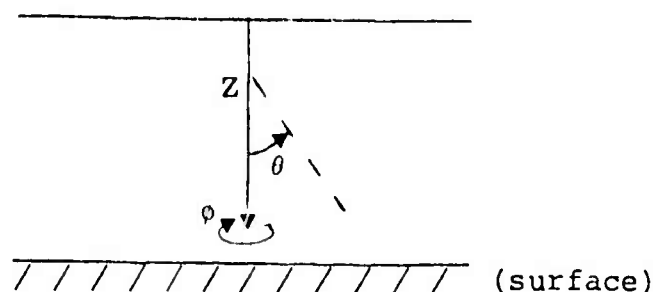


Figure 2.1 - ATRAD coordinate system

$$\mu \frac{\partial I_v}{\partial z} = \alpha'_v(z) B_v(T) + \frac{\beta_v(z)}{4\pi} \int_{4\pi} P_v(z, \vec{\Omega}, \vec{\Omega}') I_v(z, \vec{\Omega}') d\Omega' - \kappa_v(z) I_v \quad (2.2)$$

where

$\kappa_v = \alpha'_v + \beta_v =$  volume extinction coefficient,

$\alpha'_v =$  volume absorption coefficient,  $\alpha_v$ , corrected for stimulated emission (a correction usually ignored in the atmospheric radiation literature),

$$= \alpha_v \left( 1 - e^{-h\nu/kT} \right),$$

$T =$  temperature,

$\beta_v =$  volume scattering coefficient,

$B_v =$  Planck function

$$= \frac{2h\nu^3/c^2}{e^{h\nu/kT} - 1}$$

and  $P_v$  is the phase function, defined so that

$$P_v(z, \vec{\Omega}, \vec{\Omega}') \frac{d\Omega}{4\pi}$$

is the probability that a photon entering a volume element around  $z$  from direction  $\vec{\Omega}'$  will be scattered into the cone  $d\Omega$  of directions around  $\vec{\Omega}$ . Since absorption is explicitly represented in Eq. (2.2), the above probabilities must sum to one

$$\int_{4\pi} P_v(z, \vec{\Omega}, \vec{\Omega}') \frac{d\Omega}{4\pi} = 1 \quad (2.3)$$

In what follows, it is convenient to break the absorption coefficient into a "line" part and a "continuum" part,

$$\alpha'_v = \alpha_v^{\text{line}} + \alpha_v^{\text{cont}} \quad (2.4)$$

$\alpha_v^{\text{cont}}$  varies "slowly" with frequency and includes, for example, the water vapor 8-12 $\mu$  continuum and the aerosol absorption;  $\alpha_v^{\text{line}}$  is the rapidly-varying part, due to absorption lines of atmospheric constituents. Since a continuum is often due to the wings of distant lines, the separation is to a certain extent arbitrary. Therefore, we shall adopt the convention that, with the exception of aerosol absorption, continua exist only in the gaps between absorption bands.

Because a volume element in the atmosphere exhibits the same scattering pattern no matter what the direction of incidence

$\vec{\Omega}'$ , the phase function depends only on the scattering angle  $\theta_s$  between  $\vec{\Omega}$  and  $\vec{\Omega}'$ ,

$$P_v = P_v(z, \mu_s)$$

where

$$\mu_s \equiv \cos \theta_s = \mu \mu' + \sqrt{1-\mu^2} \sqrt{1-\mu'^2} \cos(\phi - \phi')$$

In order to azimuthally-average the radiation transport equation (see below), it is necessary to azimuthally-average  $P_v$ :

$$\begin{aligned} \bar{P}_v(z, \mu, \mu') &\equiv \frac{1}{2\pi} \int_0^{2\pi} P_v(z, \mu_s) d\phi \\ &= \frac{1}{2\pi} \int_0^{2\pi} P_v(z, \mu \mu' + \sqrt{1-\mu^2} \sqrt{1-\mu'^2} \cos \phi) d\phi \quad . \quad (2.5) \end{aligned}$$

The second step follows from the periodicity of the cosine. As a result,  $\bar{P}_v$  does not depend on  $\phi'$ .

For the computation of vertical fluxes and radiative heating rates, the retention of the  $\phi$ -dependence of  $I_v$  is unnecessary. It can be eliminated by  $\phi$ -averaging Eq. (2.2)

(operating on both sides with  $\frac{1}{2\pi} \int_0^{2\pi} d\phi$ ) to obtain



$$\mu \frac{\partial \bar{I}_v}{\partial z} = \alpha'_v B_v + \frac{\beta_v}{2} \int_{-1}^1 \bar{P}_v(z, \mu, \mu') \bar{I}_v(z, \mu') d\mu' - \kappa_v \bar{I}_v \quad (2.6)$$

where

$$\bar{I}_v(z, \mu) = \frac{1}{2\pi} \int_0^{2\pi} I_v(z, \mu, \phi) d\phi .$$

Knowing  $\bar{I}_v$ , the vertical flux  $F_v$  is obtained from

$$F_v(z) \equiv \int_{4\pi} \mu I_v(z, \vec{\Omega}) d\Omega = 2\pi \int_{-1}^1 \mu \bar{I}_v(z, \mu) d\mu . \quad (2.7)$$

From  $F_v$  the total (spectrally-integrated) flux  $F$  can be computed:

$$F(z) = \int_{\nu_{\min}}^{\nu_{\max}} F_v(z) d\nu$$

where  $[\nu_{\min}, \nu_{\max}]$  includes all spectral intervals in which  $F_v$  is non-negligible. From  $F$ , the radiative heating rate at level  $z$  can be calculated from

$$\frac{\partial T}{\partial t} = - \frac{1}{\rho C_p} \frac{dF}{dz} \quad (2.8)$$

where

$\rho = \rho(z)$  = air density

$C_p$  = specific heat of air at constant pressure .

Using the hydrostatic approximation, this becomes

$$\frac{\partial T}{\partial t} = - \frac{g}{C_p} \frac{dF}{dp} .$$

Rather than compute point-values of heating, ATRAD computes the average heating of a zone  $(z_i, z_{i+1})$  in terms of the boundary fluxes:

$$\begin{aligned} \left\langle \frac{\partial T}{\partial t} \right\rangle &= \frac{1}{p_{i+1} - p_i} \int_{p_i}^{p_{i+1}} \frac{\partial T}{\partial t} dp \\ &= - \frac{g}{C_p} \frac{F(z_{i+1}) - F(z_i)}{p_{i+1} - p_i} \end{aligned} \quad (2.9)$$

(the slight vertical variation of  $g$  has been ignored).

The radiative transfer equation, Eq. (2.6), is a phenomenological equation requiring input data of three different types:

- (a) atmospheric structure data
- (b) boundary condition data
- (c) absorption data for relevant atmospheric constituents.

The next three sections describe ATRAD's needs in each of these areas.

### 2.3 SPECIFICATIONS OF ATMOSPHERIC STRUCTURE

The atmospheric structure data needed to solve Eq. (2.6), with the use of Mie scattering theory for aerosols, consists of the pressure  $p$ , the temperature  $T$ , the water vapor density  $\rho_{H_2O}$ , the ozone density  $\rho_{O_3}$ , and the aerosol (including cloud) number density, size distribution, and composition. These must all be given as a function of height. The atmospheric absorbers other than water vapor and ozone are assumed to be uniformly mixed.

The details as to how the structure data are supplied to ATRAD are not given here. A variety of analytic aerosol size distributions are available as options, or the user may supply his own size distributions in card form. Similarly, a variety of aerosol refractive indices are available as options, e.g. water, ice, sea-salt, dust, etc.

### 2.4 BOUNDARY CONDITIONS

The boundary condition at the top of the atmosphere is

$$I_{\nu}(0, \mu, \phi) = S_{\nu} \delta(\vec{\Omega} - \vec{\Omega}_0) \quad \text{for} \quad \begin{array}{l} 0 < \mu \leq 1 \\ 0 \leq \phi < 2\pi \end{array}$$

where  $S_{\nu}$  is the solar flux at frequency  $\nu$  at the position of the Earth and  $\vec{\Omega}_0$  is the direction of the solar beam in ATRAD's coordinate system (Figure 2.1). Taking the  $\phi$ -average,

$$\bar{I}_{\nu}(0, \mu) = \frac{S_{\nu}}{2\pi} \delta(\mu - \mu_0) \quad 0 < \mu \leq 1 \quad (2.10)$$

$\mu_0$ , the cosine of the solar zenith angle, is calculated following the prescription of Woolf<sup>[14]</sup> from user-supplied values of latitude, longitude, day of the year, and Greenwich time. The best measurements of  $S_v$  are those of Thekaekara, et.al.,<sup>[15]</sup> which have been included in the code. (Actually, the values of

$$\int_0^\lambda S_\lambda d\lambda = \int_v^\infty S_v dv$$

are given by Thekaekara, and the code obtains from these the values

$$S_{\Delta v} = \frac{1}{\Delta v} \int_{\Delta v} S_v dv$$

for use in each frequency group  $\Delta v$ .)  $S_{\Delta v}$  is adjusted according to the earth-sun distance, which is calculated from the day of the year.

The boundary condition at the surface requires, for its complete specification, the ground temperature  $T_g$  and the bidirectional reflectivity  $\rho_v''$ . If a beam of intensity  $I_{v,inc}$  is incident on a surface from direction  $\vec{\Omega}_i$  and the resultant reflected intensity at angle  $\vec{\Omega}_r$  is  $I_{v,ref}(\vec{\Omega}_r; \vec{\Omega}_i)$ , then  $\rho_v''$  is defined such that<sup>[16]</sup> (see Figure 2.2).

$$\pi I_{v,ref}(\vec{\Omega}_r; \vec{\Omega}_i) = \rho_v''(\vec{\Omega}_i, \vec{\Omega}_r) I_{v,inc} \cos \theta_i d\Omega_i \quad (2.11)$$

By this definition,  $\rho_v''$  is of finite order, barring specular reflection, for  $I_{v,ref}$  is of differential order with respect to  $I_{v,inc}$ . In case there is a specular component of reflection, we separate  $\rho_v''$  into a diffuse part  $\rho_{v,d}''$  and a

specular part  $\rho''_{v,s}$  ,

$$\rho''_v = \rho''_{v,d} + \rho''_{v,s}$$

where

$$\rho''_{v,s}(\vec{\Omega}_i, \vec{\Omega}_r) = \frac{\pi}{\cos\theta_i} \rho'_{v,s}(\vec{\Omega}_i) \delta(\mu_i - \mu_r) \delta(\phi_i + \pi - \phi_r) \quad . \quad (2.12)$$

Some authors, for example Siegel and Howell<sup>[16]</sup>, do not include the factor of  $\pi$  in Eq. (2.11). We find it convenient because when the reflection is diffuse,  $\rho''_v$  reduces to an albedo (flux ratio), the customary measure of surface reflectivity.

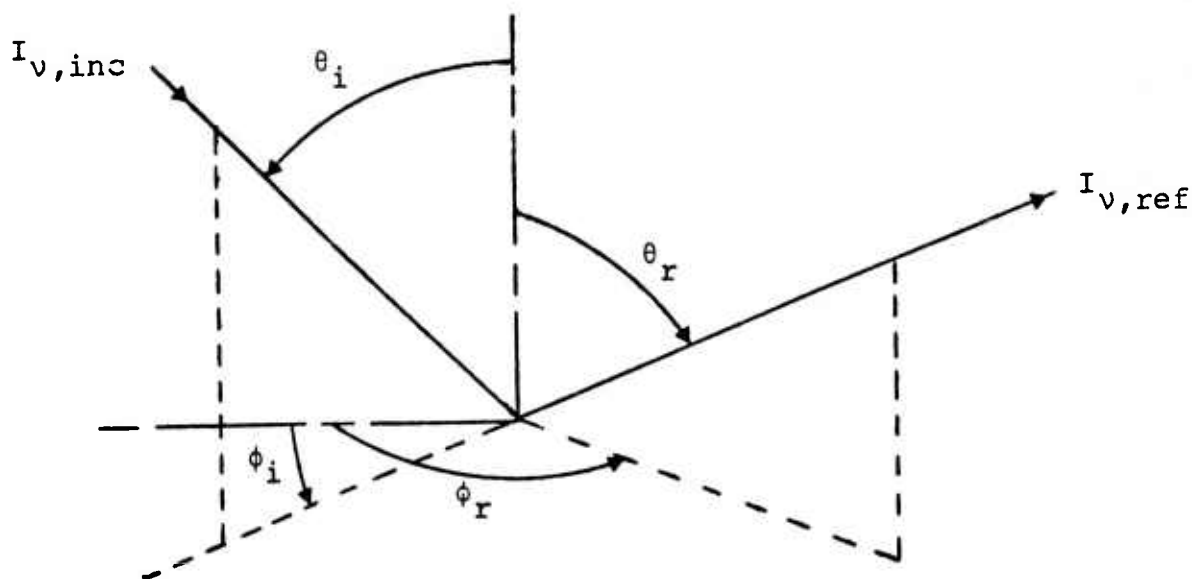


Figure 2.2. Geometry of reflection.

When radiation is incident from all  $\vec{\Omega}_i$ , the reflected intensity along  $\vec{\Omega}_r$  is, by Eq. (2.11),

$$I_{v,ref}(\vec{\Omega}_r) = \frac{1}{\pi} \int_0^{2\pi} d\phi_i \int_0^1 d\mu_i \rho_v''(\vec{\Omega}_i, \vec{\Omega}_r) I_{v,inc}(\vec{\Omega}_i) \mu_i \quad .$$

Adding on the thermal emission from the ground and phrasing the whole result in terms of the ATRAD coordinate system (Figure 2.1), the surface boundary condition becomes

$$\begin{aligned} I_v(z_0, \mu, \phi) = & \epsilon_v'(|\mu|) B_v(T_g) + \rho_{v,s}'(|\mu|) I_v(z_0, |\mu|, \phi - \pi) \\ & + \frac{1}{\pi} \int_0^{2\pi} d\phi' \int_0^1 d\mu' \rho_{v,d}''(|\mu|, \mu', \phi - \phi') I_v(z_0, \mu', \phi') \mu' \end{aligned} \quad (2.13)$$

for

$$\begin{aligned} -1 & \leq \mu < 0 \\ 0 & \leq \phi < 2\pi \end{aligned}$$

where  $z_0$  is the surface level, and  $\epsilon_v'$ , the directional emissivity, has been written as a function of angle of emission.<sup>[16]</sup> The absolute value signs on  $\mu$  in  $\epsilon_v'$ ,  $\rho_{v,s}'$ , and  $\rho_{v,d}''$  are merely because these surface properties are customarily measured or calculated with the convention  $0 \leq \theta_i, \theta_r \leq 90^\circ$ , whereas ATRAD's coordinate system takes  $0 \leq \theta_i < 90^\circ$  and  $90^\circ < \theta_r \leq 180^\circ$ .

It should be noted that, in Eq. (2.13),  $\phi$  is entirely missing from the argument list of  $\rho_{v,s}'$  and occurs in the combination  $\phi - \phi'$  in the argument list of  $\rho_{v,d}''$ . In both cases, this is justified because the surface is isotropic, that is,

its reflecting properties do not change as we rotate the coordinate system in Figure 2.2 about the vertical axis.

Taking the  $\phi$ -average of Eq. (2.13) leads to the final form of the surface boundary condition:

$$\begin{aligned} \bar{I}_v(z_0, \mu) = & \epsilon_v'(|\mu|) B_v(T_g) + \rho_{v,s}'(|\mu|) \bar{I}_v(z_0, |\mu|) \\ & + 2 \int_0^1 d\mu' \bar{\rho}_{v,d}''(|\mu|, \mu') \bar{I}_v(z_0, \mu') \mu' \end{aligned} \quad (2.14)$$

for  $-1 \leq \mu < 0$ , where

$$\begin{aligned} \bar{\rho}_{v,d}''(\mu, \mu') & \equiv \frac{1}{2\pi} \int_0^{2\pi} \rho_{v,d}''(\mu, \mu', \phi - \phi') d\phi \\ & = \frac{1}{2\pi} \int_0^{2\pi} \rho_{v,d}''(\mu, \mu', \phi) d\phi \end{aligned}$$

(the second step follows from the  $2\pi$ -periodicity of  $\rho_{v,d}''$  in its third argument).

There are three simplifications of the surface boundary condition (2.14) which are used in almost all of the other extant atmospheric radiation codes:

- (a)  $\epsilon_v' = 1$ ,  $\rho_{v,s}' = \rho_{v,d}'' = 0$ . This is used practically without exception by codes dealing with the infrared (IR) spectrum, ignoring the very real frequency- and angle-variations of  $\epsilon_v$  for natural surfaces. Furthermore, except for water, snow, and ice, the average IR emissivity

of natural surfaces is known to deviate considerably from unity.<sup>[10]</sup> Nevertheless, the mathematical consequences of using a non-unit emissivity (implying  $\rho''_{\nu,d} \neq 0$ ) are disastrous for codes using a simple quadrature of the integral transport equation, for then they can no longer frequency-average the boundary term.

- (b)  $\rho''_{\nu,d} = 0$ ,  $\rho'_{\nu,s}$  given by Fresnel formulae for reflection at a plane interface,  $\nu$  so large that  $B_{\nu}(T_g)$  is negligible. This is used primarily by codes dealing with single frequencies in the solar spectrum with water as the underlying surface.
- (c)  $\rho'_{\nu,s} = 0$ ,  $\rho''_{\nu,d} = \text{constant}$  (independent of angle of incidence and angle of reflection),  $\nu$  so large that  $B_{\nu}(T_g)$  is negligible. This is used primarily by codes dealing with single frequencies in the solar spectrum with a solid underlying surface.  $\rho''_{\nu,d}$  is the albedo, and the reflection is assumed diffuse.

We believe that it is important to include a fully general boundary condition, Eq. (2.14), as ATRAD does. Research to date suggests that such factors as the angular--and frequency--dependence of  $\epsilon'_{\nu}$  or  $\rho''_{\nu,d}$  cannot be ignored.<sup>[16,17,18,19,20,21]</sup> While data with respect to these dependences are limited, they exist in sufficient quantities to warrant comparisons with calculations using frequency and/or angular averages.



Two theoretical models of rough-surface reflectivity seem sufficiently realistic to warrant inclusion in ATRAD. The first is that for a rough water surface, in which it is assumed that the surface consists of planar elements each of which is a specular reflector. The slope distribution of the planar elements as a function of average surface wind speed can be taken from the experimental work of Cox and Munk.<sup>[17]</sup> Even with this model, the inclusion of shadowing and multiple reflections among planar elements is difficult. Therefore these effects can probably only be included approximately. Experimental measurements of sea surface bidirectional reflectivities<sup>[18]</sup> should prove useful in guiding the approximations.

The second theoretical model of rough-surface reflectivity is for land areas, and assumes that the surface consists of planar elements each of which is a diffuse reflector (of given albedo). This model is due to McStravick.<sup>[19]</sup> The slope distribution of the planar elements is presumed Gaussian. As with the first model, shadowing and multiple reflection can probably be included only approximately.

In practice, the full bidirectional reflectivity of the earth's surface is not available experimentally, nor is it likely to be available in the near future, as a function of latitude and longitude. Therefore the two theoretical models described above, particularly the water-surface model applying to so much of the earth's surface, assume special importance in filling this void. However, ATRAD also makes provision to use certain degraded forms of the bidirectional reflectivity and directional emissivity which are more readily available from experiment. These are (refer to Figure 2.2 for notation):

- (a) the directional-hemispherical reflectivity,

$$\begin{aligned}
\rho'_v(\vec{\Omega}_i) &= \frac{\text{reflected flux}}{\text{incident flux from } \vec{\Omega}_i} \\
&= \frac{\int_{\Omega} I_{v,\text{ref}}(\vec{\Omega}_r; \vec{\Omega}_i) \cos \theta_r \, d\Omega_r}{I_{v,\text{inc}}(\vec{\Omega}_i) \cos \theta_i \, d\Omega_i} \\
&= \frac{1}{\pi} \int_{\Omega} \rho''_v(\vec{\Omega}_i, \vec{\Omega}_r) \cos \theta_r \, d\Omega_r \\
&= 2 \int_0^1 \bar{\rho}''_v(\mu_r, \mu_i) \mu_r \, d\mu_r \tag{2.15}
\end{aligned}$$

(b) the hemispherical reflectivity (albedo),

$$\begin{aligned}
\rho_v &= \frac{\text{reflected flux}}{\text{incident flux}} \\
&= \frac{\int_{\Omega} \rho'_v(\vec{\Omega}_i) I_{v,\text{inc}}(\vec{\Omega}_i) \cos \theta_i \, d\Omega_i}{\int_{\Omega} I_{v,\text{inc}}(\vec{\Omega}_i) \cos \theta_i \, d\Omega_i} \tag{2.16}
\end{aligned}$$

(c) the hemispherical emissivity,

$$\begin{aligned}
\epsilon_v &= \frac{\text{emitted flux}}{\text{black body flux at } T_g} \\
&= \frac{\int_{\Omega} I_{v,\text{em}}(\vec{\Omega}) \cos \theta \, d\Omega}{\pi B_v(T_g)} \\
&= \frac{1}{\pi} \int_{\Omega} \epsilon'_v(\mu) \mu \, d\Omega \\
&= 2 \int_0^1 \epsilon'_v(\mu) \mu \, d\mu \tag{2.17}
\end{aligned}$$

The solid-angle integrals in (a)-(c) are over the upward hemisphere. Note that, by the isotropy of the surface,  $\rho'_v$  really only depends on  $\mu_i$ . Also, the above quantities are not all independent. By Kirchhoff's Law for surfaces<sup>[16]</sup>,

$$\epsilon'_v(\mu) + \rho'_v(\mu) = 1 \quad (2.18)$$

so that, if either  $\epsilon'_v$  or  $\rho'_v$  is known, the other is determined.

If only the directional-hemispherical reflectivity  $\rho'_v$  is given, nothing can be said about the angular dependence of the reflected radiation. Therefore ATRAD assumes diffuse reflection, which means  $\bar{\rho}''_v$  in Eq. (2.15) is independent of  $\mu_r$  and is equal to  $\rho'_v$ ,

$$\bar{\rho}''_v(\mu_r, \mu_i) = \rho'_v(\mu_i)$$

If  $\epsilon'_v$  rather than  $\rho'_v$  is known, Eq. (2.18) is used to obtain  $\rho'_v$ , and therefore  $\bar{\rho}''_v$ .

Note that the albedo  $\rho_v$ , Eq. (2.16), is not an intrinsic surface property but depends on the incident radiation field  $I_{v,inc}$ , a fact familiar to experimenters.<sup>[20]</sup> Only when  $\rho'_v$  is independent of angle does the albedo become independent of intensity, in which case Eq. (2.16) reduces to

$$\rho_v = \rho'_v \quad .$$

When only an albedo is available, ATRAD uses the approximation that  $\bar{\rho}''_v$  is independent of both  $\mu_r$  and  $\mu_i$ , leading to

$$\bar{\rho}''_v = \rho_v \quad .$$

To obtain the emissivity, observe that if the emission is isotropic or if  $\rho_v'$  is independent of angle, then

$$\rho_v + \epsilon_v = 1$$

from Eq. (2.18). Since the second assumption holds,  $\epsilon_v$  can be obtained from  $\rho_v$ . ATRAD then invokes the assumption of isotropic emission to obtain

$$\epsilon_v' = \epsilon_v$$

from Eq. (2.17).

A large amount of albedo data is available, [21] particularly as it relates to remote sensing from aircraft and satellites. Much more such data remains classified. However, as yet no comprehensive tabulation of albedos, bidirectional reflectivities, etc., has been incorporated into ATRAD; data for individual problems will be obtained as needed.

## 2.5 TRANSMISSION FUNCTIONS

Line-by-line absorption coefficients have been calculated and measured during the last two decades for all of the important atmospheric absorbers. However, it is computationally infeasible to use frequency groups small enough to resolve individual lines in ATRAD. Therefore, frequency-averaged absorption coefficient data in the form of transmission functions  $T_{\Delta v}$  are employed. In terms of the optical depth for line absorption

$$\tau_{v,ab}(z_1, z_2) \equiv \int_{z_1}^{z_2} \alpha_v^{(line)}(z) dz, \quad (2.19)$$

the transmission function is

$$T_{\Delta\nu}(z_1, z_2, \mu) \equiv \frac{1}{\Delta\nu} \int_{\Delta\nu} e^{-\tau_{\nu, ab}(z_1, z_2)/\mu} d\nu \quad (2.20)$$

The frequency interval  $\Delta\nu$  in general includes many lines.

The computation of transmission functions has a long history. The earliest attempts were based on band models, in which simple analytical representations of line strengths, positions, and shapes were assumed. As accurate line-by-line absorption data has become available, both from theory and experiment, transmission function computations have incorporated it. However, such detailed line-by-line transmission function computations are very expensive in terms of computer time. Considering that integration steps as small as  $0.001 \text{ cm}^{-1}$  may be required, and that the region of significant absorption extends from  $10,000 \text{ cm}^{-1}$  ( $1\mu$ ) to  $250 \text{ cm}^{-1}$  ( $40\mu$ ), with only a few gaps, the magnitude of the problem is apparent. As an example, Kyle<sup>[22]</sup> used 15 minutes of CDC 6600 time to compute transmission functions between a single pair of atmospheric levels  $z_1$  and  $z_2$ , for a single value of  $\mu$ , for the wavelength interval  $1.7\mu - 20\mu$  with  $\Delta\nu = 1 \text{ cm}^{-1}$ . Multiply this by the number of angles  $N_\mu$  and by the number of pairs of levels  $\frac{1}{2}N_z(N_z-1)$ , and the computing time to obtain a complete set of transmission functions becomes truly formidable (for 4 angles and 20 levels Kyle would require 190 hours). While it is foreseeable that, with ingenuity, such computing times could be reduced substantially, it is apparent that for the present ATRAD cannot afford to calculate transmission functions line-by-line for each new problem. Therefore, a less exact method was sought.

A rather thorough literature survey revealed numerous less exact methods for computing transmission functions. These ranged from simple parameterized band models such as Elsasser's and Goody's,<sup>[23]</sup> through more sophisticated band models such as Wyatt's,<sup>[24]</sup> to approaches such as those of Smith<sup>[25]</sup> or

McClatchey<sup>[26]</sup> involving an empirically determined function as well as empirically determined parameters. The errors in the methods of Smith or McClatchey are almost within the uncertainties in the line-by-line calculations themselves, and involve orders of magnitude less calculation. The method of McClatchey was selected for inclusion in ATRAD because of its comprehensive treatment of all known atmospheric absorbers, its accuracy, and its computational economy (only tabular interpolation is required to obtain transmissions).

The method of McClatchey, et.al., as furnished to us in subroutine LOTRAN (for LOW-resolution TRANsmission functions), contains separate values of the transmission for: (a) H<sub>2</sub>O vapor; (b) the uniformly mixed gases CO<sub>2</sub>, N<sub>2</sub>O, CH<sub>4</sub>, CO, and O<sub>2</sub>; (c) O<sub>3</sub>; (d) the H<sub>2</sub>O 8-13 $\mu$  continuum; and (e) the N<sub>2</sub>-N<sub>2</sub> 4 $\mu$  continuum. In ATRAD, the two continua (d) and (e) have been placed in subroutines separate from LOTRAN because their transmissions are simple exponentials (for small enough  $\Delta\nu$ ) and they can be added to  $\alpha_\nu$  cont, the continuum part of the absorption coefficient.

LOTRAN furnishes transmissions averaged over 20 cm<sup>-1</sup> intervals centered from 350 cm<sup>-1</sup> to 50,000 cm<sup>-1</sup>. To obtain transmissions over larger wavenumber intervals, it follows rigorously from the definition (2.20) that the 20 cm<sup>-1</sup> transmissions may be averaged; e.g.,

$$T_{400-440} = \frac{1}{2} (T_{400-420} + T_{420-440})$$

Hence ATRAD may use wavenumber intervals which are any multiple of 20 cm<sup>-1</sup>, subject to restrictions on the size of  $\Delta\nu$ . For wavenumber intervals centered below 350 cm<sup>-1</sup>, the Goody random band model for the H<sub>2</sub>O rotational band is used in LOTRAN, on the recommendation of one of McClatchey's colleagues (J.E.A. Selby). Parameters for this band model were taken from Goody,<sup>[23]</sup> Table 5.5.

In order to account for atmospheric slant paths along which the pressure  $p$  and temperature  $T$ , and therefore  $\alpha_v^{\text{line}}$ , vary--that is, in order to perform the integration in Eq. (2.19)--LOTRAN employs a version of the scaling (or effective mass) approximation. This approximation is an attempt to sum up  $z_1, z_2$  and the  $p$ - $T$  variation of  $\alpha_v^{\text{line}}(z)$  into a single argument  $u$  called the 'effective absorber amount.'  $u$  is calculated using certain a priori assumptions concerning the pressure and temperature variation of  $\alpha_v^{\text{line}}$ , with parameters chosen to best fit the real data. Following Goody, [23] the scaling approximation assumes the following decomposition of  $\alpha_v^{\text{line}}$ :

$$\alpha_v^{\text{line}}(z) = \rho_a(z) \alpha_1(v) \alpha_2(p, T)$$

(the absorber density  $\rho_a$  is separated out because the mass absorption coefficient  $\alpha_1 \alpha_2$ , an intrinsic property, is preferred by spectroscopists). The stimulated emission correction has been omitted from explicit consideration, but the effects of stimulated emission are present in the LOTRAN model insofar as certain parameters are determined, at least in part, from measured transmissions\*. The absorption optical depth (2.19) then becomes

$$\begin{aligned} \tau_{v,ab}(z_1, z_2) &= \alpha_1(v) \int_{z_1}^{z_2} \rho_a(z) \alpha_2(p, T) dz \\ &= k_v u(z_1, z_2) \end{aligned} \quad (2.21)$$

---

\*McClatchey, private communication.

where

$$k_v = \alpha_1(v) \alpha_2(p_0, T_0)$$

$$u(z_1, z_2) = \int_{z_1}^{z_2} \rho_a(z) \frac{\alpha_2(p, T)}{\alpha_2(p_0, T_0)} dz \quad (2.22)$$

and  $p_0$  and  $T_0$  are taken in LOTRAN as STP (1 atm., 273°K).  $u$  is the equivalent absorber amount on the vertical path between  $z_1$  and  $z_2$ . The further assumption is then made that  $\alpha_2$  has the form

$$\alpha_2(p, T) = A p^{\gamma_1} T^{\gamma_2}$$

Different values of  $\gamma_1$ , chosen to give a best fit to line-by-line transmissions, are used in LOTRAN for each category of absorber (a)-(e).

Unfortunately, because of lack of good data on line strengths as a function of temperature, it has not been possible to obtain best values of  $\gamma_2$  in the same way. An attempt has been made to include the temperature dependence of the line half-width by using  $p/T^{1/2}$  instead of  $p$ , so that at present  $\gamma_2 = -\gamma_1/2$ , but it is not at all certain that this leads to less error nor that  $T^{-1/2}$  is indeed the correct temperature dependence of the half-width. A prescription for putting temperature dependence into  $T_{\Delta v}$  has been proposed by Kondratyev and Timofeev.<sup>[27]</sup> These authors claim that transmission errors of up to .1 - .2 may result if temperature dependence is not accounted for, even if one uses the Curtis-Godson approximation instead of scaling. Therefore more work is needed on this question.



Many IR radiative transfer studies employ the Curtis-Godson approximation (see Armstrong<sup>[28]</sup> for an excellent discussion) rather than the scaling approximation. Very few comparisons have been made, however, of Curtis-Godson and scaling with exact calculations. Two such comparisons are that of Kondratyev and Timofeev, discussed in the last paragraph, and that of Zdunkowski and Raymond.<sup>[29]</sup> The first concludes that Curtis-Godson and scaling incur comparable errors. The second concludes that, while Curtis-Godson has the edge in accuracy, the scaling approximation is accurate to at least two decimal places for a wide range of path lengths. Thus, it appears to be justified to use the scaling approximation, especially for applications such as the present one in which errors in any one frequency interval are mitigated by the integration over all frequencies.

#### 2.5.1 Exponential-Sum Fitting

The method of Cantor and Evans<sup>[30]</sup> for exponential-sum fitting is now incorporated into ATRAD, although numerous modifications and simplifications have been introduced in adapting the method to the fitting of transmission functions. The method is briefly outlined in the following paragraphs.

We desire to fit a transmission function  $T_{\Delta v}(u)$ , whose values  $T_{\Delta v}(u_n)$  are given at a set of points

$$0 = u_1 < u_2 < \dots < u_N ,$$

with a positively-weighted sum of exponentials,

$$T_{\Delta v}(u) \approx \sum_{i=1}^M a_i e^{-k_i u} , \quad a_i > 0$$

The fit is to be best in the least-squares sense, that is, it is to be such that the residual

$$R = \sum_{n=1}^N W_n \left[ T_{\Delta v}(u_n) - \sum_{i=1}^M a_i e^{-k_i u_n} \right]^2$$

is minimized. The quantities  $W_n$  are positive weights which may be assigned arbitrarily. In order to ensure that small and large values of the transmission receive equal treatment, the weights have been taken as

$$W_n = 1/[T_{\Delta v}(u_n)]^2$$

so that  $R$  is in fact a sum of squared relative errors.

The  $u_n$ 's are selected to be equally spaced,

$$u_n = (n-1)\Delta u .$$

Then  $R$  may be written

$$R = \sum_{n=1}^N W_n \left[ T_{\Delta v}(u_n) - \sum_{i=1}^M a_i \theta_i^{n-1} \right]^2$$

where

$$\theta_i = e^{-k_i \Delta u}$$

Let us presume the following ordering of the  $\theta_i$ 's:

$$0 \leq \theta_1 < \theta_2 < \dots < \theta_M \leq 1$$

The problem of minimizing  $R$  is partly linear (finding  $a_1, \dots, a_M$ ) and partly nonlinear (finding  $\theta_1, \dots, \theta_M$ ). The algorithm which we shall describe below treats the linear and nonlinear parts of the problem separately, although we shall see that there is some coupling.

Given a set of  $\theta_1, \dots, \theta_M$ , we shall call the procedure of finding the  $a_1, \dots, a_M$  which minimize  $R$  with no constraints "solving the linear problem." Since the  $a_i$ 's are unconstrained, solving the linear problem may produce one or more negative  $a_i$ 's.

The extreme (and well-documented) ill-conditioning of the linear problem is side-stepped, as far as the calculation of the residual is concerned, by the use of divided differences, which is made possible by the use of equally-spaced  $u_n$ 's. During the iteration between linear and non-linear problems, the  $a_i$  are of importance only in determining which exponential factors  $\theta_i$  are to be dropped because of a negative coefficient.

To find the best  $\theta_i$ 's we proceed iteratively. Imagine that to the approximant

$$\sum_{i=1}^m a_i \theta_i^{n-1}, \quad a_i > 0$$

we add a new term with exponential factor  $\theta$  and coefficient  $a$ . We want to see how the residual changes as we increase  $a$  from zero; therefore, we evaluate the slope of  $R$  at  $a=0$ :

$$\left\{ \frac{d}{da} \sum_{n=1}^N w_n \left[ T_{\Delta v}(u_n) - \sum_{i=1}^m a_i \theta_i^{n-1} - a \theta^{n-1} \right]^2 \right\}_{a=0}$$

$$= -2 \sum_{n=1}^N w_n \left[ T_{\Delta v}(u_n) - \sum_{i=1}^m a_i \theta_i^{n-1} \right] \theta^{n-1} \quad (2.23)$$

which is simply a polynomial in  $\theta$ . Since we want to minimize the sum of squares, we pick  $\theta$  so that this expression is as negative as possible (if it is never negative for  $0 \leq \theta \leq 1$ , we are already at a best fit). In other words, we find the absolute minimum of the polynomial in (2.23) over  $0 \leq \theta \leq 1$ . This search was originally done by simply partitioning  $[0,1]$  into a large number of points ( $\sim 1,000$ ) and finding the absolute minimum over that set of points. This kind of search proved to be quite expensive computationally, however, since it required evaluating an  $(N-1)^{\text{st}}$  degree polynomial ( $N \sim 15-50$ ) at more than 1,000 points, for each iteration of the fitting process, for each molecular species, in every frequency level. Therefore, the search has been improved by taking into account the third derivative of the polynomial.

## 2.5.1.1 A Global Minimization Procedure for Polynomials

The problem is to find the absolute minimum of  $P(\theta)$  for  $0 \leq \theta \leq 1$ . The method which we shall give can, of course, be generalized to an arbitrary interval  $[a,b]$ , and it applies to any function  $P(\theta)$  which can be decomposed,

$$P(\theta) = P^+(\theta) - P^-(\theta) \quad (2.24)$$

into the difference of two functions  $P^+$  and  $P^-$  with monotone non-decreasing second derivatives on  $[a,b]$ . An algorithm for performing this decomposition for a polynomial is given in Section 2.5.1.2. Such a decomposition is, of course, not unique, since one can add any function with positive third derivative to both  $P^+$  and  $P^-$ . Nevertheless, because the efficiency of the procedure depends on the extent to which  $\left| \frac{d^2 P^+}{d\theta^2} + \frac{d^2 P^-}{d\theta^2} \right|$  exceeds  $|P'''(\theta)|$  on  $[0,1]$ , not all decompositions are equally useful. The one that has been selected is quite sophisticated because a simpler one proved inadequate to produce rapid convergence to the minimum.

The algorithm is based on bounding properties of certain quadratic approximants to  $P^+(\theta)$  and  $P^-(\theta)$ . Consider first the quadratic  $Q^+(\theta)$  which matches  $P^+(\theta)$  at  $\theta_1$  and  $\theta_2$  ( $0 \leq \theta_1 < \theta_2 \leq 1$ ) and which matches the derivative of  $P^+(\theta)$  at  $\theta_2$ :

$$Q^+(\theta_1) = P^+(\theta_1) \quad ,$$

$$Q^+(\theta_2) = P^+(\theta_2) \quad ,$$

ar .

$$\frac{dQ^+}{d\theta}(\theta_2) = \frac{dP^+}{d\theta}(\theta_2) .$$

By construction of  $P^+$  ,

$$\frac{d^3P^+}{d\theta^3} \geq 0 \quad \text{for } \theta \in [0,1] .$$

The error in the approximation

$$\Delta(\theta) = P^+(\theta) - Q^+(\theta)$$

therefore, has the properties

$$\Delta'''(\theta) \geq 0 , \quad \theta \in [\theta_1, \theta_2] ,$$

$$\Delta(\theta_1) = \Delta(\theta_2) = \Delta'(\theta_2) = 0 .$$

Based on these properties, a proof is now given that  $\Delta \geq 0$  throughout the interval  $[\theta_1, \theta_2]$  . By Rolle's theorem, because  $\Delta(\theta_1) = \Delta(\theta_2) = 0$  , there is a point  $\bar{\theta} \in (\theta_1, \theta_2)$  such that  $\Delta'(\bar{\theta}) = 0$  . By Taylor's theorem, we may expand  $\Delta'(\theta)$  about  $\bar{\theta}$  as follows:

$$\Delta'(\theta) = \Delta''(\bar{\theta})(\theta - \bar{\theta}) + \frac{1}{2}\Delta'''(\xi(\theta))(\theta - \bar{\theta})^2 \quad (2.25)$$

where  $\xi(\theta)$  is a point between  $\theta$  and  $\bar{\theta}$ . Evaluating this at  $\theta = \theta_2$  ,

$$0 = \Delta''(\bar{\theta})(\theta_2 - \bar{\theta}) + \frac{1}{2}\Delta'''(\xi(\theta_2))(\theta_2 - \bar{\theta})^2$$

Since the second term of this expression is non-negative, it follows that

$$\Delta''(\bar{\theta}) \leq 0 \quad .$$

The case  $\Delta''(\bar{\theta}) = 0$  is only possible when  $P^+(\theta)$  is quadratic, for then by Equation (2.25)  $\Delta'(\theta) \geq 0$  which is irreconcilable with  $\Delta(\theta_1) = \Delta(\theta_2) = 0$  unless  $\Delta(\theta) \equiv 0$ . Ignoring the trivial case when  $P^+$  is quadratic, then, we have

$$\Delta''(\bar{\theta}) < 0$$

so that  $\bar{\theta}$  is a local maximum. Hence, there are no local minima in  $(\theta_1, \theta_2)$  and so  $\Delta(\theta)$  must attain its minimum on  $[\theta_1, \theta_2]$  at an endpoint,

$$\Delta(\theta) \geq \min[\Delta(\theta_1), \Delta(\theta_2)] = 0 \quad \text{on} \quad [\theta_1, \theta_2] \quad .$$

Hence it has been proven that  $Q^+(\theta)$  forms a lower bound for  $P^+(\theta)$  on the whole interval  $[\theta_1, \theta_2]$ ,

$$Q^+(\theta) \leq P^+(\theta) \quad , \quad \theta \in [\theta_1, \theta_2] \quad .$$

A similar proof will establish that if the quadratic  $Q^-(\theta)$  is chosen such that

$$Q^-(\theta_1) = P^-(\theta_1) \quad ,$$

$$Q^-(\theta_2) = P^-(\theta_2) ,$$

and

$$\frac{dQ^-}{d\theta}(\theta_1) = \frac{dP^-}{d\theta}(\theta_1) .$$

then  $Q^-(\theta)$  forms an upper bound for  $P^-(\theta)$  ,

$$Q^-(\theta) \geq P^-(\theta) , \quad \theta \in [\theta_1, \theta_2] .$$

Clearly, then,  $Q = Q^+ - Q^-$  forms a lower bound for  $P$ ,

$$Q(\theta) = Q^+(\theta) - Q^-(\theta) \leq P^+(\theta) - P^-(\theta) = P(\theta)$$

on  $[\theta_1, \theta_2]$  . The minimization algorithm rests on this property.

Let us now trace through a single iterative step of the minimization algorithm. Presume that the original interval  $[0,1]$  on which the minimum of  $P(\theta)$  is desired has been divided into subintervals  $[\theta_1, \theta_2], [\theta_3, \theta_4], \dots, [\theta_{2N-1}, \theta_{2N}]$  which are the remaining candidates to contain the minimum. The ordering of these intervals is such that if  $Q_i(\theta)$  is the quadratic approximant of the type defined above for the interval  $[\theta_{2i-1}, \theta_{2i}]$ , and

$$q_i = \min_{\theta \in [\theta_{2i-1}, \theta_{2i}]} Q_i(\theta)$$

then

$$q_1 \leq q_2 \leq q_3 \dots \leq q_N .$$



In other words, the intervals are ordered according to the minima of their quadratic bounds. Since the quadratic bound in the first interval  $[\theta_1, \theta_2]$  dips lowest, this interval is regarded as the most likely candidate to contain the minimum. Let  $y_1$  be the position at which  $Q_1(\theta)$  attains its minimum, that is,

$$Q_1(y_1) = q_1$$

Divide  $[\theta_1, \theta_2]$  into two new intervals  $[\theta_1, y_1]$  and  $[y_1, \theta_2]$ , establish quadratic bounds separately for each of the new intervals, and insert the new intervals into the candidate stack based on their corresponding  $q$ 's. Drop the old interval  $[\theta_1, \theta_2]$ , and drop either of the two new intervals if its quadratic bound: (a) arches upward (has negative curvature) rather than dipping downward, or (b) does not have a local minimum within the interval. Finally, drop any intervals  $k$  for which

$$q_k \geq \min_{1 \leq j \leq 2N} P(\theta_j) \quad (2.26)$$

since in such intervals  $P$  is bounded above an already-known value of the polynomial. (The latter criterion for interval-dropping is particularly simple when the intervals are  $q$ -ordered; for if we begin our search at  $q_1$ , and  $q_K$  is the first  $q$  such that (2.26) is satisfied, then it is also satisfied for  $q_{K+1}, q_{K+2}, \dots$ )

The iteration is initialized by  $N = 1$ ,  $[\theta_1, \theta_2] = [0, 1]$ . It terminates when any one of the following convergence criteria is satisfied:

- (1) after any interval-dropping operation, only one interval remains in the candidate stack;
- (2) more than a pre-set number of iterations has been performed;
- (3) the sum of the number of iterations performed and the number of remaining intervals in the candidate stack exceeds a certain constant;
- (4)  $P(y_1) < 0$  and  $q_1/P(y_1) < \epsilon$  for some  $\epsilon \approx 1$  (we currently use  $\epsilon = 1.01$ ).

The reasons for criteria (1) and (2) are fairly obvious. The third criterion was based on the idea that as the number of iterations increases, fewer and fewer intervals should remain in the candidate stack if the algorithm is functioning properly. The fourth criterion has been specialized to the exponential fitting application because we require the polynomial minimum to be negative, but the idea behind it, that we are close to the minimum when the quadratic bound in the leading interval closely approximates the polynomial, is general. In practice, surprisingly, it is usually criterion (1) which terminates the iteration which means that the interval-dropping feature is very effective.

Another version of this algorithm was also developed which required no derivative evaluations of  $P(\theta)$  except at the endpoints  $\theta = 0$  and  $\theta = 1$ , but it proved to be somewhat less accurate and efficient than the present version and it also necessitated considerably more complex logic (especially with regard to interval-dropping). It was based on the fact that the quadratic  $Q(\theta)$  which matches any function with non-negative third derivative  $f(\theta)$  at three points

$$0 \leq \theta_1 < \theta_2 < \theta_3 \leq 1,$$

$$Q(\theta_i) = f(\theta_i) \quad (i = 1, 2, 3)$$

exhibits the "under-over" property,

$$Q(\theta) \leq f(\theta) \quad \text{in } [\theta_1, \theta_2] \quad ,$$

and

$$Q(\theta) \geq f(\theta) \quad \text{in } [\theta_2, \theta_3] \quad .$$

Hence by fitting  $P^+$  by  $Q^+$  at  $\theta_2 < \theta_3 < \theta_4$  and  $P^-$  by  $Q^-$  at  $\theta_1 < \theta_2 < \theta_3$ , we have:

$$Q^+ - Q^- \leq P^+ - P^- = P \quad \text{in } [\theta_2, \theta_3] \quad .$$

The remainder of the algorithm is then similar to that described above.

Convergence of the algorithm can be proved; however, the proof will not be given here.

#### 2.5.1.2 Splitting the Polynomial

The crucial step in the minimization algorithm of Section 2.5.1.1 involves splitting  $P(\theta)$  into the difference of two polynomials:

$$P(\theta) = P^+(\theta) - P^-(\theta)$$

with non-negative third derivatives,

$$\frac{d^3 P^+}{d\theta^3} \geq 0 \quad \text{for } \theta \in [0, 1] \quad .$$

The algorithm which we use to accomplish this splitting will be illustrated by actually decomposing several sample polynomials.

Suppose that  $D(\theta) = P'''(\theta)$ . Then we want to decompose  $D(\theta)$  into a difference:

$$D(\theta) = D^+(\theta) - D^-(\theta)$$

such that

$$D^{\pm}(\theta) \geq 0 \quad \text{for } \theta \in [0,1] \quad .$$

In order to split  $D(\theta)$  into positive ( $D^+$ ) and negative ( $D^-$ ) parts, we shall make use of the elementary observation that:

$$\theta^m \leq \theta^n \quad \text{when } m > n \quad \text{and } \theta \in [0,1] \quad . \quad (2.27)$$

Then if we have, for example, the pair of terms

$$3\theta^3 - 5\theta^5$$

we can take the part  $-3\theta^5$  of the negative term and include it with the positive term,

$$3\theta^3 - 3\theta^5$$

and still have an expression which is non-negative on  $0 \leq \theta \leq 1$ . For this simple example, then,

$$D^+(\theta) = 3\theta^3 - 3\theta^5 \quad ,$$

and

$$D^-(\theta) = 2\theta^5 \quad .$$

Proceeding to a more complex example, consider the quadratic:

$$D(\theta) = 1 - \theta - \theta^2 \quad .$$

Divide  $D(\theta)$  into blocks in each of which the coefficients are mono-signed:

$$\underbrace{1}_{\text{block 1}} \quad \underbrace{-\theta - \theta^2}_{\text{block 2}}$$

The second block's coefficients are multiplied by a constant such that their sum equals the negative of the coefficient sum for the first block:

$$1 - \frac{1}{2}\theta - \frac{1}{2}\theta^2 \quad . \quad (2.28)$$

This expression is then non-negative by the property (2.27), and furthermore there are no more coefficient blocks to process. Note that the expression (2.28) vanishes at  $\theta = 1$ , a property which we build into it; therefore, it may be factored,

$$(1 - \theta) \left(1 + \frac{1}{2}\theta\right) \quad .$$

Since the second factor is strictly positive, we are finished (in the next example this will not be so). The splitting is:

$$D^+(\theta) = 1 - \frac{1}{2}\theta - \frac{1}{2}\theta^2 \quad ,$$

and

$$D^-(\theta) = \frac{1}{2}\theta + \frac{1}{2}\theta^2 \quad .$$

An example with an odd number of mono-signed blocks introduces the further complications of: (a) keeping track of 'remainders', and (b) performing a second blocking operation on what is left after the first factor of  $(1 - \theta)$  is removed. Consider:

$$D(\theta) = 2 - 7\theta + 6\theta^2 \quad .$$

The mono-signed blocks are merely single terms here. We can take the part  $-2\theta$  of the second term and include it with the first term to yield:

$$2 - 2\theta - 5\theta + 6\theta^2 \quad .$$

The first two terms now form a non-negative expression. By dividing further,

$$2 - 2\theta - 5\theta + 5\theta^2 + \theta^2 \quad ,$$

the second two terms can be made into a non-positive expression. The extra  $\theta^2$  which is left over has no terms to match with it and hence is called a 'remainder.' All remainders are strictly non-negative or non-positive. They are shunted off into a 'remainder table' during the blocking-factorization process, and each repetition of this process creates (in general) a new remainder for the table. After all possible blocking-factorization processes have been done, the remainders are re-assembled into either  $D^+$  or  $D^-$ , depending on their sign. As a shorthand notation, we shall keep the remainders to the right of the polynomial, so for our current example:

$$2 - 2\theta - 5\theta + 5\theta^2 \qquad \theta^2$$

Factoring,

$$(1 - \theta) (2 - 5\theta) \qquad \theta^2$$

Now we block and separate the second factor in the same fashion:

$$(1 - \theta) (2 - 2\theta - 3\theta) \qquad \theta^2$$

Shunting off the remainder,

$$(1 - \theta)(2 - 2\theta) \qquad \theta^2, -3\theta(1 - \theta).$$

Now we are finished, since the second factor can be blocked and separated no further. Re-assembling the positive and negative parts,

$$D^+ = (1 - \theta)(2 - 2\theta) + \theta^2 = 2 - 4\theta + 3\theta^2,$$

and

$$D^- = -3\theta(1 - \theta) = -3\theta + 3\theta^2.$$

As a final example, consider:

$$\underbrace{1}_1 - \underbrace{2\theta - \theta^2}_2 + \underbrace{3\theta^3}_3.$$

The polynomial is separated into three mono-signed blocks as indicated. Since the largest negative value of the second block (at  $\theta = 1$ ) is  $-3$ , we can take  $\frac{1}{3}$  of the second block and adjoin it to the first block and still have a non-negative first block:

$$\underbrace{1 - \frac{2}{3}\theta - \frac{1}{3}\theta^2}_1 - \underbrace{\frac{4}{3}\theta - \frac{2}{3}\theta^2}_2 + \underbrace{3\theta^3}_3$$

Since the largest negative value of block 2 is now  $-2$ , we can adjoin  $\frac{2}{3}$  of block 3 to it and still have a non-positive second block:

$$\underbrace{1 - \frac{2}{3}\theta - \frac{1}{3}\theta^2}_1 - \underbrace{\frac{4}{3}\theta - \frac{2}{3}\theta^2 + 2\theta^3}_2 + \underbrace{\theta^3}_3$$

Block 3 now has nothing to match with it, and so is placed in the remainder table.  $(1 - \theta)$  is factored out of blocks 1 and 2:

$$(1 - \theta) \left[ \underbrace{1 + \frac{1}{3}\theta}_1 - \underbrace{\left(\frac{4}{3}\theta + 2\theta^2\right)}_2 \right] \theta^3$$

We now have new blocks 1 and 2, as indicated, and the whole process begins again (note that the  $\frac{1}{3}\theta$  and  $-\frac{4}{3}\theta$  are not combined - this is in order to avoid doing the actual factorization in the computational implementation of this method). The value of blocks 1 and 2 at  $\theta = 1$  are  $\frac{4}{3}$  and  $\frac{10}{3}$ , respectively, so we can adjoin  $\frac{4}{10}$  of block 2 to block 1 and still have a non-negative first block:

$$(1 - \theta) \left[ \underbrace{1 + \frac{1}{3}\theta - \frac{4}{10}\left(\frac{4}{3}\theta + 2\theta^2\right)}_1 - \underbrace{\frac{6}{10}\left(\frac{4}{3}\theta + 2\theta^2\right)}_2 \right] \theta^3$$

Block 2 has nothing to match with it, and so is added to the remainder table. Another  $(1 - \theta)$  is factored out of block 1, to yield:

$$(1 - \theta)^2 \left( 1 + \frac{8}{10}\theta \right) \theta^3, - \frac{6}{10}(1 - \theta) \left( \frac{4}{3}\theta + 2\theta^2 \right)$$

The factor multiplying  $(1 - \theta)^2$  is positive, so we are finished. We may therefore identify:

$$D^+ = (1 - \theta)^2 \left( 1 + \frac{8}{10}\theta \right) + \theta^3$$

$$= 1 - 1.2\theta - 0.6\theta^2 + 1.8\theta^3,$$

and

$$D^- = \frac{6}{10}(1 - \theta) \left( \frac{4}{3}\theta + 2\theta^2 \right) = 0.8\theta + 0.4\theta^2 - 1.2\theta^3.$$



As noted above, the computational implementation of this algorithm avoids doing the actual factorizations involving  $(1 - \theta)$  by noting that what we really want out of the factor multiplying  $(1 - \theta)^n$  for each  $n$  is the value of each of its blocks at  $\theta = 1$ . This can be simply related to the  $n^{\text{th}}$  derivative of blocks of the 'reduced' polynomial (the polynomial with remainders removed) at  $\theta = 1$ . Therefore, these derivatives are calculated instead of the factorizations. This saves a substantial amount of computer time.

### 2.5.1.3 Exponential Fits of Representative Transmission Functions

In order to illustrate the type of exponential fits to transmission functions which are generated, sample calculations are shown in Tables 2.1 to 2.3 for the five frequency intervals  $180 - 240 \text{ cm}^{-1}$  (far-infrared water vapor rotation band),  $720 - 740 \text{ cm}^{-1}$  ( $\text{CO}_2$   $15\mu$  band),  $800 - 840 \text{ cm}^{-1}$  (8 -  $12\mu$  "window"),  $5440 - 5760 \text{ cm}^{-1}$  (near-infrared  $\Omega$ -band of water vapor), and  $32000 - 33000 \text{ cm}^{-1}$  (Huggins band of ozone). These intervals are representative of the parts of the spectrum in which they lie, and will serve to point up peculiarities of the fitting process. Table 2.1 contains the values  $T_{\Delta v}(n\Delta u)$ ,  $n = 0, 1, 2, \dots, n_t$ , of the transmission function to which the exponential sum

$$E_{\Delta v}(u) = \sum a_i e^{-k_i u}$$

is to be fitted, the corresponding values  $E_{\Delta v}(n\Delta u)$ , the percent difference between  $E_{\Delta v}$  and  $T_{\Delta v}$ , and the coefficients  $a_i$  and exponents  $k_i$  resulting from the fitting. Tables 2.2 and 2.3 illustrate the effects of changing certain fitting parameters, and contain only coefficients  $a_i$  and exponents  $k_i$ .

The range of transmission values,  $1.0 - T_{\Delta\nu}(n_t \Delta u)$ , used in the tables is not fixed, but depends on the maximum estimated effective amount  $u_{\max}^*$  of each absorber which could possibly be encountered along a slant path making an angle of  $80^\circ$  with the zenith. (Actually, maximum  $H_2O$ ,  $CO_2$ , and  $O_3$  amounts have been taken to be twice the current values in order that our exponential fits might be applicable to changed future or past climatic conditions.) Thus, for example, in the  $800 - 840 \text{ cm}^{-1}$  case of Table 2.1(c), the range of water vapor transmission fitted is 0.775 to 1.0 because  $T_{\Delta\nu}(u_{\max}^*) = 0.775$  for water vapor in this spectral interval. At the other extreme are spectral intervals such as  $180 - 240 \text{ cm}^{-1}$  (see Table 2.1(a)) for which  $T_{\Delta\nu}(u_{\max}^*)$  is orders of magnitude below 0.001, the smallest transmission predictable with McClatchey's scheme<sup>[26]</sup> (which sets any transmission below 0.001 to zero.) Even should we manage to extend the transmission data below 0.001, however, it would not be desirable for two reasons connected with the numerics of fitting. First, because the fitting scheme takes equal steps  $\Delta u$  of absorber amount between the transmission data points, fitting to transmission ranges even as large as 0.001 - 1.0 results in taking many data points below 0.1 and relatively few between 1.0 and 0.1, so that the transmission function is inadequately resolved in 0.1 - 1.0 and the fit is relatively poor there. Secondly, the fitting algorithm becomes unacceptably poor if more than about 125 data points are used, so that increasing the resolution in 0.1 - 1.0 by taking a larger  $n_t$  is also unfeasible. We have temporarily solved this problem by putting a lower bound  $Tr_{\min}$  (usually 0.005 or 0.01) on the transmission data actually fitted. The variation of the fit with  $Tr_{\min}$  will be discussed below.

Evans\* believes that we can relax the equal  $\Delta u$  restriction by taking  $M$  steps of  $\Delta u$  (starting at  $u = 0$ ), then  $M$  steps of  $2\Delta u$ , then  $M$  steps of  $4\Delta u$ , etc., where  $M$  is the maximum number of terms we expect the exponential fit to contain ( $M = 20$  for the band model we use in the far IR,  $M = 8$  for McClatchey's transmission data). This involves some rather extensive code modifications, however, and has not been done because of more pressing problems. Once done, it would eliminate the problem of adequately resolving  $T_{\Delta u}(u)$  over its full range of variation.

The number of values  $n_t$  of the transmission which are used for fitting is made a function of the smallest transmission value  $t_{\min} = \max[T_{\Delta u}(u_{\max}^*), T_{r_{\min}}]$ :

$$n_t = t_{\min} n_{\min} + (1 - t_{\min}) n_{\max}$$

where  $n_{\min} = 5$  for Tables 2.1-2.3 and  $n_{\max} = 40$  for Table 2.1 and 80 for Tables 2.2-2.3. This leads to computational savings when  $t_{\min}$  is near unity and assures that a full  $n_{\max}$  points are used when  $t_{\min}$  is near zero. The linear nature of this formula is not optimal, however, for it leads to unnecessarily large values of  $n_t$  when  $t_{\min} \in [0.1, 0.9]$ . Further study is needed.

Tables 2.1 - 2.3 contain information about both the underlying line structure in each spectral interval and about the nature of the fitting process. We begin by comparing the various tables as regards the fitting process. In the far-IR spectral interval  $180 - 240 \text{ cm}^{-1}$ , the transmission data are supplied by a Goody random band model (which is used for  $\nu < 340 \text{ cm}^{-1}$  in ATRAD); for the other spectral intervals, the tabular transmission data of McClatchey are used. Because

---

\* Private communication.

Table 2.1 Results of exponential fitting of transmission functions in five spectral intervals: 180 - 240  $\text{cm}^{-1}$ ; 720 - 740  $\text{cm}^{-1}$ ; 800 - 840  $\text{cm}^{-1}$ ; 5440 - 5760  $\text{cm}^{-1}$ ; 32000 - 33000  $\text{cm}^{-1}$ . ( $n_{\text{max}} = 40$ ,  $T_{\text{min}} = 0.01$ ) Exponent units:  $\text{H}_2\text{O}$ ,  $\text{cm}^2/\text{g}$ ;  $\text{CO}_2$ ,  $\text{km}^{-1}$ ;  $\text{O}_3$ ,  $(\text{atm-cm})^{-1}$ .

(a) 180 - 240  $\text{cm}^{-1}$

TRANSMISSION FCN EXPONENTIAL APPROX WATER VAPOR PERCENT ERROR

1	1.0000000000	9.9999999999	-5.9634646-06
2	4.5531495-01	4.5531494-01	-3.5454414-06
3	3.3211003-01	3.3211002-01	-4.6737652-06
4	2.6232530-01	2.6232529-01	-2.3669389-06
5	2.1562433-01	2.1562432-01	-1.5822357-06
6	1.8221181-01	1.8221180-01	-2.5556044-06
7	1.5660044-01	1.5660043-01	-1.0898888-06
8	1.3654988-01	1.3654988-01	-1.1367306-06
9	1.2030999-01	1.2030999-01	-1.5482048-06
10	1.0693280-01	1.0693280-01	-1.3064129-06
11	9.5737230-02	9.5737230-02	-1.6213173-07
12	8.6244479-02	8.6244479-02	-7.1990894-07
13	7.8107098-02	7.8107098-02	-1.6679130-06
14	7.1066311-02	7.1066310-02	-1.7473307-06
15	6.4925155-02	6.4925156-02	2.9884493-07
16	5.9109222-02	5.9109222-02	-6.5184791-08
17	5.413307-02	5.413307-02	-4.9601780-07
18	5.0526224-02	5.0526223-02	-8.4482107-07
19	4.6741978-02	4.6741978-02	-4.5660902-07
20	4.3347076-02	4.3347075-02	-1.2533060-06
21	4.0289110-02	4.0289111-02	9.6316614-07
22	3.7524466-02	3.7524465-02	-5.6877050-07
23	3.5016547-02	3.5016542-02	1.2744226-06
24	3.2734417-02	3.2734417-02	6.5199904-07
25	3.0651788-02	3.0651787-02	-9.0114859-07
26	2.8746149-02	2.8746149-02	7.0870993-07
27	2.6998141-02	2.6998141-02	5.7493006-07
28	2.5391020-02	2.5391020-02	9.1698026-07
29	2.3910242-02	2.3910242-02	6.4917968-07
30	2.2543110-02	2.2543111-02	2.4959912-06
31	2.1278507-02	2.1278507-02	-2.6671265-06
32	2.0106646-02	2.0106646-02	6.5136291-07
33	1.9018894-02	1.9018894-02	8.9265098-07
34	1.8007603-02	1.8007603-02	1.2121476-06
35	1.7065977-02	1.7065978-02	2.7001714-06
36	1.6187963-02	1.6187963-02	9.2889879-07
37	1.5368147-02	1.5368147-02	-8.5219929-07
38	1.4601681-02	1.4601681-02	1.0962509-06
39	1.3884210-02	1.3884210-02	3.4062957-06
40	1.3211811-02	1.3211812-02	4.9564451-07

1	1.9429179-01	1.7386119+04
2	4.3356751-02	3.5801759+03
3	5.5865030-02	2.6374800+03
4	6.3869325-02	1.6961658+03
5	3.6648696-02	1.2601571+03
6	6.4763136-02	9.6959281+02
7	4.4868906-03	7.5916924+02
8	4.7378590-02	6.8416264+02
9	4.3472489-02	5.7933518+02
10	8.7835575-02	4.2203653+02
11	5.4996306-02	3.0363052+02
12	8.6400848-02	2.2604541+02
13	8.3277536-02	1.4304483+02
14	4.0438820-02	1.0203543+02
15	4.5278354-02	7.0901771+01
16	3.2748827-02	4.7945420+01
17	1.4776124-02	2.4307031+01
18	3.4911824-05	6.0000000

SSS-R-75-2556

TRANSMISSION FCN			FOR U Z ONE		EXPONENTIAL APPROX		PERCENT ERROR	
1	1.0000000	0.00	1.0000000	0.05	0.00	4.7683704	0.05	
2	9.8800537	-0.01	9.8799245	-0.01	-1.3076236	-0.03		
3	9.7663565	-0.01	9.7673692	-0.01	1.0573753	-0.02	1	
4	9.6639603	-0.01	9.6615968	-0.01	-2.4460332	-0.02	2	
5	9.5606127	-0.01	9.5620831	-0.01	1.5379072	-0.02	3	
6	9.4671703	-0.01	9.4684377	-0.01	1.3386613	-0.02		
7	9.3822055	-0.01	9.3802792	-0.01	-2.0533241	-0.02		
8	9.2966113	-0.01	9.2972508	-0.01	-6.8784347	-0.03		

**Table 2.1(b) - contd.**

FOR CO2 + OTHER UNIFORMLY-MIXED GASES			
TRANSMISSION FCN	EXPONENTIAL APPROX	PERCENT ERROR	
1	1.000000+00	1.4901161-06	
2	6.8215742-01	6.3225475-02	
3	5.681523-01	-2.5855713-01	
4	4.9134884-01	4.9257342-01	
5	4.3787103-01	4.3827150-01	
6	3.95332858-01	3.9554662-01	
7	3.6176677-01	3.6021745-01	
8	3.2995347-01	3.3014239-01	
9	3.0256958-01	3.0409489-01	
10	2.8114019-01	2.8128455-01	
11	2.6189547-01	2.6114865-01	
12	2.4374840-01	2.4325765-01	
13	2.2743368-01	2.2726938-01	
14	2.1322656-01	2.1290463-01	
15	2.0072765-01	1.9993247-01	
16	1.8781365-01	1.8816048-01	
17	1.7655137-01	1.7742755-01	
18	1.6748806-01	1.6759835-01	
19	1.5887104-01	1.5855891-01	
20	1.5023282-01	1.5021296-01	
21	1.4204844-01	1.4247903-01	
22	1.3494578-01	1.3528794-01	
23	1.2840746-01	1.2858078-01	
24	1.2215984-01	1.2230724-01	
25	1.1640502-01	1.1642418-01	
26	1.1100813-01	1.1089449-01	
27	1.0582295-01	1.0580612-01	
28	1.0083348-01	1.0077124-01	
29	9.6280253-02	9.6125620-02	
30	9.1938386-02	9.1728019-02	
31	8.7743722-02	8.7559761-02	
32	8.3686624-02	8.3604330-02	
33	7.9779672-02	7.9847042-02	
34	7.6308515-02	7.6274763-02	
35	7.2940993-02	7.2875777-02	
36	6.9671091-02	6.9639398-02	
37	6.6473312-02	6.6556009-02	
38	6.3402603-02	6.3616836-02	

Table 2.1(c) 800 - 840  $\text{cm}^{-1}$ 

..... F O R    W A T E R    V A P O R    .....			
TRANSMISSION FCN	EXPONENTIAL APPROX	PERCENT ERROR	
1	1.0000000+00	3.1768771-03	
2	9.4042661-01	-2.2649581-02	
3	9.1020309-01	4.4010146-02	
4	8.9014296-01	-2.1318391-02	
5	8.7211727-01	5.1415782-02	
6	8.5693191-01	-7.1675546-03	
7	8.4260471-01	-2.5054757-02	
8	8.3036546-01	-1.6986231-01	
9	8.1648200-01	-2.5706084-03	
10	8.0373137-01	1.3734478-01	
11	7.9335209-01	8.4028721-02	
12	7.8369474-01	3.3002358-02	
13	7.7540431-01	-1.0546813-01	
..... F O R    C O <sub>2</sub> + OTHER UNIFORMLY MIXED GASES    .....			
COEFFICIENTS                      EXPONENTS			
1	5.3252484-02	2.2769510+00	
2	2.9769137-01	1.2339420-01	
3	6.4906793-01	0.0000000	
TRANSMISSION FCN    EXPONENTIAL APPROX    PERCENT ERROR			
1	1.0000000+00	0.0000000	
2	9.8631965-01	9.8831677-01	2.0227731-01
3	9.7778041-01	9.7677004-01	-1.0338638-01
COEFFICIENTS                      EXPONENTS			
1	1.0000000+00	2.3504029-03	

Table 2.1(d) 5440 - 5760  $\text{cm}^{-1}$ 

..... F O R W A T E R V A P O R .....			
TRANSMISSION FCN	EXPONENTIAL APPROX	PERCENT ERROR	
1	1.000000+00	9.9999999-01	-1.4901161-06
2	6.4619749-01	6.4619727-01	-3.4139265-05
3	5.7467587-01	5.7468100-01	8.9208507-04
4	5.3333506-01	5.3332159-01	-2.5254206-03
5	5.0429673-01	5.0427164-01	-4.9749347-03
6	4.8166101-01	4.8175348-01	1.9195429-02
7	4.6322583-01	4.6323960-01	2.9719218-03
8	4.4762514-01	4.4747227-01	-3.4157013-02
9	4.3371792-01	4.3373513-01	3.9682058-03
10	4.2147405-01	4.2156825-01	2.2347500-02
11	4.1064691-01	4.1065013-01	7.8425680-04
12	4.0086194-01	4.0074403-01	-2.9419935-02
13	3.9157828-01	3.9167049-01	2.3545210-02
14	3.8329461-01	3.8329118-01	-8.9477524-04
15	3.7554555-01	3.7549635-01	-1.2570249-02
16	3.6821349-01	3.6820746-01	-1.6393025-03
17	3.6124826-01	3.6135169-01	2.0627046-02
18	3.5479525-01	3.5487787-01	2.3283033-02
19	3.4868080-01	3.4874335-01	1.7936953-02
20	3.4295805-01	3.4291364-01	-1.2949336-02
21	3.3751711-01	3.3736057-01	-4.6391339-02
22	3.3224897-01	3.3206089-01	-5.6624820-02
23	3.2703180-01	3.2699518-01	-1.1101576-02
24	3.2213384-01	3.2214702-01	4.0937082-03
25	3.1736696-01	3.1750239-01	4.2662836-02
26	3.1292451-01	3.1304910-01	3.9799049-02
27	3.0871639-01	3.0877648-01	1.9461056-02
28	3.0468638-01	3.0467504-01	-3.7223697-03
29	3.0080248-01	3.0073626-01	-2.2017245-02
30	2.96988453-01	2.9695243-01	-1.0810775-02
..... C O E F F I C I E N T S E X P O N E N T S .....			
1	2.2790496-01	1.6704346+01	
2	1.3616368-01	4.1405703+00	
3	1.4114620-01	1.0936147+00	
4	2.9307161-01	1.6067582-01	
5	2.0171355-01	0.0000000	



Table 2.1(e) 32000 - 33000  $\text{cm}^{-1}$ 

..... F O R U Z O N E .....		.....	
TRANSMISSION FCU	EXPONENTIAL APPROX	PERCENT ERROR	
1 1.0000000000	9.9999762-01	-2.3767380-04	
2 9.2162972-01	9.2152821-01	-1.6299250-04	
3 8.5004603-01	8.5004519-01	-9.9026051-05	
4 7.8461202-01	7.8461164-01	-4.4763583-05	
5 7.2475424-01	7.2475424-01	1.8504266-07	
6 6.6995614-01	6.6995639-01	3.7455512-05	
7 6.1975216-01	6.1975258-01	6.6769449-05	
8 5.7372245-01	5.7372295-01	8.7528196-05	
9 5.3148814-01	5.3148869-01	1.0367950-04	
10 4.9270719-01	4.9270774-01	1.1383625-04	
11 4.5707057-01	4.5707111-01	1.2010365-04	
12 4.2429896-01	4.2429948-01	1.2247913-04	
13 3.9413971-01	3.9414018-01	1.1940225-04	
14 3.6636416-01	3.6636458-01	1.1525729-04	
15 3.4076520-01	3.4076557-01	1.0635864-04	
16 3.1715519-01	3.1715550-01	9.7326929-05	
17 2.9536393-01	2.9536418-01	8.4440939-05	
18 2.7523704-01	2.7523724-01	7.3257313-05	
19 2.5663431-01	2.5663446-01	5.9210534-05	
20 2.3942836-01	2.3942846-01	4.3993351-05	
21 2.2350338-01	2.2350344-01	2.9435178-05	
22 2.0875400-01	2.0875403-01	1.2714818-05	
23 1.9508431-01	1.9508430-01	-2.4538099-06	
24 1.8240691-01	1.8240688-01	-1.8487016-05	
25 1.7064215-01	1.7064209-01	-3.3084899-05	
26 1.5971734-01	1.5971727-01	-4.7908060-05	
27 1.4956614-01	1.4956605-01	-6.1595796-05	
28 1.4012795-01	1.4012784-01	-7.5055904-05	
29 1.3134735-01	1.3134723-01	-8.8043174-05	
30 1.2317366-01	1.2317353-01	-1.0023693-04	
31 1.1556048-01	1.1556035-01	-1.1051961-04	
32 1.0846531-01	1.0846518-01	-1.2162551-04	
33 1.0184919-01	1.0184905-01	-1.3710995-04	
34 9.5676377-02	9.5676243-02	-1.3969160-04	
35 8.9714050-02	8.9713927-02	-1.4813130-04	
36 8.4532106-02	8.4531973-02	-1.5679952-04	
37 7.9502907-02	7.9502670-02	-1.6246333-04	
38 7.4800681-02	7.4800550-02	-1.6447107-04	

	COEFFICIENTS	EXPONENTS
1	1.5133501-01	6.3029917+00
2	2.7841505-01	5.0168507+00
3	1.9825387-01	3.5065411+00
4	1.6963843-01	3.1942169+00
5	1.2282156-01	2.3337323+00
6	7.9533725-02	2.1455175+00

Table 2.2

Coefficients and exponents for the exponential fits of transmission functions in the five spectral intervals, 180 - 240  $\text{cm}^{-1}$ , 720 - 740  $\text{cm}^{-1}$ , 800 - 840  $\text{cm}^{-1}$ , 5440 - 5760  $\text{cm}^{-1}$ , and 32000 - 33000  $\text{cm}^{-1}$  ( $n_{\text{max}} = 80$ ,  $\text{Tr}_{\text{min}} = 0.04$ )

## For Water Vapor

	COEFFICIENTS	EXPONENTS
1	7.7563684-02	6.6173130+04
2	4.6181609-02	1.3289408+04
3	4.5090727-02	7.4714703+03
4	5.3694783-03	6.2633637+03
5	5.1365345-02	4.3711194+03
6	1.4955810-02	3.3192736+03
7	6.1768176-02	2.4900121+03
8	2.9725030-02	1.6884777+03
9	5.7676750-02	1.4368250+03
10	4.0343264-02	9.5935166+02
11	4.0598607-02	6.8681096+02
12	2.4581004-02	7.9102383+02
13	1.0924025-01	5.2561479+02
14	2.2293679-02	3.9611453+02
15	1.1513306-01	2.8605335+02
16	8.9622140-02	1.7608871+02
17	2.8611519-02	1.1415686+02
18	8.4192258-02	9.4613272+01
19	2.2242038-02	5.0628239+01
20	3.3437070-02	5.3190099+01

(a) 180 - 240  $\text{cm}^{-1}$ 

## For Water Vapor

	COEFFICIENTS	EXPONENTS
1	1.0380458-02	8.4208226+01
2	6.9627069-02	3.1774609+00
3	2.6972948-01	2.1767528-01
4	6.5126277-01	1.64333697-02

For CO<sub>2</sub>

	COEFFICIENTS	EXPONENTS
1	1.0757056-01	2.5416238+01
2	2.30226096-01	3.3653365+00
3	3.3546586-01	6.9361494-01
4	3.2670589-01	1.5410237-01

## For Ozone

	COEFFICIENTS	EXPONENTS
1	5.5150159-04	1.3039266+01
2	2.0720544-01	1.6445462+00
3	7.9233105-01	0.0000000

(b) 720 - 740  $\text{cm}^{-1}$

Table 2.2, contd.

## For Water Vapor

	COEFFICIENTS	EXPONENTS
1	7.6118593-C3	5.5262042+01
2	4.5755173-02	2.0952084+00
3	2.99337959-01	1.2204550-01
4	6.4705335-01	6.0000000

For CO<sub>2</sub>

	COEFFICIENTS	EXPONENTS
1	1.0000000+00	2.3504029-03

2-50

## For Water Vapor

	COEFFICIENTS	EXPONENTS
1	1.9154203-C1	2.6494272+01
2	5.3843621-02	7.5389322+00
3	1.1890704-C1	4.0007756+00
4	1.4072478-C1	1.0944522+03
5	2.9305787-C1	1.6097549-01
6	2.0191963-C1	6.0000000

(d) 5440 - 5760 cm<sup>-1</sup>

## For Ozone

	COEFFICIENTS	EXPONENTS
1	8.7551614-02	6.4310453+00
2	1.0109020-C1	5.8711309+00
3	2.1753932-01	5.0109434+00
4	1.8476970-01	3.7668060+00
5	1.9318001-01	3.1520671+00
6	8.5236210-02	2.5867038+00
7	1.3556731-C1	2.1608418+00

(e) 32000 - 33000 cm<sup>-1</sup>

Table 2.3

Coefficients and exponents for the exponential fits of transmission functions in the three spectral intervals, 180 - 240  $\text{cm}^{-1}$ , 720 - 740  $\text{cm}^{-1}$ , (CO<sub>2</sub> + only), and 3200 - 3300  $\text{cm}^{-1}$  ( $u_{\text{max}} = 80$ ,  $Tr_{\text{min}} = 0.15$ )

## For Water Vapor

	COEFFICIENTS	EXPONENTS
1	2.8437159-02	2.1821593+05
2	7.5091862-03	8.885131+04
3	2.8541729-02	3.3458946+04
4	7.8738582-02	2.0827184+04
5	1.0280145-02	1.8085987+04
6	7.1281167-02	1.3841822+04
7	2.2959148-02	1.1723123+04
8	2.4307048-02	8.2888714+03
9	1.3739203-02	7.1271766+03
10	2.9963700-02	5.4729254+03
11	3.8770854-02	3.9736457+03
12	2.7157997-02	3.035076+03
13	5.3681642-02	2.2464229+03
14	4.1890734-02	1.5705673+03
15	8.5116676-02	1.1108971+03
16	7.2094296-02	7.2261260+02
17	1.8719054-01	4.1192960+02
18	2.3082714-01	7.4231581+02
19	4.7870888-02	4.8531877+01
20	1.3632708-02	0.0000000

(a) 180 - 240  $\text{cm}^{-1}$ 

For CO<sub>2</sub>

	COEFFICIENTS	EXPONENTS
1	4.8741058-02	2.4454967+02
2	5.6251078-02	2.2082878+01
3	1.9694652-01	3.6680425+00
4	1.7703375-01	1.2121288+00
5	4.5915857-01	3.7030522-01
6	6.1269065-02	0.0000000

(b) 720 - 740  $\text{cm}^{-1}$ 

## For Ozone

	COEFFICIENTS	EXPONENTS
1	3.1182365-03	7.8242436+00
2	8.8540089-02	6.2307800+00
3	2.0446707-01	5.8866288+00
4	1.3586891-01	4.4008119+00
5	3.1842368-01	3.5220810+00
6	1.5753501-01	2.4054787+00
7	8.0546888-02	2.1844162+00

(c) 3200 - 3300  $\text{cm}^{-1}$

of the different origins of the data, there are rather striking differences between both the accuracy of the fits and the number of terms in them: the fit in Table 2.1(a) is exact to the accuracy carried by our computer and consists of 18 terms; the fits in Table 2.1(b) - (e) are considerably more approximate and consist at most of 6 terms. As a general principle, the larger the number of continuous derivatives possessed by the transmission function  $T_{\Delta\nu}(u)$  generating the data, the closer will be the exponential fit. This is obvious from an intuitive standpoint because a sum of exponentials is infinitely differentiable, and so can only match exactly with another infinitely differentiable function belonging to the function space of exponential sums. The  $T_{\Delta\nu}(u)$  used in the band model is in fact infinitely differentiable on  $0 \leq u < \infty$ , while the McClatchey data, involving as it does linear interpolation in a table of transmissions, has discontinuous first derivatives. (This suggests one way in which the appropriateness of the McClatchey scheme for exponential fitting might be improved, which is to use instead of linear interpolation, interpolation schemes of higher differentiability such as cubic splines.)

A common feature of every one of the fits in Table 2.1 is the seemingly random variation of the sign of error. This indicates that the exponential fit wanders above and below the transmission data, as it should if it is a least squares fit. Inaccuracies in the fitting process, caused for example by using too many data points (like  $n_{\max} = 150$ ), can often be detected by observing this sign pattern. When all the errors are of one sign, for example, computational problems are definitely indicated.

The following approximation may be viewed

$$\frac{1}{\Delta v} \int_{\Delta v} e^{-k_v u} dv \approx \sum a_i e^{-k_i u}$$

as a Lebesgue quadrature rule with coefficient  $a_i$  representing the fraction of the spectral interval  $\Delta v$  over which the absorption coefficient is roughly  $k_i$ . Thus, the exponential fits provide some insight into the underlying distribution of line intensity in  $\Delta v$ . In the 180 - 240  $\text{cm}^{-1}$  interval of Table 2.1(a), for example, one could deduce a sizable proportion ( $\sim 0.2$ ) of strong absorption near  $k_1 = 17386.1 \text{ cm}^2/\text{g}$  and a fairly uniform distribution of absorption ranging all the way from 3580  $\text{cm}^2/\text{g}$  to 24  $\text{cm}^2/\text{g}$ . For water vapor in the 720 - 740  $\text{cm}^{-1}$  interval (Table 2.1(b)), we observe a preponderant fraction (0.64) of very weak absorption ( $k \sim 0.015 \text{ cm}^2/\text{g}$ ), half as much ( $\sim 0.28$ ) of 14 times stronger absorption ( $k \sim 0.208 \text{ cm}^2/\text{g}$ ), and a small fraction (0.08) of yet 16 times stronger absorption ( $k \sim 3.28 \text{ cm}^2/\text{g}$ ). For ozone in the 32000 - 33000  $\text{cm}^{-1}$  interval (Table 2.1(e)), the range of  $k$ 's is quite small, only 0.63  $(\text{atm-cm})^{-1}$  to 0.21  $(\text{atm-cm})^{-1}$ , indicating very little line structure. Of course, the  $a$ 's and the  $k$ 's vary as we change the number of data points  $n_t$ , the lower limit  $\text{Tr}_{\min}$ , and the spacing  $\Delta u$ , so the  $a$ 's and the  $k$ 's cannot be taken too literally. Nevertheless, qualitative features such as the range of the  $k_i$ 's remain invariant as the details of the fitting process are varied. The only exception to this rule is when the fitting is changed so as to resolve parts of the  $T_{\Delta v}(u)$  curve not previously resolved; in this case, much larger and much smaller  $k$ -values may arise than were found using the inadequate resolution.

To show the effects of changing the fitting parameters, Table 2.2 contains the coefficients and exponents generated for all five spectral intervals when  $n_{\max}$  is increased to 80 (from 40) and  $Tr_{\min}$  is increased to 0.04 (from 0.01). Table 2.3 contains similar information for  $180 - 240 \text{ cm}^{-1}$ ,  $\text{CO}_2$  in  $720 - 740 \text{ cm}^{-1}$ , and ozone in  $32000 - 33000 \text{ cm}^{-1}$  when  $n_{\max}$  is left at 80 and  $Tr_{\min}$  is further increased to 0.15 (the other fits are unchanged from Table 2.2).

The transmission data for the  $180 - 240 \text{ cm}^{-1}$  interval of Table 2.2(a) contain better but still inadequate resolution in the range  $0.1 - 1.0$  as compared to Table 2.1 (a). The largest exponent in Table 2.2(a) is a factor of four larger than in Table 2.1(a), in order to account for the initial steep decrease of the transmission which had been even more poorly resolved before. There are many more large exponents in Table 2.2(a) than in Table 2.1(a). A continuation of this trend is observable in Table 2.3(a), in which the largest exponent has increased a further factor of three on account of even better resolution in  $0.1 - 1.0$ . Note that the smallest exponent also increases from Table 2.1(a) to Table 2.2(a) to Table 2.3(a), which is due to the progressive increase in  $Tr_{\min}$  and the consequent loss of resolution in the tail of the transmission, where the small exponents predominate. Granted these quite understandable changes in the exponent range, however, the most important thing to notice about Tables 2.1(a), 2.2(a), and 2.3(a) is their qualitative similarities; the number of exponents and their distribution between the extremes, and the size and general pattern of the coefficients exhibit regularities which are preserved as the range and resolution of the data change.

Comparing the water vapor parts of Tables 2.1(b) and 2.2(b) for  $720 - 740 \text{ cm}^{-1}$ , it is apparent that the only change due to the better resolution in Table 2.2(b) is to add a large exponent (84.2) with a small coefficient. The other coefficients and exponents are virtually unchanged. The fit is independent of  $\text{Tr}_{\text{min}}$  since the transmission range is so small.

The  $\text{CO}_2$  fit for  $720 - 740 \text{ cm}^{-1}$  (a region of large  $\text{CO}_2$  absorption) in Table 2.2(b) is very similar to that of Table 2.1(b) except that the largest exponent has decreased by a factor of three due primarily to fitting a single extra transmission datum between 0.682 and 1.0 (at 0.776). The comparison  $\text{CO}_2$  fit of Table 2.3(b), which fits transmission data having even more resolution between 0.7 and 1.0 (namely points 0.71, 0.76, and 0.83) but no points in the tail beyond 0.15, adds a large exponent ten times bigger than the largest exponent of Table 2.2(b), retains similar exponents in the mid-range, then deviates again for small exponents. The addition of the zero exponent with a non-negligible coefficient seems strange, but it is due to the fact that cutting off the data at 0.15 allows the method to insert a constant term (zero-exponent term) into the fit with any coefficient up to 0.15 if it so desires, in an attempt to fit the data. Without any transmission resolution below 0.15, and without some physical basis for putting a lower bound on the exponents (hard to come by because of lack of knowledge of line wings), there is no sound reason for rejecting this zero exponent.



The ozone 32000 - 33000  $\text{cm}^{-1}$  fit of Table 2.3(c) illustrates the danger of making generalizations about the exponential fitting process. Here we have severely reduced the resolution in the transmission tail by taking  $\text{Tr}_{\min} = 0.15$ , and yet we observe practically no impact on the minimum exponent compared to Table 2.2(e). This is quite different from the situations in Table 2.3(a) and (b), where knowledge of the small exponents was reduced in the same circumstances. Ozone in this region is of course anomalous in its relatively small range of absorption coefficient, but it nevertheless serves to illustrate the point that it is not always necessary to consider very small values of the transmission.

There is very little substantive difference between the remainder of the fits in Table 2.2 and their analogues in Table 2.1.

In conclusion, we mention that when the range of transmission values which need to be considered is small enough ( $T_{\Delta v}(u_{\max}^*) \geq 0.93$  in the current code), the full exponential fitting routine is bypassed in favor of a one-term least-squares exponential fit to three data points, which can be done analytically. Assuming that the one-term exponential approximation is

$$e^{-ku}$$

in order to give unit transmission for  $u = 0$ , and defining

$$\theta = e^{-ku_{\max}^*/2},$$

the least-squares residual becomes

$$R = [T_{\Delta v}(\frac{u_{\max}^*}{2}) - \theta]^2 + [T_{\Delta v}(u_{\max}^*) - \theta^2]^2 .$$

The condition  $\frac{dR}{d\theta} = 0$  then yields a cubic equation for  $\theta$ ,

$$2\theta^3 + [1 - 2T_{\Delta v}(u_{\max}^*)]\theta - T_{\Delta v}(\frac{u_{\max}^*}{2}) = 0 ,$$

which can be shown to have only one positive real root for  $T_{\Delta v}$ 's of interest. An example of such a one-term fit, for  $\text{CO}_2$  can be seen in Table 2.1(c).

#### 2.5.1.4 Tables of Fitting Parameters

It is desirable to make ATRAD as computationally efficient as possible, with a view to executing it a large number of times for: (a) heat budget studies involving a large fraction of the globe, (b) diurnal cycle studies, and (c) parameter studies involving the albedo, aerosol density, cloud cover, sun angle, etc. In none of these multiple executions would there be any need to change the ATRAD spectral interval structure - and since the transmission function fitting depends on the spectral intervals, the fitting parameters can be computed once and for all and kept in tables. This is especially important in view of the fact that, in the original version of ATRAD, the pacing items as regards computer time were the Mie calculation and the fitting calculation.

Therefore, the fitting is now done by a separate code module, called EVANS-TABLES. The table currently used for ATRAD consists of fitting parameters for 120 spectral intervals spanning the spectral range of  $60 - 48500 \text{ cm}^{-1}$ . ATRAD has the capability of using the full fitting tables, or any sub-set thereof. Using

these tables, it is possible to perform a complete ATRAD calculation (without Mie scattering) for 40 levels, and for from 6 to 12 Gaussian angles, at a cost of anywhere between 300 and 400 CPU seconds on the UNIVAC 1108. If edits of each spectral interval are suppressed, this reduces to 200 - 250 CPU seconds. Clearly, the use of fitting tables effects tremendous computational savings over the earlier version of ATRAD, which required 40 - 60 minutes for a complete clear-sky calculation.

### 2.5.2 Treatment of Overlapping Bands

In many frequency groups  $\Delta\nu$ , more than one atmospheric constituent may contribute to the absorption. ATRAD then fits the transmission function  $T_{\Delta\nu}^{(n)}$  of each individual constituent with an exponential sum,

$$T_{\Delta\nu}^{(n)}(u) \approx \sum_{i=1}^{M^{(n)}} a_i^{(n)} e^{-k_i^{(n)} u^{(n)}}$$

Superscript 1 refers to  $H_2O$ , superscript 2 to the uniformly mixed gases  $CO_2$ , etc., and superscript 3 to  $O_3$ . The product of these individual transmission functions is taken as the total transmission,

$$T_{\Delta\nu} \approx \sum_{i=1}^{M^{(1)}} \sum_{j=1}^{M^{(2)}} \sum_{\ell=1}^{M^{(3)}} a_i^{(1)} a_j^{(2)} a_{\ell}^{(3)} e^{-(k_i^{(1)} u^{(1)} + k_j^{(2)} u^{(2)} + k_{\ell}^{(3)} u^{(3)})}$$

Then  $M = M^{(1)} M^{(2)} M^{(3)}$  monochromatic problems are calculated, one for each term of the triple sum, in each of which the optical depth of zone  $[z, z']$  is

$$\begin{aligned} \Delta\tau(z, z') = & k_i^{(1)} u^{(1)}(z, z') + k_j^{(2)} u^{(2)}(z, z') \\ & + k_\ell^{(3)} u^{(3)}(z, z') \end{aligned}$$

and the line absorption coefficient at  $z$  is

$$\begin{aligned} \alpha^{\text{line}}(z) = & - \frac{\partial}{\partial z} \Delta\tau(z, z') \\ = & - k_i^{(1)} \frac{\partial}{\partial z} u^{(1)}(z, z') - k_j^{(2)} \frac{\partial}{\partial z} u^{(2)}(z, z') \\ & - k_\ell^{(3)} \frac{\partial}{\partial z} u^{(3)}(z, z') \end{aligned}$$

The  $z$ -derivatives of the  $u$ 's are simply the integrands in the expressions (2.22) defining the  $u$ 's.

## 2.6 SEPARATION OF INTENSITY INTO SOLAR AND DIFFUSE PARTS

Because the solar beam and the specular reflection (if any) of the solar beam are essentially  $\delta$ -functions in angle, it is customary before solving the radiative transfer equation numerically to eliminate these beams from explicit consideration via the following transformation:

$$i_v = \begin{cases} \bar{I}_v - \bar{I}_v^{\text{spec}} & -1 \leq \mu < 0 \\ \bar{I}_v - \bar{I}_v^{\text{solar}} & 0 < \mu \leq 1 \end{cases} \quad (2.29)$$

$i_v$ , the diffuse intensity, may be expected to behave 'smoothly' as a function of angle, that is, to be amenable to angular

quadrature schemes which assume  $i_v$  can be approximated by a low-order polynomial in  $\mu$ . The solar intensity  $\bar{i}_v^{\text{solar}}$  and the specularly reflected solar intensity  $\bar{i}_v^{\text{spec}}$  are obtained by considering the incident solar beam to be acted upon only by extinction  $\kappa_v$  and specular reflection  $\rho'_{v,s}$ :

$$\bar{i}_v^{\text{solar}} = \frac{S_v}{2\pi} e^{-\tau_v(z)/\mu} \delta(\mu - \mu_0)$$

$$\bar{i}_v^{\text{spec}} = \frac{S_v}{2\pi} \rho'_{v,s}(|\mu|) e^{[2\tau_v(z_0) - \tau_v(z)]/\mu} \delta(\mu + \mu_0)$$

where

$$\tau_v(z) = \int_0^z \kappa_v(z') dz' .$$

is the optical depth measured from the top of the atmosphere.

If the transformation (2.29) is applied to the radiative transfer equation (2.6), the boundary conditions (2.10) and (2.14), and the flux equation (2.7), the results are:

$$\mu \frac{\partial i_v}{\partial z} + \kappa_v i_v = \alpha'_v B_v + \frac{\beta_v}{2} \int_{-1}^1 \bar{P}_v(z, \mu, \mu') i_v(z, \mu') d\mu' + Q_v(z, \mu) \quad (2.30)$$

$$Q_v(z, \mu) = \frac{\beta_v S_v}{4\pi} \bar{P}_v(z, \mu, \mu_0) e^{-\tau_v(z)/\mu_0} + \frac{\beta_v S_v}{4\pi} \rho'_{v,s}(\mu_0) \bar{P}_v(z, \mu, -\mu_0) e^{-[2\tau_v(z_0) - \tau_v(z)]/\mu_0}$$

$$i_v(0, \mu) = 0, \quad 0 < \mu \leq 1 \quad (2.31)$$

$$\begin{aligned}
i_v(z_0, \mu) = & \varepsilon'_v(|\mu|) B_v(T_g) + \rho'_{v,s}(|\mu|) i_v(z_0, |\mu|) \\
& + 2 \int_0^1 d\mu' \bar{\rho}''_{v,d}(|\mu|, \mu') i_v(z_0, \mu') \mu' \\
& + \frac{S_v}{\pi} \mu_0 \bar{\rho}''_{v,d}(|\mu|, \mu_0) e^{-\tau_v(z_0)/\mu_0}, \quad -1 \leq \mu < 0
\end{aligned}
\tag{2.32}$$

$$\begin{aligned}
F_v(z) = & 2\pi \int_{-1}^1 \mu i_v(z, \mu) d\mu + \mu_0 S_v e^{-\tau_v(z)/\mu_0} \\
& - \mu_0 S_v \rho'_{v,s}(\mu_0) e^{-[2\tau_v(z_0) - \tau_v(z)]/\mu_0}
\end{aligned}
\tag{2.33}$$

These are the equations which are solved numerically in ATRAD by methods described in Section 2.8.

There are two functions in Eqs. (2.30) and (2.32) which, if they were not smooth functions of angle, could destroy the assumed smoothness of  $i_v$  as a function of  $\mu$ ; they are the phase function  $\bar{F}_v$  and the diffuse bidirectional reflectivity  $\bar{\rho}''_{v,d}$ . The strongest peak in  $P_v$  is due to forward scattering by aerosol particles; therefore, ATRAD incorporates an approximation wherein this sharp peak is replaced by a  $\delta$ -function, leaving a truncated phase function which is much smoother (see Section 2.7.5). The same procedure can be applied to a broadened reflection peak in  $\bar{\rho}''_{v,d}$ , such as might be caused by a slightly disturbed ocean surface. That is, the peak will be approximated by a  $\delta$ -function and lumped into the specular reflectivity  $\rho'_{v,s}$ , leaving a truncated and much smoother diffuse bidirectional reflectivity  $\rho''_{v,d}^{(\text{trunc})}$  for use in the boundary condition (2.32).

## 2.7 SCATTERING TREATMENT

2.7.1 Rayleigh Scattering

The Rayleigh volume scattering coefficient,

$$\beta_{v,R} = \frac{8\pi^3}{3} \frac{(n_s^2 - 1)^2}{\lambda^4 N_s^2} \left( \frac{6 + 3\rho_n}{6 - 7\rho_n} \right) \frac{p}{kT}$$

and the Rayleigh phase function for unpolarized light

$$P_R(\mu_s) = \frac{3(1 + \rho_n)}{4 + 2\rho_n} \left( 1 + \frac{1 - \rho_n}{1 + \rho_n} \mu_s^2 \right)$$

are taken from the review article of Penndorf.<sup>[31]</sup> The various quantities in these equations are:

$n_s$  = index of refraction of air at 760 mm Hg  
and 15°C

$\lambda$  = wavelength

$N_s$  = number density of air molecules at 760 mm Hg  
and 15°C =  $2.54743 \times 10^{19} \text{ cm}^{-3}$

$\rho_n$  = depolarization factor

$k$  = Boltzmann's constant

$\mu_s$  = cosine of scattering angle

$n_s$  is calculated according to the new empirical formula of Peck and Reeder,<sup>[32]</sup> which supersedes the older Edlen formula.<sup>[31]</sup>

$\rho_n$ , which is a measure of the anisotropy of the air molecules, is taken as 0.0303 following Gucker, et.al.<sup>[33]</sup>

### 2.7.2 Mie Scattering, Single Sphere

Mie scattering of a plane wave of wavelength  $\lambda$  from an aerosol particle of radius  $a$  is described rigorously by the following infinite series:<sup>[3]</sup>

$$\sigma_{\text{ext}} = \frac{\lambda^2}{2\pi} \sum_{n=1}^{\infty} (2n+1) \operatorname{Re}(a_n + b_n) \quad (2.34)$$

$$\sigma_{\text{sca}} = \frac{\lambda^2}{2\pi} \sum_{n=1}^{\infty} (2n+1) (|a_n|^2 + |b_n|^2) \quad (2.35)$$

$$\sigma_{\text{abs}} = \sigma_{\text{ext}} - \sigma_{\text{sca}}$$

$$i_1 = \left| \sum_{n=1}^{\infty} \frac{2n+1}{n(n+1)} \left[ a_n(\alpha, m) \pi_n(\mu_s) + b_n(\alpha, m) \tau_n(\mu_s) \right] \right|^2 \quad (2.36)$$

$$i_2 = \left| \sum_{n=1}^{\infty} \frac{2n+1}{n(n+1)} \left[ a_n(\alpha, m) \tau_n(\mu_s) + b_n(\alpha, m) \pi_n(\mu_s) \right] \right|^2 \quad (2.37)$$

where

$$\alpha = \frac{2\pi a}{\lambda}$$

$$\begin{aligned} m &= \text{complex index of refraction} \\ &= n_1 - in_2 \end{aligned}$$

$$\beta = m\alpha$$



$$a_n = \frac{\psi_n(\alpha)\psi'_n(\beta) - m\psi_n(\beta)\psi'_n(\alpha)}{\zeta_n(\alpha)\psi'_n(\beta) - m\psi_n(\beta)\zeta'_n(\alpha)}$$

$$b_n = \frac{\psi_n(\beta)\psi'_n(\alpha) - m\psi_n(\alpha)\psi'_n(\beta)}{\psi_n(\beta)\zeta'_n(\alpha) - m\zeta_n(\alpha)\psi'_n(\beta)}$$

$$\pi_n(\mu) = P'_n(\mu)$$

$$\tau_n(\mu) = \mu\pi_n(\mu) - (1-\mu^2)\pi'_n(\mu) \quad .$$

The  $P_n$  are Legendre polynomials and the  $\psi_n$ ,  $\zeta_n$  are Ricatti-Bessel functions.  $\sigma_{\text{ext}}$ ,  $\sigma_{\text{sca}}$ , and  $\sigma_{\text{abs}}$  are the extinction, scattering, and absorption cross sections of the particle.  $i_1$  and  $i_2$  describe the patterns of scattered intensity polarized perpendicular and parallel to the scattering plane (determined by incident and scattered beams), respectively. For the unpolarized light treatment assumed in ATRAD, the pattern of scattered intensity is proportional to  $i_1 + i_2$ .

It can be shown that  $\sigma_{\text{sca}}$  is related to the integral of  $i_1 + i_2$  over all scattering angles  $\Omega_s$ :

$$\sigma_{\text{sca}}(\alpha) = \left(\frac{\lambda}{2\pi}\right)^2 \int_{4\pi} [i_1(\alpha, \mu_s) + i_2(\alpha, \mu_s)] d\Omega_s \quad . \quad (2.38)$$

The numerical evaluation of the infinite series, Eqs. (2.34) through (2.37), while seemingly straightforward, has sources of error which are related to the accumulation of round-off error in recursively calculating  $\psi_n$ ,  $\zeta_n$ ,  $\pi_n$ , and  $\tau_n$ . Techniques to eliminate these errors have been discussed by numerous authors. Dave,<sup>[34]</sup> Kattawar and Plass,<sup>[35]</sup> and Denman, Heller, and Pangonis<sup>[36]</sup> are the primary sources of the present ATRAD formulation of the series

summation, in subroutine MIESCT. Calculated results were compared with the graphs of Kerker<sup>[3]</sup> and the tables of Deirmendjian<sup>[37]</sup> and of Denman, et.al.<sup>[36]</sup> Agreement was found in all cases with the published results.

The Mie scattering calculation requires the aerosol complex index of refraction  $m_v(z)$  as a function of frequency and height. This is the least well-known, for the real atmosphere, of all the required aerosol data. Excellent  $m_v$  data are available for water; we have selected the measurements of Irvine and Pollack,<sup>[38]</sup> Rusk, et.al.,<sup>[39]</sup> and Robertson and Williams<sup>[40]</sup> for inclusion in ATRAD (subroutine IOR). Even for water, however, the uncertainty in the real part of  $m_v$  is as high as 5 percent and in the imaginary part as high as 20-25 percent. Somewhat less accurate data are available for ice,<sup>[38]</sup> aqueous solutions of NaCl,<sup>[41]</sup> carbonaceous aerosol,<sup>[42,43]</sup> and quartz,<sup>[44]</sup> all of which have been included in ATRAD. The above substances have each been studied by several investigators, so at least the data have been measured independently. No such independent evaluation exists for the index of refraction measurements of Volz,<sup>[45,46]</sup> who studied sea salt, dust, Sahara dust, and several samples of water-soluble aerosol material; nevertheless, these data have also been included in ATRAD.

Aerosol materials, of course, have highly variable compositions and are subject to uncertainties regarding their chemical and physical states.

A large number of transmission spectra have been taken for atmospheric dust and for individual components of atmospheric dust.<sup>[47,48,49]</sup> These spectra indicate strong dust absorption in the atmospheric window region 8-13 $\mu$ , which could have a pronounced effect on radiative heating. However,

more data than the transmission spectrum of a substance are needed to deduce the index of refraction. Even less is known about the index of refraction of many other inorganic aerosol constituents. As for the organic aerosol fraction, which is considerable,<sup>[50]</sup> the lack of data is almost complete.

### 2.7.3 Mie Scattering, Polydispersion

In reality, the atmospheric aerosol consists of particles with a wide range of radii  $a$ . This variation is described by a size distribution function,

$$N_{\text{aer}}(z) n(a, z) \quad , \quad a_{\text{min}} \leq a \leq a_{\text{max}}$$

where  $N_{\text{aer}}(z)$  is the total number density of aerosol particles at height  $z$  and  $n(a, z)$  is the normalized distribution of radii at height  $z$ , defined such that

$$n(a, z) da = \text{fraction of particles at height } z \\ \text{with radii in } (a, a+da)$$

$$\int_{a_{\text{min}}}^{a_{\text{max}}} n(a, z) da = 1 \quad .$$

The separation of  $N_{\text{aer}}$  from  $n$  is convenient because in practical applications we often assume  $n$  is independent of  $z$ . The volume scattering and absorption coefficients for an aerosol described by such a size distribution are

$$\beta_{\text{v}, M}(z) = N_{\text{aer}}(z) \int_{a_{\text{min}}}^{a_{\text{max}}} \sigma_{\text{sca}}(\alpha) n(a, z) da \quad (2.39)$$

$$\alpha_{v,M}(z) = N_{aer}(z) \int_{a_{min}}^{a_{max}} \sigma_{abs}(\alpha) n(a,z) da \quad (2.40)$$

The pattern of scattered intensity will be proportional to

$$N_{aer}(z) \int_{a_{min}}^{a_{max}} [i_1(\alpha, \mu_s) + i_2(\alpha, \mu_s)] n(a,z) da \quad .$$

Normalizing this so that its integral over all scattering directions  $\Omega_s$  is  $4\pi$ , we obtain the Mie phase function

$$P_{v,M}(z, \mu_s) = 4\pi \frac{\int_{a_{min}}^{a_{max}} [i_1(\alpha, \mu_s) + i_2(\alpha, \mu_s)] n(a,z) da}{\int_{4\pi} d\Omega_s \int_{a_{min}}^{a_{max}} [i_1(\alpha, \mu_s) + i_2(\alpha, \mu_s)] n(a,z) da}$$

Inverting the order of integration in the denominator and employing the relationships of Eqs. (2.38) and (2.39),

$$P_{v,M}(z, \mu_s) = \frac{\lambda^2 N_{aer}(z)}{\pi \beta_{v,M}(z)} \int_{a_{min}}^{a_{max}} [i_1(\alpha, \mu_s) + i_2(\alpha, \mu_s)] n(a,z) da \quad (2.41)$$

Various analytic forms for  $n(a,z)$  have been proposed. Perhaps the most popular is the Junge power-law distribution<sup>[51]</sup>  $(ca^{-Y})$ ; in the American literature Deirmendjian's modified gamma distribution<sup>[52]</sup>  $(ca^Y e^{-ba\delta})$  for haze and cloud is also used extensively. Log-normal distributions

$$\left( \frac{1}{\sigma \sqrt{2\pi} a} e^{-\ln^2(r/r_0)/2\sigma^2} \right)$$

are used by some European and Russian aerosol researchers. [53,54] Twomey, et.al., [55] employ Gaussian distributions, but these are not in general use because most available data indicate an asymmetrical distribution of aerosol sizes. With the exception of the Junge distribution, which is unrealistically monotonic for all  $a$ , the data do not favor one size distribution formula over another. All of the above are included as options in ATRAD.

The dependence of  $N_{aer}(z)$  on  $z$  for the cloudless atmosphere has been investigated extensively; [56,57,58,59,60] certain regularities have been determined. Eltermann, [61] for example, has proposed a clear standard atmosphere with a prescription for  $N_{aer}(z)$  which has been included in ATRAD as an option. In clouds,  $N_{aer}$  may vary widely, [53] but most models ignore this and assume homogeneous clouds. The variation of  $N_{aer}$  (as well as  $n$ ) near a cloud's upper and lower boundaries may have important consequences for atmospheric heating, however, and should not be ignored. Such variations can be incorporated quite straightforwardly, within the framework of the ATRAD formalism.

A further complication for realistic aerosols is that the size distribution and the index of refraction depend on the relative humidity. [62,63] Hygroscopic aerosols may begin to take up water at a relative humidity as small as 50 percent. Hence it is impossible to specify realistic atmospheric structure data for ATRAD without taking this variable into consideration.

#### 2.7.4 Numerical Integration Over Aerosol Size Distribution

Techniques for performing the numerical integrations over size distribution in Eqs. (2.39) - (2.41) are far from standard. Most investigators use trapezoidal quadrature on the grounds that  $\sigma_{\text{sca}}$ ,  $\sigma_{\text{abs}}$ ,  $i_1$ , and  $i_2$  oscillate so rapidly and non-uniformly with  $\alpha$  that more sophisticated quadrature schemes are less accurate. This, of course, is a tacit admission that their integration meshes are not fine enough to resolve the oscillations. However, the present authors performed several integrations over size in which the oscillations were resolved, and the improvement in accuracy was too small (never more than a few percent) to warrant the additional computing cost - especially in light of uncertainties in the Mie input data for a real aerosol. Therefore, Romberg quadrature,<sup>[64]</sup> which is based on multiple trapezoidal quadratures, was selected for use in ATRAD.

The comprehensive study of Deirmendjian<sup>[52]</sup> proved useful in ascertaining suitable integration increments  $\Delta\alpha$  for the Romberg quadrature. However, Deirmendjian's  $\Delta\alpha$ 's were chosen by trial-and-error; he did not determine a universal prescription for selecting  $\Delta\alpha$ 's small enough to ensure accuracy yet large enough to avoid wasting computer time. Studies by Dave<sup>[65,66]</sup> indicate the danger of selecting  $\Delta\alpha$  too large and show that a  $\Delta\alpha$  which is satisfactory for integrating  $\beta_{v,m}$  and  $\alpha_{v,m}$ , and  $P_{v,M}$  for small angles, may be unsatisfactory for integrating  $P_{v,M}$  for larger angles. However, Dave, whose work was restricted to water droplets in the visible spectrum, provides no rule for automatic selection of  $\Delta\alpha$ .

Our Romberg scheme for integration of the fundamental Mie functions  $\sigma_{\text{sca}}$ ,  $\sigma_{\text{ext}}$ , and  $i_1 + i_2$  over aerosol size distribution  $n(a)$  was abandoned in favor of a trapezoidal scheme with a variable integration increment  $\Delta\alpha$  ( $a$  = particle radius,  $\lambda$  = wavelength,  $\alpha = \frac{2\pi a}{\lambda}$ ). This decision was based in large part on a note of Dave's<sup>[66]</sup> in which he pointed out the computational economies of increasing  $\Delta\alpha$  after the integration covers a certain fraction of the particles. In Dave's examples, the integration increment was kept at  $\Delta\alpha = 0.1$  until the fraction 0.99 of the particles had been processed, then increased to  $\Delta\alpha = 0.5$ . This is, of course, the simplest type of variable -  $\Delta\alpha$  scheme. A somewhat more complicated variant is now used in our code; it will be described below. The former Romberg scheme, while desirable for observing the convergence of the integrals, was not only computationally cumbersome, but required fixed  $\Delta\alpha$ . Hence, while useful as a research tool, it could not be retained for doing large numbers of more or less routine Mie computations.

Our present size distribution integration scheme errs on the side of caution in order to do the extreme cases ( $\lambda \rightarrow 0$ ) correctly, but in so doing undoubtedly takes too small an integration increment in other cases. Fortunately, when the Mie calculation uses tables of  $\sigma_{\text{sca}}$ ,  $\sigma_{\text{ext}}$ , and  $i_1 + i_2$ , the integration increment is fixed by the tables; it need not, therefore, be a source of concern, for even a greatly over-conservative  $\Delta\alpha$  is of little import to the trivial amount of computation necessary to produce the polydisperse Mie functions from these tables. When tables of  $\sigma_{\text{sca}}$ , etc., are not used, the initial integration increment is taken as:

$$\Delta\alpha = \min \left( 0.1, \frac{\alpha_{\text{max}} - \alpha_{\text{min}}}{200} \right) \quad (2.42)$$

where the interval of integration is  $[\alpha_{\min}, \alpha_{\max}]$ . This choice is based on a conversation with Dave in which he maintained that 0.1 was the largest  $\Delta\alpha$  one can safely use, but that  $\Delta\alpha$  must also be small enough to adequately resolve the interval  $[\alpha_{\min}, \alpha_{\max}]$  (i.e., to resolve  $n(\alpha)$ ). The increment is kept fixed until a fraction  $f$  of the particles have been integrated over, then the increment is allowed to double as many as  $n_d$  times before the integration is finally terminated. The criterion for increment-doubling is that the maximum relative change in any quantity being integrated, due to the previous integration step, be less than  $\delta_0$ . An acceptable set of parameters is

$$f = 0.99 \quad ,$$

$$n_d = 6 \quad ,$$

and

$$\delta_0 = 0.001 \quad .$$

However, these are definitely too conservative for most situations.

The effects of varying  $\Delta\alpha$ ,  $f$ ,  $n_d$ , and  $\delta_0$  were examined in several spectral regions for the Arctic stratus cloud whose size distribution is shown in Figure 3.8. It was found that an increment  $\Delta\alpha = 0.1$  is indeed necessary to accurately integrate  $\sigma_{sca}$ , etc., in the visible and down to  $\lambda \sim 0.3\mu$ , that somewhat larger increments ( $\Delta\alpha = 0.2$  at  $1\mu$ ) are permissible as the wavelength increases into the near IR, but that progressively smaller increments ( $\Delta\alpha = 0.05$  at  $11\mu$ ) must again be used in the IR. The  $\frac{\alpha_{\max} - \alpha_{\min}}{200}$  estimate of Equation (2.42) takes care of the IR quite well, and the 0.1 estimate takes care of the visible. Nevertheless, Equation (2.42) is shown by these studies to be too conservative through the near IR, a deficiency which can be remedied easily.



The fraction  $f$  must indeed be 0.99 for extreme cases such as  $\lambda \sim 0.3\mu$  - even values as large as 0.95 lead to error then. However, it has been found possible to decrease  $f$  somewhat for larger wavelengths. The largest value of  $\delta_0$  which leads to acceptable accuracy is 0.01, and generally the number of doublings  $n_d$  should be kept to 5 or 6. Decreasing  $\delta_0$  to 0.001 or less will usually suppress doubling for the longer wavelengths while allowing it to proceed for the shorter ones. This is desirable since Mie computations at longer wavelengths are relatively inexpensive anyway.

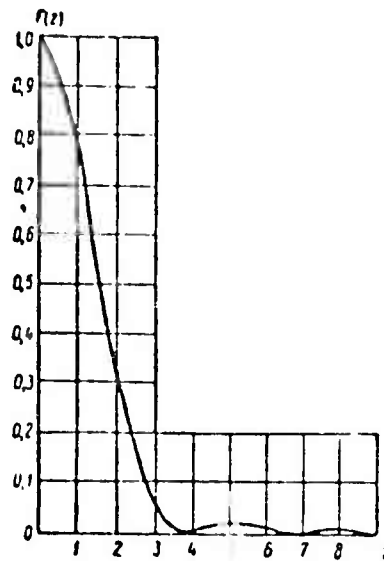
The forward (diffraction) peak in  $P_{v,M}$  for a particle of size parameter  $\alpha$  is proportional to

$$F(z) = \left( \frac{2 J_1(z)}{z} \right)^2$$

where  $z = \alpha \sin \theta$ , and  $J_1$  is the Bessel function of order one. This quantity is shown in Figure 2.3.

The actual forward peak will be a composite of the peaks for all  $\alpha \in [\alpha_{\min}, \alpha_{\max}]$ . The sharpest of the component peaks is due to  $\alpha = \alpha_{\max}$ , and therefore in order to resolve this peak, which varies substantially over  $\Delta z \approx \alpha_{\max} \Delta \theta = 1$ , we pick an angular increment

$$\Delta \theta_0 = \frac{1}{2 \alpha_{\max}}$$

Figure 2.3 - Graph of  $F(z)$ 

Actually, because the  $\pi_n$ 's and  $\tau_n$ 's entering the Mie series (Eqs. (2.36) and (2.37)) are pre-calculated with a predetermined angular mesh  $\Delta\theta_{\text{tab}}$ ,  $\Delta\theta_0$  is selected to be the closest multiple of  $\Delta\theta_{\text{tab}}$  to  $1/2 \alpha_{\text{max}}$ .  $\Delta\theta$  is also limited to be less than  $\theta_m$  (currently  $1^\circ$ ). The angular mesh on which  $P_{v,M}$  is calculated is then taken as a user-supplied and even number of steps of  $\Delta\theta_0$ , then  $2\Delta\theta_0$ , then  $4\Delta\theta_0$ , etc., with the restriction that no step is larger than  $\theta_{\text{max}}$  (currently  $2.5^\circ$ ). The number of steps of each size is even so that a piecewise Simpson quadrature can be used to integrate  $P_{v,M}$  in case truncation (Section 2.7.5) or renormalization (Section 2.7.7) is necessary.

### 2.7.5 Phase Function Truncation

Hansen<sup>[67]</sup> and Potter<sup>[68]</sup> have shown that the forward peak of the phase function  $P_{v,M}$  can be truncated without significantly changing the results of the transport calculation. Thus, for  $\theta \in [0, \theta^t]$ , where  $\theta^t$  is the truncation angle, the real phase function  $P_v(z, \theta)$  is 'replaced' (to within a normalization factor) by a truncated phase function  $P_{v,M}^t(z, \theta)$  in the manner of Figure 2.4. The logarithm of  $P_{v,M}^t$  is taken to be a linear function of  $\theta$  on  $[0, \theta^t]$  and the values of  $P_{v,M}^t$  and its derivative are matched to those of  $P_{v,M}$  at  $\theta = \theta^t$ .

Neither Hansen nor Potter propose a general method for selecting  $\theta^t$ . Therefore we devised the following procedure: If  $P_{v,M}$  for  $\theta = 0$  is less than a prescribed  $P_{\max}$  (currently 5),  $P_{v,M}$  is not truncated. Otherwise, truncation is attempted at a succession of  $\theta^t$ 's beginning near  $\theta = 0$  until either a successful truncation is achieved (such that  $P_{v,M}^t(z, 0) < P_{\max}$ ) or  $\theta^t$  exceeds  $\theta^T$  (currently  $20^\circ$ ). If  $\theta^t$  exceeds  $\theta^T$  first,  $P_{v,M}$  is truncated at  $\theta^T$  without regard to  $P_{\max}$ , provided only that  $P_{v,M}^t(z, 0) < P_{v,M}(z, 0)$ . If the latter procedure is unsuccessful,  $P_{v,M}$  is not truncated.

Mathematically, truncation amounts to approximating the forward peak,  $P_{v,M} - P_{v,M}^t$ , by a  $\delta$ -function:

$$\begin{aligned} P_{v,M} &= (P_{v,M} - P_{v,M}^t) + P_{v,M}^t \\ &\approx 4\pi F \delta(\vec{\Omega}' - \vec{\Omega}) + P_{v,M}^t \end{aligned}$$

where  $F$  may be determined by integrating both sides over all scattering angles

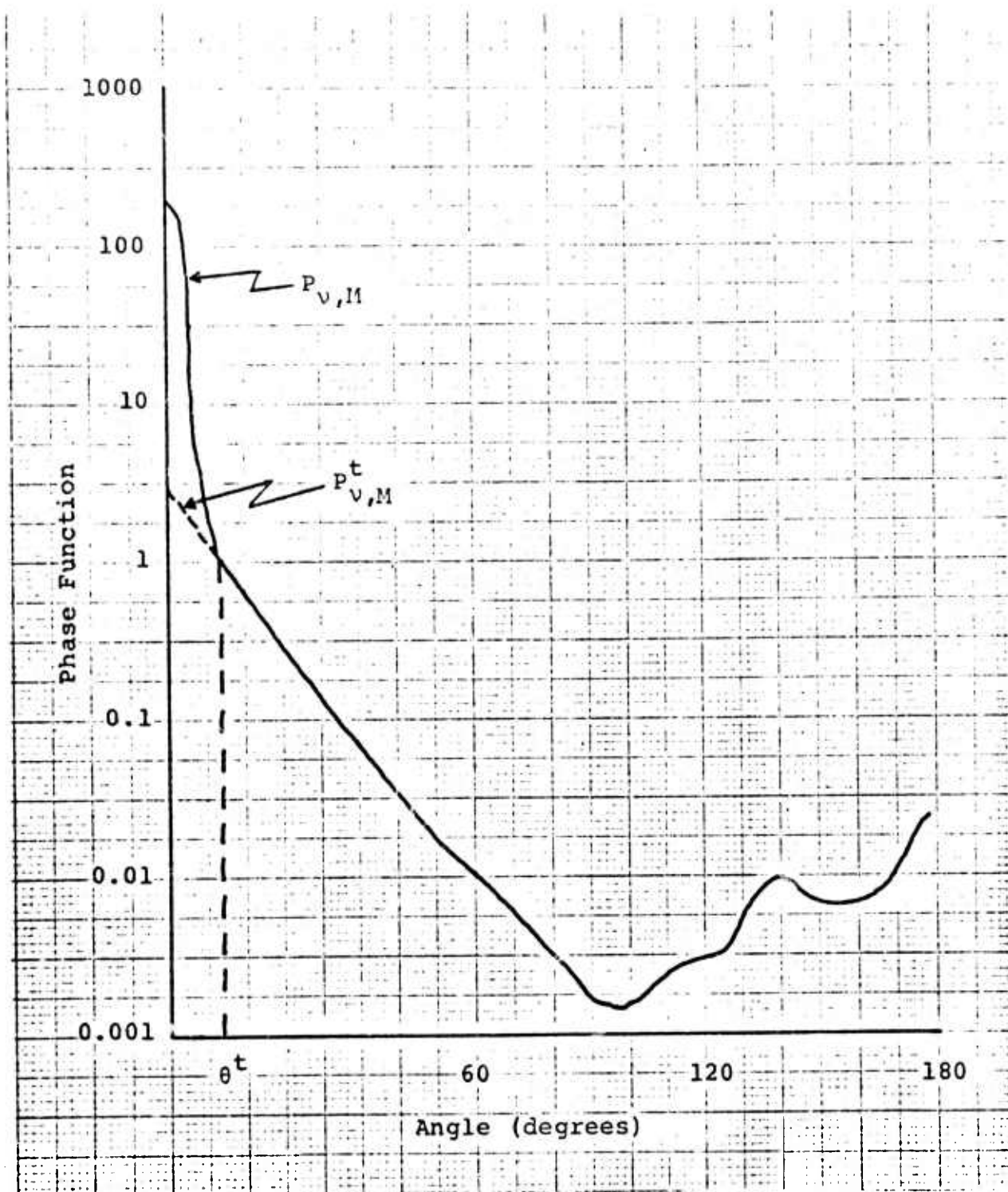


Figure 2.4 - Exact ( $P_{v,M}$ ) and Truncated ( $P_{v,M}^t$ ) Phase Function

$$\begin{aligned}
F &= \frac{1}{4\pi} \int_{4\pi} (P_{\nu,M} - P_{\nu,M}^t) d\Omega' \\
&= \frac{1}{2} \int_0^\pi [P_{\nu,M}(z, \theta) - P_{\nu,M}^t(z, \theta)] \sin\theta \, d\theta \\
&= \frac{1}{2} \int_0^{\theta^t} [P_{\nu,M}(z, \theta) - P_{\nu,M}^t(z, \theta)] \sin\theta \, d\theta \quad (2.43)
\end{aligned}$$

$F$  is determined numerically (in subroutine TRUNCT) using a Simpson quadrature.

Substituting the  $\delta$ -function approximation into the scattering terms of the radiative transfer equation (2.6), and eliminating subscripts and unnecessary arguments for brevity,

$$\begin{aligned}
\text{scat. terms} &= \frac{\beta}{4\pi} \int P(\vec{\Omega}, \vec{\Omega}') I(\vec{\Omega}') d\Omega' - \beta I(\vec{\Omega}) \\
&\approx \frac{\beta}{4\pi} \int [4\pi F \delta(\vec{\Omega}' - \vec{\Omega}) + P^t] I(\vec{\Omega}') d\Omega' - \beta I(\vec{\Omega}) \\
&= \frac{\beta(1-F)}{4\pi} \int \frac{P^t(\vec{\Omega}, \vec{\Omega}')}{1-F} I(\vec{\Omega}') d\Omega' - \beta(1-F) I(\vec{\Omega}) \\
&= \frac{\beta'}{4\pi} \int P'(\vec{\Omega}, \vec{\Omega}') I(\vec{\Omega}') d\Omega' - \beta' I(\vec{\Omega}) \quad ,
\end{aligned}$$

where

$$\beta' \equiv (1 - F)\beta \quad ,$$

$$P' \equiv \frac{P^t}{1 - F} \quad .$$

Therefore, the scattering terms have their original form, but  $P$  and  $\beta$  are replaced by  $P'$  and  $\beta'$  defined above.

#### 2.7.6 Azimuthal Integration

The aximuthally-averaged phase function  $\bar{P}_V$  (Eq. (2.5)), not  $P_V$  itself, is required in the ATRAD formulation of radiative transfer. The azimuthal average of the Rayleigh phase function (Section 2.7.1) is computed analytically in ATRAD, from

$$\begin{aligned}\bar{P}_R(\mu, \mu') &= \frac{c_1}{2\pi} \int_0^{2\pi} (1 + c_2 \mu_s^2) d\phi \\ &= \frac{c_1}{2\pi} \int_0^{2\pi} [1 + c_2 (\mu\mu')^2 + 2c_2 \mu\mu' \sqrt{(1-\mu^2)(1-\mu'^2)} \cos\phi \\ &\quad + c_2 (1-\mu^2)(1-\mu'^2) \cos^2\phi] d\phi \\ &= c_1 [1 + c_2 (\mu\mu')^2 + \frac{1}{2} c_2 (1-\mu^2)(1-\mu'^2)]\end{aligned}$$

where

$$c_1 = \frac{3(1 + \rho_n)}{4 + 2\rho_n} \quad c_2 = \frac{1 - \rho_n}{1 + \rho_n}$$

The azimuthal average of the Mie phase function is computed numerically using a Simpson Quadrature in order to reduce errors affecting the renormalization procedure (Section 2.7.7).

### 2.7.7 Renormalization of the Phase Function

There are two types of renormalization of the Mie phase function in ATRAD. The first operates on the Mie phase function  $P_{v,M}$  before azimuthal averaging, and consists in multiplying all values of  $P_{v,M}$  by the renormalization factor

$$\frac{2}{\int_{-1}^1 P_{v,M}(z, \mu_s) d\mu_s} \quad (2.44)$$

where the integral in the denominator is computed numerically using Simpson's Rule.

The second type of renormalization operates on the azimuthally averaged phase function  $P_{v,M}$  and is required by the Grant and Hunt algorithm (see Section 2.8) in order to preserve flux conservation. In terms of the Gaussian angular quadrature mesh  $0 < \mu_1 < \dots < \mu_m \leq 1$ , the numerical equivalent of the normalization condition

$$\int_{-1}^1 \bar{P}_{v,M}(z, \mu, \mu') d\mu = 2 \quad (2.45)$$

is

$$\sum_{j=1}^m c_j \rho_{jk} = 2 \quad (k = 1, \dots, m) \quad (2.46)$$

where

$$\rho_{jk} = P_{jk}^{++} + P_{jk}^{+-}$$

$$P_{jk}^{++} = \bar{P}_{v,M}(z, \mu_j, \mu_k)$$

$$P_{jk}^{+-} = \bar{P}_{v,M}(z, \mu_j, -\mu_k)$$

There are several reasons why  $\bar{P}_{v,M}$  will in general fail to satisfy Eq. (2.46). One is that Gaussian quadrature does not accurately represent Eq. (2.45); that is,  $\bar{P}_{v,M}$  may not closely approximate a polynomial in  $\mu$ . Also, errors are introduced in each step of the process by which  $\bar{P}_{v,M}$  is constructed:

- (a) the numerical computation of the Mie series (2.34)-(2.37)
- (b) the numerical integration over the aerosol size distribution, Eq. (2.41)
- (c) the numerical integration to obtain the truncation factor  $F$ , Eq. (2.42)
- (d) the numerical integration over azimuth.

Tests have been run to determine ATRAD's errors from each of the four sources (a)-(d); it has been determined that in no case do they exceed 1%. Hence, the necessity for renormalization will be almost entirely due to the inadequacy of Eq. (2.46) as an approximation to Eq. (2.45).

Let us assume that the corrected values  $\rho_{jk}$ , satisfying Eq. (2.46), are to be obtained from the calculated values  $\rho_{jk}^{calc}$  by applying a multiplicative correction,

$$\rho_{jk} = (1 + \epsilon_{jk}) \rho_{jk}^{calc}$$



Unfortunately, there are  $\frac{m(m-1)}{2}$  unknowns  $\epsilon_{jk}$  (the number is reduced from  $m^2$  by the symmetry requirement  $\epsilon_{kj} = \epsilon_{jk}$ ) and there are only  $m$  equations (Eqs. (2.46)) to determine them. This underspecification can be handled in many ways, no one of which seems much preferable on physical grounds over any other. Grant\* corrects only the diagonal elements,  $\epsilon_{jk} = \epsilon_j \delta_{jk}$ , and so has a determinate set of equations for the  $\epsilon_j$ . He points out that the phase matrices  $\rho_{jk}$  are usually strongly diagonally dominant and that his procedure thus incorporates the entire correction where it makes the smallest relative change.

An alternative procedure has been investigated. Assume

$$\epsilon_{jk} = \epsilon_j + \epsilon_k.$$

Then Eqs. (4.37) become

$$\sum_{j=1}^m (c_j \rho_{jk}^{\text{calc}} + b_k \delta_{jk}) \epsilon_j = 2 - b_k \quad (k=1, \dots, m)$$

where

$$b_k = \sum_{j=1}^m c_j \rho_{jk}^{\text{calc}}$$

and  $\delta_{jk}$  is the Kronecker delta. This is a determinate set of linear equations for the  $\epsilon_j$ .

Both Grant's method and our method of renormalization have been included as options in ATRAD. The effect of our

---

\*Private communication.

method is, in practice, similar to Grant's; the largest corrections are made to the diagonal elements of  $\rho_{jk}$ . Progressively smaller relative corrections result when an element is farther from the diagonal. However, our method offers the advantage of spreading the correction, while Grant's procedure concentrates it entirely on the diagonal element. In our opinion it is difficult to justify correcting only a subset of the  $\rho_{jk}$ 's.

Several test calculations have been run in which the Henyey-Greenstein phase function,

$$-\frac{1 - g^2}{(1 + g^2 - 2g\mu_s)^{3/2}}$$

was used for  $P_{v,M}$ , with  $g = 0.8$  and  $g = 0.95$  so that large forward scattering peaks were being tested. Twelve Gaussian angles ( $m=6$ ) were used. For these examples, it was found that reasonably large (up to 8% for  $g=0.8$  and up to 20% for  $g=0.95$ ) renormalization corrections were necessary. The results point up to the importance of truncation to ensure that  $\bar{P}_{v,M}$  can be treated by low-order Gaussian quadrature.

This model, however, leads to a phase function with a substantially altered area under its forward peak, and since this forward peak was often truncated and the scattering coefficient modified accordingly, the net impact of using the H-G option was often to cause a drastically different scattering coefficient to be used. In order to mitigate this circumstance, the parameter  $g$  is now chosen so that the area  $A$  under the real phase function between  $0^\circ$  and  $D^\circ$  (computed by a modified Simpson's rule) equals the area under the H-G approximation between  $0^\circ$  and  $D^\circ$ :

$$A = \int_{\mu_0}^1 \frac{1 - g^2}{(1 + g^2 - 2g\mu)^{3/2}} d\mu$$

$$\mu_0 = \cos D$$

This turns out to reduce to a cubic equation in  $g$ ,

$$A(2 - A)g^3 - 2(1 - A)[A + \epsilon(1 - A)]g^2 - [2A + A^2 + 4\epsilon(1 - A)]g + 2(A - \epsilon) = 0$$

where

$$\epsilon \equiv 1 - \mu_0$$

Studies of this cubic have shown that for realistic ranges of  $A$  and  $\epsilon$ , it has three real roots, one of which is always negative, one of which always exceeds one, and one of which lies between zero and one. The last root is the desired one.

The current H-G scheme has lost one thing which made the earlier scheme attractive - computational speed. The old scheme only required the value of the real phase function at  $\theta = 0^\circ$ ; the new one requires enough values to resolve the real phase function between  $0^\circ$  and  $D^\circ$ . As a result, the new scheme is only about a factor of 5 faster than a full Mie computation.

#### 2.7.8 Total Phase Function

The total phase function  $\bar{P}_V$  is obtained from  $\bar{P}_R$  and  $\bar{P}_{V,M}$  according to

$$\bar{P}_V = \frac{\beta_{V,R} \bar{P}_R + \beta_{V,M} \bar{P}_{V,M}}{\beta_V}$$

where

$$\beta_v = \beta_{v,R} + \beta_{v,M}$$

is the total volume scattering coefficient.

#### 2.7.9 Tables

The Mie computation is by far and away the most expensive part of ATRAD. For example, for a single wavelength  $\lambda = 0.33\mu$ , for the Arctic stratus cloud of Figure 3.8, 30 - 60 minutes of UNIVAC 1108 time (depending on the angular resolution in the phase function) is required. The time required is progressively less at longer wavelengths, but the sum of all these times for the 120 spectral intervals currently used by ATRAD amounts to many, many hours. Clearly, ATRAD could never be a satisfactory research tool if every problem with clouds or aerosols took so long to compute. The only answer was to split off the entire Mie computation as a separate code module, which then makes tables of  $\bar{\sigma}_{sca}$ ,  $\bar{\sigma}_{ext}$ , and  $P_{v,M}(\theta)$  to be read by ATRAD. Using these Mie tables, ATRAD can now be run for a typical cloud or aerosol problem in (UNIVAC 1108) times of the order of 5-10 minutes.

### 2.8 SOLUTION TO THE RADIATION TRANSFER EQUATION

The method of solution of the radiative transfer equation due to Grant and Hunt<sup>[69,70,71,72,73,74]</sup> has been chosen to solve the monochromatic problem arising in this section, Eqs. (2.30 through 2.33). Grant and Hunt's procedure requires no iteration in the presence of scattering, allows zones of arbitrary size, and is computationally economical. It brings together several lines of research in radiative transfer. On the one hand, it represents, for 1-D plane parallel problems,

the culmination of the discrete space formulation of transfer theory associated with Preisendorfer<sup>[75]</sup> and van de Hulst.<sup>[76]</sup> On the other hand, it reduces in the limit of small zone size to the differential formulation of Rybicki and Usher,<sup>[77]</sup> which represented an elegant formulation of the method of invariant imbedding. Lastly, it improves upon the  $S_n$  method<sup>[78]</sup> (by eliminating the need for zone-centered intensities) to the point where previous  $S_n$  methods for plane parallel geometry are now virtually obsolete.

The elimination of scattering iteration is a very significant feature of the Grant and Hunt method. Iteration methods, when optically thick clouds are present, would have been prohibitively expensive. Other attractive features of the method are:

- (1) a single inequality imposed on the "primary layer thickness"  $\Delta\tau_p$  (cf. Section 2.8.1) assures both positivity of intensities and computational stability;
- (2) flux is conserved provided only that the phase function  $\bar{P}_v$  is correctly normalized (cf. Section 2.7.7); and
- (3) error estimates are available.

More generally the Grant and Hunt method possesses a certain elegance, simplicity, and freedom from ad hoc assumptions which alternative methods lack.

The basis of the Grant and Hunt method is the interaction principle,

$$u^+(\tau_2) = t(\tau_2, \tau_1) u^+(\tau_1) + r(\tau_1, \tau_2) u^-(\tau_2) + \Sigma^+(\tau_1, \tau_2) \quad (2.47)$$

$$u^-(\tau_1) = r(\tau_2, \tau_1) u^+(\tau_1) + t(\tau_1, \tau_2) u^-(\tau_2) + \Sigma^-(\tau_1, \tau_2)$$

Figure 2.5 illustrates the various quantities involved in describing the interactions in the slab between  $\tau_1$  and  $\tau_2$ . The total optical depth coordinate is  $\tau$  and  $\mu = \cos \theta$  is the cosine of the angle between the ray and the vertical. The  $u^+$ 's are positively directed ( $\mu > 0$ ) intensities, the  $u^-$ 's negatively directed ( $\mu < 0$ ) intensities (the  $\mu$ -dependence is implicit). The  $r$ 's and  $t$ 's are integral operators representing reflection from and transmission through the slab  $[\tau_1, \tau_2]$ , and the  $\Sigma$ 's represent effective internal sources in  $[\tau_1, \tau_2]$ . We now approximate the angular integrals in the interaction principle by half-range Gaussian or Radau quadratures with weights  $c_i$  and angles  $0 < \mu_1 < \dots < \mu_m \leq 1$  ( $\mu_m = 1$  for Radau quadrature). (By using half-range quadrature, an idea originally due to Krook,<sup>[79]</sup> in which separate but symmetric quadrature formulas are used for  $0 \leq \mu \leq 1$  and  $-1 \leq \mu \leq 0$ , discontinuities in the intensity across  $\mu = 0$  ( $\theta = 90^\circ$ ) which may occur physically are allowed for.) The  $r$ 's and  $t$ 's become matrix operators, and the  $u$ 's and  $\Sigma$ 's become vectors:

$$u^\pm(\tau) = \begin{bmatrix} i_\nu(\tau, \pm\mu_1) \\ \vdots \\ i_\nu(\tau, \pm\mu_m) \end{bmatrix} \quad \Sigma^\pm(\tau_1, \tau_2) = \begin{bmatrix} \Sigma(\tau_1, \tau_2, \pm\mu_1) \\ \vdots \\ \Sigma(\tau_1, \tau_2, \pm\mu_m) \end{bmatrix} \quad (2.48)$$

where  $i_\nu$  has been written as a function of  $\tau$  rather than  $z$ . Eq. (2.47) will now be taken to be in this matrix-vector form.

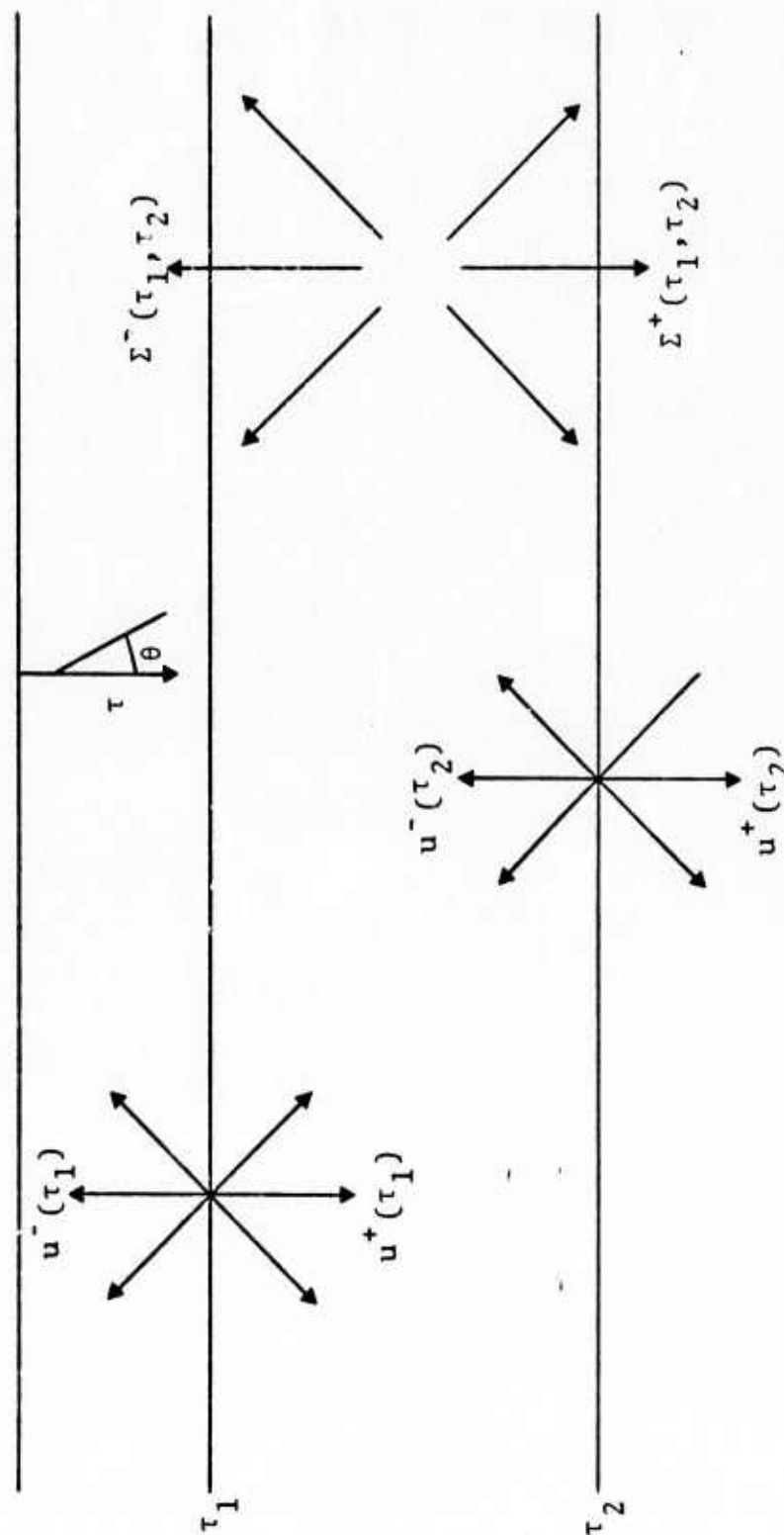


Figure 2.5 - Diagram of interaction principle.

For the sake of computational economy, we intend to use only a relatively few ( $m \leq 7$ ) angles. Therefore, the desirability of solving for the diffuse intensity  $i_v$  rather than the full intensity  $\bar{I}_v$ , which includes the solar flux, is apparent; if we used  $\bar{I}_v$ , many more angles  $\mu_i$  would be needed to resolve the solar peak, and these could no longer be distributed in the optimal (Gaussian) way. We are, of course, ignoring a possible specular reflection peak in  $i_v$ , which has not been subtracted out. (This would be of concern only over fairly smooth water surfaces.) Tests have been performed for a variety of situations which ensure that the angular discretization is adequate to determine fluxes accurately.

### 2.8.1 Layer Composition

We now consider how  $r$ ,  $t$ ,  $\Sigma$  for each zone are to be obtained. Each zone is divided into sub-layers called primary layers, which are optically thin enough that  $r$ ,  $t$ ,  $\Sigma$  for each primary layer can be obtained from the physical quantities  $B_v$ ,  $\bar{P}_v$ , etc. of the differential formulation, Eq. (2.22). Then the primary-layer  $r$ 's,  $t$ 's,  $\Sigma$ 's are "added up," by a process we shall call layer composition, to obtain  $r$ 's,  $t$ 's, and  $\Sigma$ 's for the entire zone.

The appropriate primary-layer quantities, derived by comparing the limits as  $\Delta\tau = \tau_2 - \tau_1 \rightarrow 0$  of Eqs. (2.47) with Eq. (2.30), are<sup>[70]</sup>

$$\begin{aligned}
 t(\tau_2, \tau_1) &= t(\tau_1, \tau_2) = I - M^{-1} \left[ I - \frac{\omega(\xi)}{2} P^{++}(\xi) c \right] \Delta\tau + O(\Delta\tau^2) \\
 r(\tau_2, \tau_1) &= r(\tau_1, \tau_2) = \frac{\omega(\xi)}{2} M^{-1} P^{+-}(\xi) c \Delta\tau + O(\Delta\tau^2) \\
 \Sigma^\pm(\tau_1, \tau_2) &= M^{-1} B^\pm(\xi) \Delta\tau + O(\Delta\tau^2)
 \end{aligned} \tag{2.49}$$



To  $O(\Delta\tau)$ ,  $t(\tau_2, \tau_1)$  and  $t(\tau_1, \tau_2)$  are identical; however, they may differ in  $O(\Delta\tau^2)$  terms. A similar remark applies to  $r$ . The various scalars, matrices, and vectors occurring in Eqs. (2.49) are defined as

$$\begin{aligned}\Delta\tau &= \tau_2 - \tau_1, & \tau_1 \leq \xi \leq \tau_2, \\ M &= [\mu_i \delta_{ij}] & , \quad c = [c_i \delta_{ij}] , \\ P^{++}(\tau) &= [\bar{P}_v(\tau, \mu_i, \mu_j)] = [\bar{P}_v(\tau, -\mu_i, -\mu_j)] , \\ P^{+-}(\tau) &= [\bar{P}_v(\tau, \mu_i, -\mu_j)] = [\bar{P}_v(\tau, -\mu_i, \mu_j)] , \\ \omega(\tau) &= \frac{\beta_v(\tau)}{\kappa_v(\tau)}\end{aligned}\tag{2.50}$$

$$\hat{B}(\tau, \mu) = [1 - \omega(\tau)] B_v(T(\tau)) + \frac{\omega(\tau)}{\beta_v(\tau)} Q_v(\tau, \mu)$$

$$B^\pm(\tau) = \begin{bmatrix} \hat{B}(\tau, \pm\mu_1) \\ \vdots \\ \hat{B}(\tau, \pm\mu_m) \end{bmatrix}$$

It is worthwhile to note that the error terms in Eqs. (2.49) will, in fact, be  $O(\Delta\tau^3)$  if  $\xi$  is chosen as the mid-point of  $[\tau_1, \tau_2]$ . This follows from Taylor's theorem.

In order to guarantee positive intensities, all elements of the primary-layer  $r$ - and  $t$ -matrices in Eq. (2.49) must be positive. Ignoring  $O(\Delta\tau^2)$  terms, this reduces to

the requirement that the diagonal elements of  $t$  be positive, which gives us the following restriction on  $\Delta\tau$  :

$$\Delta\tau < \Delta\tau_{\max} = \min_{1 \leq i \leq m} \left[ \frac{\mu_i}{1 - \frac{\omega(\xi)}{2} c_i \bar{P}_v(\xi, \mu_i, \mu_i)} \right] \quad (2.51)$$

It is also true that this property of positive elements in  $r$  and  $t$  is preserved by layer composition,<sup>[71]</sup> so that no restrictions beyond Eq. (2.51) are necessary.

The question of truncation error, that is, the error incurred by neglecting  $O(\Delta\tau^2)$  terms in Eqs. (2.49), is also of concern. Grant and Hunt have used as a practical criterion<sup>[71]</sup>

$$\Delta\tau = \frac{1}{2} \Delta\tau_{\max}$$

Grant\* has also made some estimates of the growth of truncation error during the process of layer composition. He finds that if  $T_n$  and  $R_n$  are the correct transmission and reflection matrices for a layer of thickness  $n\Delta\tau$ , and if this is built up by composing primary layers of thickness  $\Delta\tau$ , then the effect of small truncation errors  $\eta$  in  $T_1$  and  $\rho$  in  $R_1$  is to give approximate matrices  $t_n, r_n$  such that

$$\begin{aligned} ||T_n - t_n|| &< Cn\lambda^n(||\rho|| + ||\eta||) \\ ||R_n - r_n|| &< 2n(||\rho|| + ||\eta||) \end{aligned} \quad (2.52)$$

---

\* Private communication.

where  $C$  and  $\lambda$  are defined such that

$$||t_n|| < C\lambda^n \quad (0 < \lambda \leq 1)$$

and  $|| \quad ||$  is the norm of Ref. [71]. Thus, for fixed  $\Delta\tau$ , the absolute error in  $R_n$  and the relative error in  $T_n$  grow about linearly with  $n$ . If we use an approximation in which

$$||\rho|| + ||\eta|| = O(\Delta\tau^{\alpha+1})$$

and write  $n = H/\Delta\tau$  for fixed  $H$ , then

$$||T(H) - t(H)|| < KCH \lambda^n \Delta\tau^\alpha \quad (2.53)$$

$$||R(H) - r(H)|| < 2KH \Delta\tau^\alpha$$

so that the errors tend to zero as  $\Delta\tau \rightarrow 0$ . Currently, we intend to ignore  $O(\Delta\tau^2)$  terms in Eqs. (2.49), so that  $\alpha = 1$  (or  $\alpha = 2$  if  $\xi$  is taken as the mid-point).

The layer composition formulas are derived as follows. Suppose  $\tau_1 < \tau_2 < \tau_3$ . Write down the interaction principle (2.47) for the layer  $[\tau_1, \tau_2]$ , and again for the layer  $[\tau_2, \tau_3]$ . Eliminate  $u^+(\tau_2)$  and  $u^-(\tau_2)$  from two of these equations using the remaining two. Put the first two equations in the form of an interaction principle for the layer  $[\tau_1, \tau_3]$ . Then identify  $r_{13} \equiv r(\tau_1, \tau_3)$ , etc. from this principle. The results are

$$\begin{aligned}
r_{13} &= r_{23} + t_{32} \Gamma r_{12} t_{23} \\
r_{31} &= r_{21} + t_{12} \hat{\Gamma} r_{32} t_{21} \\
t_{31} &= t_{32} \Gamma t_{21} \\
t_{13} &= t_{12} \hat{\Gamma} t_{23} \\
\Sigma_{13}^+ &= t_{32} \Gamma (r_{12} \Sigma_{23}^- + \Sigma_{12}^+) + \Sigma_{23}^+ \\
\Sigma_{13}^- &= t_{12} \hat{\Gamma} (r_{32} \Sigma_{12}^+ + \Sigma_{23}^-) + \Sigma_{12}^-
\end{aligned} \tag{2.54}$$

where

$$\begin{aligned}
\Gamma &= (I - r_{12} r_{32})^{-1} \\
\hat{\Gamma} &= (I - r_{32} r_{12})^{-1} = I + r_{32} \Gamma r_{12}
\end{aligned} \tag{2.55}$$

In the special case when the layer  $[\tau_1, \tau_3]$  is homogeneous, (i.e., when  $\omega(\tau)$ ,  $P^{++}(\tau)$ , and  $P^{+-}(\tau)$  do not vary significantly across  $[\tau_1, \tau_3]$ ) and if the two layers  $[\tau_1, \tau_2]$  and  $[\tau_2, \tau_3]$  are of equal thickness  $\Delta\tau$ , then formulas (2.54) simplify somewhat:

$$\begin{aligned}
r_1 &\equiv r_{13} = r_{31} = r_0 + t_0 \Gamma_0 r_0 t_0 \\
t_1 &\equiv t_{13} = t_{31} = t_0 \Gamma_0 t_0 \\
\Sigma_1^+ &\equiv \Sigma_{13}^+ = t_0 \Gamma_0 (r_0 \Sigma_0^- + \Sigma_0^+) + \Sigma_0^+ \\
\Sigma_1^- &\equiv \Sigma_{13}^- = t_0 \Gamma_0 (r_0 \Sigma_0^+ + \Sigma_0^-) + \Sigma_0^-
\end{aligned} \tag{2.56}$$

where

$$\Gamma_0 = (I - r_0 r_0)^{-1}$$

and

$$r_0 \equiv r_{12} = r_{21} = r_{23} = r_{32}$$

$$t_0 \equiv t_{12} = t_{21} = t_{23} = t_{32} \quad (2.57)$$

$$\Sigma_0^{\pm} \equiv \Sigma_{12}^{\pm} = \Sigma_{23}^{\pm}$$

Relations (2.57) follow from Eqs. (2.49) by the assumptions of homogeneity and equal  $\Delta\tau$ 's. The single-subscript notation indicates that  $r$ ,  $t$ ,  $\Sigma$  depend on only one argument instead of two, that argument being the corresponding layer thickness. Defining

$$r_n = r(2^n \Delta\tau), \quad \text{etc.}$$

it is possible to continue the above process, called doubling, through any homogeneous region,

$$t_{n+1} = t_n \Gamma_n t_n$$

$$r_{n+1} = r_n + t_n \Gamma_n r_n t_n$$

$$\Sigma_{n+1}^+ = t_n \Gamma_n (r_n \Sigma_n^- + \Sigma_n^+) + \Sigma_n^+ \quad (2.58)$$

$$\Sigma_{n+1}^- = t_n \Gamma_n (r_n \Sigma_n^+ + \Sigma_n^-) + \Sigma_n^-$$

Doubling is much faster than simple layer addition as embodied in Eqs. (2.54). To add  $2^N$  primary layers comprising a homogeneous layer requires  $2^N - 1$  layer additions versus only  $N$  doublings.

In the future the code will allow for arbitrarily larger zones, which may or may not be homogeneous. If a zone is homogeneous, doubling will be used; if it is not, the code will partition it into sub-zones which are homogeneous, double within each of the sub-zones, and add the sub-zones using Eqs. (2.54). For now, however, the code will be constructed on the assumption that each zone is homogeneous. This is fairly restrictive, since it implies that neither the scattering nor the absorption coefficient vary substantially across a zone. No more than 40 zones should be necessary, however, and this does not seem overly burdensome (Grant and Hunt run with about 40 zones\*).

### 2.8.2 Source Doubling

The problem of an inhomogeneous source  $\Sigma^\pm$  in a zone which is otherwise homogeneous requires special attention. An inhomogeneous source region will occur frequently on account of the factor  $e^{-\tau/\mu_{\text{sun}}}$  in  $\hat{B}(\tau, \mu)$  and on account of the rapid variation of  $B_\nu(T)$  with  $T$  in many spectral regions. It turns out, however, that the most frequently occurring types of source inhomogeneity still admit a modified form of doubling. Inhomogeneous sources can be doubled right along with  $r$  and  $t$  with the resulting saving of computing time.

Let us begin by developing a general formula for source composition when the source variation across an otherwise homogeneous zone is described by  $f(\tau)$ . Referring to

---

\*Private communication.

Figure 2.6 and Eqs. (2.49), let the source vector for any one of the primary layers be

$$\Sigma_i^\pm = \Sigma_p^\pm f(\xi_i) \quad i = 1, \dots, 2^N \quad (2.59)$$

where  $\Sigma_p^\pm$  are independent of  $\tau$ , and  $\xi_i$  is the mid-point of primary layer  $i$ ,

$$\xi_i = \tau_0 + i\Delta\tau - \frac{\Delta\tau}{2} \quad (2.60)$$

Adding the sources in layers 1 and 2 according to Eq. (2.54), it is clear that the source  $\Sigma_{1+2}^\pm$  for the combined layer will be a linear combination of  $f(\xi_1)$  and  $f(\xi_2)$ :

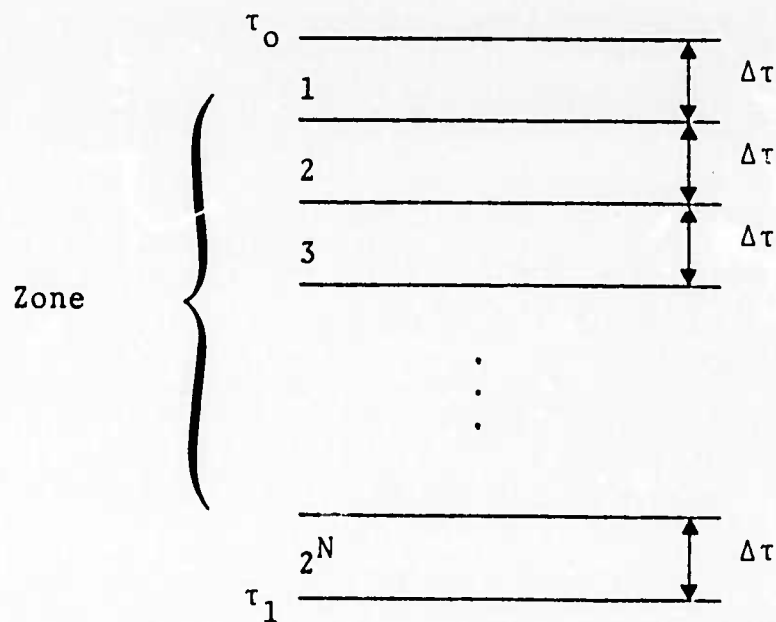


Figure 2.6 - Homogeneous zone composed of  $2^N$  primary layers.

$$\Sigma_{1+2}^{\pm} = V_1^{\pm(1)} f(\xi_1) + V_2^{\pm(1)} f(\xi_2)$$

(The expressions for the  $V$ 's are not of interest here.)  
Similarly, the source for the combined layer 3+4 involves only a change in the  $\xi$ 's:

$$\Sigma_{3+4}^{\pm} = V_1^{\pm(1)} f(\xi_3) + V_2^{\pm(1)} f(\xi_4)$$

Then, upon combining layers 1+2 and 3+4, a linear combination of  $f(\xi_1)$  through  $f(\xi_4)$  results:

$$\Sigma_{1+2+3+4}^{\pm} = \sum_{\ell=1}^4 V_{\ell}^{\pm(2)} f(\xi_{\ell})$$

Suppose that any  $2^n$  adjacent primary layers have been superposed in the above manner. Using the notation

$$\Sigma_{(i,n)}^{\pm} = \Sigma_{i+(i+1)+\dots+(i+2^n-1)}^{\pm}$$

where  $i$  denotes the first primary layer in the grouping, it is possible to prove by induction that

$$\Sigma_{(i,n)}^{\pm} = \sum_{\ell=1}^{2^n} V_{\ell}^{\pm(n)} f(\xi_{i+\ell-1}) \quad (2.61)$$

We now specialize our considerations to the solar source ( $f(\tau) = e^{-\tau/\mu_0}$ ) and the Planck source ( $f(\tau) = B_{\nu}(T(\tau))$ ). By the linearity of the source composition formulas (2.54) it is possible to compose the solar



source and Planck source separately and then simply add the results at the end to obtain the full source.

For the case of the solar source, the quantities  $\Sigma_p^\pm$  of Eq. (2.59) are, from Eqs. (2.49) and (2.50),

$$\Sigma_{p,sol}^\pm = \frac{S_v \omega(\bar{\tau})}{4\pi} \Delta\tau M^{-1} \begin{bmatrix} \bar{P}_v(\bar{\tau}, \pm\mu_1, \mu_0) \\ \bar{P}_v(\bar{\tau}, \pm\mu_m, \mu_0) \end{bmatrix} \quad (2.62)$$

Since  $\omega$  and  $\bar{P}_v$  are assumed not to vary across the zone, the argument  $\bar{\tau}$  refers to the mid-point of the entire zone in Figure 2.6. Now assume that, beginning with the  $\Sigma_{p,sol}^\pm$  and Eq. (2.59), the first  $2^n$  primary layers have been composed, so that the  $\Sigma_{(1,n)}^\pm$  are known. The adjacent  $2^n$  primary layers will then, by Eq. (2.61), have source vectors

$$\begin{aligned} \Sigma_{(1+2^n,n)}^\pm &= \sum_{\ell=1}^{2^n} v_\ell^{\pm(n)} f(\xi_{\ell+2^n}) \\ &= \sum_{\ell=1}^{2^n} v_\ell^{\pm(n)} e^{-(\tau_0 + (\ell+2^n)\Delta\tau - \frac{\Delta\tau}{2})/\mu_0} \\ &= e^{-2^n\Delta\tau/\mu_0} \Sigma_{(1,n)}^\pm \\ &= h_n \Sigma_{(1,n)}^\pm \end{aligned} \quad (2.63)$$

where

$$h_n = e^{-2^n \Delta\tau/\mu_0} \quad (2.64)$$

Remembering the definitions  $r_n = r(2^n \Delta\tau)$ , etc., the sources  $\Sigma_{(1,n+1)}^\pm$  for the combined layer, containing  $2^{n+1}$  primary layers, are

$$\begin{aligned} \Sigma_{(1,n+1)}^+ &= t_n \Gamma_n (r_n \Sigma_{(1+2^n,n)}^- + \Sigma_{(1,n)}^+) + \Sigma_{(1+2^n,n)}^+ \\ &= t_n \Gamma_n (r_n h_n \Sigma_{(1,n)}^- + \Sigma_{(1,n)}^+) + h_n \Sigma_{(1,n)}^+ \end{aligned} \quad (2.65)$$

$$\begin{aligned} \Sigma_{(1,n+1)}^- &= t_n \Gamma_n (r_n \Sigma_{(1,n)}^+ + \Sigma_{(1+2^n,n)}^-) + \Sigma_{(1,n)}^- \\ &= t_n \Gamma_n (r_n \Sigma_{(1,n)}^+ + h_n \Sigma_{(1,n)}^-) + \Sigma_{(1,n)}^- \end{aligned}$$

These are adaptations of the source composition formulas in Eqs. (2.54). From the definition of  $h_n$ , it is obvious that

$$h_{n+1} = h_n^2 \quad (2.66)$$

Together, Eqs. (2.65) and (2.66) form a doubling scheme for the solar (or any exponential) source. The scheme is initialized by

$$\Sigma_{(1,0)}^\pm = \Sigma_{p,sol}^\pm e^{-(\tau_0 + \frac{\Delta\tau}{2})/\mu_0} \quad (2.67)$$

$$h_0 = e^{-\Delta\tau/\mu_0}$$

and iterated from  $n = 0$  to  $n = N - 1$ .

In order to derive doubling formulas for the Planck source, it is necessary to have a more tractable functional form for  $f(\tau)$  than  $B_v(T(\tau))$ . It can be shown that it is reasonable to assume  $B_v$  is piecewise linear in  $\tau$ , so that

$$f(\tau) = B_v(T(\tau)) = B_0 + B'(\tau - \tau_0) \quad (2.68)$$

across the zone of Figure 2.6, where

$$B_0 \equiv B_v(T(\tau_0))$$

$$B' \equiv \frac{B_v(T(\tau_1)) - B_v(T(\tau_0))}{\tau_1 - \tau_0}$$

Expressing this in terms of  $\xi_i$  (see Eq. (2.60)),

$$\begin{aligned} f(\xi_i) &= B_0 + B'(\tau_0 + i\Delta\tau - \frac{\Delta\tau}{2} - \tau_0) \\ &= B'_0 + B' i\Delta\tau \end{aligned} \quad (2.69)$$

where

$$B'_0 = B_0 - B' \frac{\Delta\tau}{2}$$

The sources  $\Sigma_{(1,n)}^\pm$  for the first  $2^n$  primary layers then become

$$\Sigma_{(1,n)}^\pm = \sum_{\ell=1}^{2^n} V_\ell^\pm(n) (B'_0 + B' \ell \Delta\tau)$$

while for the adjacent  $2^N$  primary layers

$$\begin{aligned}\Sigma_{(1+2^n, n)}^{\pm} &= \sum_{\ell=1}^{2^n} V_{\ell}^{(n)} [B'_0 + B'(\ell+2^n)\Delta\tau] \\ &= \Sigma_{(1, n)}^{\pm} + 2^n B' \Delta\tau Y_n^{\pm}\end{aligned}\tag{2.70}$$

where

$$Y_n^{\pm} \equiv \sum_{\ell=1}^{2^n} V_{\ell}^{\pm(n)}$$

The  $Y_n^{\pm}$  refer to a constant source  $f(\tau) = 1$ , and so may be calculated by doubling as in Eqs. (2.58). A further simplification is that symmetry prevails,

$$Y_n \equiv Y_n^+ = Y_n^-$$

This is intuitively obvious, since a constant source would be expected to emit the same at  $-\mu$  as at  $+\mu$ . It can be proven inductively by first noting that the  $\Sigma_p^{\pm}$  of Eq. (2.59), which for the Planck source are,

$$\begin{aligned}\Sigma_{P, plk}^{\pm} &= [1 - \omega(\bar{\tau})] \Delta\tau M^{-1} \begin{bmatrix} 1 \\ 1 \\ \vdots \\ 1 \end{bmatrix} \\ &= [1 - \omega(\bar{\tau})] \Delta\tau \begin{bmatrix} 1/\mu_1 \\ \vdots \\ 1/\mu_m \end{bmatrix}\end{aligned}\tag{2.71}$$

are equal,

$$\Sigma_{P,plk} \equiv \Sigma_{P,plk}^+ = \Sigma_{P,plk}^-$$

Because  $f(\tau) \equiv 1$ ,

$$Y_0^\pm = \Sigma_{P,plk} \quad (2.72)$$

by Eq. (2.59), so that symmetry is proved for  $n = 0$ . If symmetry has been proved for a general  $n$ , then from the doubling formulas (2.58)

$$Y_{n+1}^+ = t_n \Gamma_n (r_n Y_n + Y_n) + Y_n$$

$$Y_{n+1}^- = t_n \Gamma_n (r_n Y_n + Y_n) + Y_n = Y_{n+1}^+$$

which completes the induction proof, and gives us the simplified doubling formula

$$Y_{n+1} = [I + t_n \Gamma_n (I + r_n)] Y_n \quad (2.73)$$

for  $Y_n$ .

The two layers, each containing  $2^n$  primary layers, are now composed just as for the exponential source (see Eq. (2.65)):

$$\begin{aligned}
\Sigma_{(1,n+1)}^+ &= t_n \Gamma_n \left[ r_n (\Sigma_{(1,n)}^- + 2^n B' \Delta\tau Y_n) + \Sigma_{(1,n)}^+ \right] \\
&\quad + \Sigma_{(1,n)}^+ + 2^n B' \Delta\tau Y_n \\
\Sigma_{(1,n+1)}^- &= t_n \Gamma_n \left[ r_n \Sigma_{(1,n)}^+ + \Sigma_{(1,n)}^- + 2^n B' \Delta\tau Y_n \right] + \Sigma_{(1,n)}^-
\end{aligned}
\tag{2.74}$$

Together, Eqs. (2.73) and (2.74) form a doubling scheme for the Planck (and any linear-in- $\tau$ ) source. The scheme is initialized by Eq. (2.72) and by

$$\Sigma_{(1,0)}^\pm = (B'_0 + B' \Delta\tau) Y_0 \tag{2.75}$$

and iterated from  $n = 0$  to  $n = N - 1$ .

More accurate piecewise polynomial approximations to  $B_\nu(T(\tau))$  are possible, at the expense of more complicated source doubling formulas. In particular, economical piecewise quadratic and piecewise cubic schemes have been derived and will be programmed at a future date to ascertain if the increased accuracy of the heating-rate calculations so obtained warrants the additional computational expense.

### 2.8.3 Forward and Backward Passes

By the procedures of Sections 2.8.1 and 2.8.2, we obtain reflection and transmission matrices and source vectors for every zone of the atmosphere. If the zone structure is

$$0 = \tau_1 < \tau_2 < \dots < \tau_{N+1}$$

and the notation is

$$u_n^\pm = u^\pm(\tau_n)$$

$$r_{n,n+1} \equiv r(\tau_n, \tau_{n+1})$$

(2.76)

$$t_{n,n+1} \equiv t(\tau_n, \tau_{n+1})$$

$$\Sigma_{n,n+1}^\pm = \Sigma^\pm(\tau_n, \tau_{n+1})$$

then according to the Grant and Hunt algorithm (whose derivation is lengthy and will not be repeated here) the solution for the intensity vectors  $u_n^\pm$  splits into two parts.

The first part is the forward pass. In the forward pass, the  $m \times m$  matrices  $E_n$ ,  $G_n$ , and  $H_n$  and the  $m$ -vectors  $V_n^{(1)}$ ,  $V_n^{(2)}$ , and  $V_n^{(3)}$  are calculated recursively as follows:

$$E_1 = 0 \quad V_1^{(1)} = V_1^{(2)} = V_1^{(3)} = 0 \quad (2.77a)$$

$$\tilde{\Gamma}_{n+1} = (I - r_{n+1,n} E_n)^{-1} \quad (2.77b)$$

$$H_{n+1} = \tilde{\Gamma}_{n+1} t_{n,n+1} \quad (2.77c)$$

$$G_{n+1} = E_n H_{n+1} \quad (2.77d)$$

$$E_{n+1} = r_{n,n+1} + t_{n+1,n} G_{n+1} \quad (2.77e)$$

$$V_{n+1}^{(1)} = \tilde{\Gamma}_{n+1} (r_{n+1,n} V_n^{(3)} + \Sigma_{n,n+1}^-) \quad (2.77f)$$

$$V_{n+1}^{(2)} = V_n^{(3)} + E_n V_{n+1}^{(1)} \quad (2.77g)$$

$$V_{n+1}^{(3)} = t_{n+1,n} V_{n+1}^{(2)} + \Sigma_{n,n+1}^+ \quad (2.77h)$$

$$(n = 1, 2, \dots, N)$$

The initialization of  $V_1^{(3)}$  at zero reflects the fact that there is no incident diffuse radiation at the top of the atmosphere,  $\tau = 0$  (the incident solar radiation is already accounted for by the transformation from  $T_v$  to  $i_v$ ). Economy of storage is achieved by performing the sub-layer superpositions, which yield the  $r$ 's,  $t$ 's, and  $\Sigma$ 's, simultaneously with the forward pass; in this way the  $r$ 's,  $t$ 's, and  $\Sigma$ 's need not be saved as a function of zone.

In order to identify certain quantities in the backward pass formulas, it is necessary to look at the surface boundary condition as stated in Section 2.4.

$$i_v(\tau_{N+1}, \mu) = f_b(|\mu|) + 2 \int_0^1 \mu' \bar{\rho}_v(\mu', |\mu|) \cdot i_v(\tau_{N+1}, \mu') d\mu' \quad (-1 \leq \mu < 0) \quad (2.78)$$

where

$$f_b(\mu) = \epsilon_v(\mu) B_v(T_g) + \frac{S_v}{\pi} \mu_0 \bar{\rho}_v(\mu_0, \mu) e^{-\tau_{N+1}/\mu_0}$$

Applying our half-range Gaussian quadrature to the integral in Eq. (2.78),



$$i_v(\tau_{N+1}, -\mu_i) = f_b(\mu_i) + 2 \sum_{j=1}^m c_j \mu_j \bar{\rho}_v(\mu_j, \mu_i) i_v(\tau_{N+1}, \mu_j)$$

$$(i = 1, \dots, m)$$

This can be written in matrix-vector form, using the notation of Eq. (2.76) as

$$u_{N+1}^- = w + r_G u_{N+1}^+$$

where

$$w = \begin{bmatrix} f_b(\mu_1) \\ \vdots \\ f_b(\mu_m) \end{bmatrix} \quad (2.79)$$

$$(r_G)_{ij} = 2c_j \mu_j \bar{\rho}_v(\mu_j, \mu_i) .$$

The backward pass may now be written

$$u_{N+1}^+ = (I - E_{N+1} r_G)^{-1} (E_{N+1} w + V_{N+1}^{(3)})$$

$$u_{N+1}^- = w + r_G u_{N+1}^+ \quad (2.80)$$

and

$$u_n^+ = G_{n+1} u_{n+1}^- + V_{n+1}^{(2)}$$

$$u_n^- = H_{n+1} u_{n+1}^- + V_{n+1}^{(1)} \quad (2.81)$$

$$n = N, N-1, \dots, 1$$

From the components  $i_v(\tau_n, \pm\mu_i)$  of the  $u_n^\pm$ , the fluxes are obtained:

$$\begin{aligned}
 F_v(\tau_n) &= 2\pi \int_{-1}^1 \mu i_v(\tau_n, \mu) d\mu + \mu_0 S_v e^{-\tau_n/\mu_0} \\
 &= 2\pi \int_0^1 [\mu i_v(\tau_n, \mu) - \mu i_v(\tau_n, -\mu)] d\mu \\
 &\quad + \mu_0 S_v e^{-\tau_n/\mu_0} \\
 &= 2\pi \sum_{i=1}^m c_i \mu_i [i_v(\tau_n, \mu_i) - i_v(\tau_n, -\mu_i)] \\
 &\quad + \mu_0 S_v e^{-\tau_n/\mu_0} - \mu_0 S_{v\rho\gamma, s}(\mu_0) e^{-[2\tau_{n+1} - \tau_n]/\mu_0}
 \end{aligned} \tag{2.82}$$

This completes the algorithm.

#### 2.8.4 Special Case of No Scattering in the Grant-Hunt Algorithm

In the case of negligible scattering it is not necessary to build up the solution from optically thin layers; simple analytic expressions for the reflection and transmission matrices and Planck source vectors can be derived for zones of arbitrary optical depth. These analytic expressions are obtained from the Grant-Hunt algorithm by taking the limit as the primary-layer thickness  $\Delta\tau_p$  goes to zero. For the reflection and transmission matrices of a zone of optical thickness  $\Delta\tau$ , we obtain

$$r_{ij} = 0$$

$$t_{ij} = e^{-\Delta\tau/\mu_i} \delta_{ij}$$

For a Planck source which varies linearly in  $\tau$ ,

$$B_v(\tau) = B_v(\tau_0) + B'_v(\tau - \tau_0)$$

where

$$B'_v = \frac{B_v(\tau_0 + \Delta\tau) - B_v(\tau_0)}{\Delta\tau}$$

we obtain for the  $j^{\text{th}}$  component of each source vector,

$$\Sigma_{\text{pl}k_j}^+ = B_v(\tau_0)(1 - e^{-\Delta\tau/\mu_j}) + \mu_j B'_v \left[ \frac{\Delta\tau}{\mu_j} - (1 - e^{-\Delta\tau/\mu_j}) \right]$$

$$\Sigma_{\text{pl}k_j}^- = B_v(\tau_0)(1 - e^{-\Delta\tau/\mu_j}) + \mu_j B'_v \left[ 1 - (1 + \frac{\Delta\tau}{\mu_j}) e^{-\Delta\tau/\mu_j} \right]$$

These special case results are incorporated in ATRAD.

## 2.9 FLOW DIAGRAM OF ATRAD

Figure 2.7 shows a brief flow diagram of the ATRAD Code. EVANS-TABLES makes tables of the exponential fits of transmission functions. I1I2-TABLES makes tables of the Mie scattering functions for single homogeneous spheres of varying sizes, but fixed index of refraction. MIE-TABLES makes tables of Mie scattering functions for spherical polydispersions. The dotted line correcting I1I2-TABLES and MIE-TABLES is meant to indicate that MIE-TABLES has the option of either generating its own values of  $\sigma_{\text{sca}}$ ,  $\sigma_{\text{ext}}$ , and  $i_1 + i_2$  or reading them from tables generated by I1I2-TABLES.



### 3. ATRAD APPLICATIONS

This chapter presents the results of comparisons between the ATRAD code and the radiation subroutine of the Mintz-Arakawa global circulation code. The Mintz-Arakawa treatment is discussed in Section 3.1. The test problem results are presented in Sections 3.2 - 3.5.

#### 3.1 THE MINTZ-ARAKAWA RADIATION SUBROUTINE

The calculation of radiation heating and cooling in the Mintz-Arakawa (M/A) global circulation model (GCM) is necessarily a considerably simplified one in order to keep the computational work within practicality. In order to determine the size of the errors which result from this simplified radiative treatment, a series of comparisons of fluxes and heating rates calculated with the first-principles radiative transfer code, ATRAD, and those from the Mintz-Arakawa two-level GCM are being made. The results of the first two comparison cases corresponding to cloud-free conditions over land are reported in Section 3.2. In order to make these comparisons we performed calculations of radiative quantities with the M/A radiative subroutine corresponding to a particular epoch in a standard global circulation calculation. (We are indebted to A. B. Kahle of RAND for the M/A computer code and for input data for it.) In the

following section we outline the features of the M/A radiative model and describe how the input data for it are transcribed to the ATRAD code.

The M/A treatment as employed in the climate dynamics program of the RAND Corporation is described by Gates, et.al. [1971], who give a definitive description of the formulation and code. We outline the principal features of the code here; however, we are particularly interested in specifying how the M/A atmosphere is constituted in order that we may provide a proper initialization for ATRAD.

The M/A radiative subroutine determines the radiative heating rate in two layers of the atmosphere and the radiative flux into the surface. Each of the layers contains one-half of the mass of the atmosphere lying below the 200 mb level. The part of the atmosphere above 200 mb is not explicitly contained in the M/A calculation but is included in ATRAD. The relevant radiative quantities to determine atmospheric heating are completely specified by giving the net radiative fluxes at the boundaries of these levels; in terms of the variable  $\sigma$  denoting the fraction of the atmosphere below 200 mb these are  $F(\sigma = 0)$  at the 200 mb level,  $F(\sigma = 0.5)$  in the middle of the atmosphere, and  $F(\sigma = 1.0)$  at the lower boundary of the atmosphere. These three altitudes are included among the zone boundaries of ATRAD for which radiative fluxes are calculated.

The radiative model of the M/A code distinguishes three spectral regions in which different radiative calculations are performed. Taking advantage of the fact that there is little overlap between the solar and thermal radiative sources, the major frequency division is between long-wave and short-wave radiation. The frequency dividing these regions is not specified in the M/A code but is chosen to be at

$4\mu$  for the purposes of editing data from ATRAD. In the long-wave region the M/A code takes account only of thermal emission and absorption by the atmosphere and the ground. In the short-wave case where thermal emission is neglected the spectrum is divided at  $0.9\mu$  into two parts; in the near IR region the solar radiation is assumed to be absorbed but unscattered, while in the remaining spectral interval it is assumed to be unabsorbed but Rayleigh scattered. Using these spectral intervals, the results of the M/A calculation can be presented as a matrix of nine net fluxes, corresponding to the three spectral intervals and the three altitudes.

The most important atmospheric absorber for typical atmospheric conditions is water vapor. The M/A calculation takes account principally of the effect of water vapor, incorporating empirical corrections for the effect of  $\text{CO}_2$ . Based on a single value  $Q_3$  of the water vapor mixing ratio at  $\sigma = 3/4$ , and an assumed saturated vapor pressure above 120 mb in the stratosphere, the code interpolates a profile of water vapor density. The vertical profile,  $Q$ , as a function of pressure,  $p$ , in mb is given by

$$Q = Q_3 \left( \frac{p}{p_3} \right)^k, \quad p \geq 120 \text{ mb},$$

$$Q = \frac{2.06255 \times 10^{-4}}{p}, \quad p < 120 \text{ mb}.$$
(3.1)

$p_3$  is the pressure at  $\sigma = 3/4$  and the constant  $k$  is determined by matching the values of  $Q$  at 120 mb:

$$k = \frac{\ln(Q_3/1.7188 \times 10^{-6})}{\ln(p_3/120 \text{ mb})} .$$

Using this profile the effective water vapor amount, including a factor for the pressure broadening of the absorption lines, is calculated between altitude levels. This quantity is subsequently used to form the absorptivity of each layer for the near IR short-wave radiation and the transmissivity of each layer for the IR radiation.

Equation (3.1) is also used to form the water vapor density input data for the ATRAD code. In addition, it is necessary to interpolate and extrapolate the temperature. The M/A code makes use of the calculated values of temperature  $T_1$  in the upper layer and  $T_3$  in the lower layer. From these values the temperatures at the 200 mb level and at the boundary between the upper and lower layer are found by invoking the following functional dependence of temperature on pressure:

$$T = \frac{\theta_3 - \theta_1}{p_3^\kappa - p_1^\kappa} (p^\kappa)^2 + \frac{\theta_1 p_3^\kappa - \theta_3 p_1^\kappa}{p_3^\kappa - p_1^\kappa} p^\kappa , \quad (3.2)$$

where  $\kappa = R/C_p$  and

$$\theta = T/p^\kappa$$

is proportional to potential temperature. Equation (3.2) insures that the prescribed values of temperature at  $p_1$  ( $\sigma = 1/4$ ) and  $p_3$  ( $\sigma = 3/4$ ) are recovered and in addition, the temperature becomes zero at  $p = 0$ . In addition, the air temperature near the ground at the top of the boundary layer,  $T_4$ , is also calculated in the M/A code from a consideration of



the fluxes of static energy between the ground and level 3 ( $\sigma = 3/4$ ). Subsequent adjustments of the original input temperatures may take place from convection. In order to specify the initial temperature profile for the ATRAD code, we use Eq. (3.2) from  $\sigma = 0$  to  $\sigma = 3/4$ . To determine temperatures from  $\sigma = 0.75$  to  $\sigma = 1.0$ , we use the same expression adjusted to match  $T_3$  and  $T_4$ :

$$T = \frac{\theta_4 - \theta_3}{p_4^K - p_3^K} (p^K)^2 + \frac{\theta_3 p_4^K - \theta_4 p_3^K}{p_4^K - p_3^K} p^K, \quad p_3 \leq p \leq p_4. \quad (3.3)$$

Finally, in the region above 200 mb, where the M/A code gives no guidance, we provide a rough simulation of the stratospheric temperature rise, using an expression which is continuous with  $T_0$  at  $p_0 = 200$  mb.

$$T = T_0 \frac{(p_0 + k_1)}{(p + k_1)}, \quad 0 \leq p \leq p_0. \quad (3.4)$$

Having specified the relation between temperature and pressure throughout the atmosphere, we can proceed to the determination of the altitude by using the hydrostatic relationship,

$$z - z_4 = \frac{R}{g} \int_p^{p_4} \frac{T}{p} dp,$$

where  $z_4$  is the altitude of the surface and we have neglected the effect of water vapor in the atmosphere. In view of the several analytic forms given above for the temperature-pressure relationship, we have approximated it by linear expressions,  $T = A + Bp$ , within each of the ATRAD zones which are of the order of 25 mb thick. The altitude of zone I becomes

$$Z(I) = Z(I-1) + \frac{R}{g} \left[ A \ln \frac{P(I-1)}{P(I)} + B(P(I-1) - P(I)) \right] , \quad (3.5)$$

where

$$A = \frac{T(I-1) P(I) - T(I) P(I-1)}{P(I) - P(I-1)}$$

and

$$B = \frac{T(I) - T(I-1)}{P(I) - P(I-1)} .$$

We have chosen  $Z(1) = 0$ , thereby measuring the altitude relative to the surface.

### 3.2 CALCULATIONS

Two different locations on the Earth's surface were chosen for comparison calculations. The criteria for choosing these locations were first, that they be the centers of grid squares in the M/A code, second, that the M/A code predict no clouds for the chosen points, and third, that the chosen points have substantially different water vapor profiles. Two such locations were found in the M/A run that was furnished to us. The first (Problem 1) was at 14°N, 20°E, in Chad (in the Sahara desert). The second (Problem 2) was at 18°S, 65°W, in Bolivia. Temperature profiles and water vapor profiles for the two problems, as extracted from M/A by the methods of the previous section, are shown in Figures 3.1 and 3.2, respectively. Since M/A does not calculate ozone profiles, an analytic ozone profile taken from Green, [81]

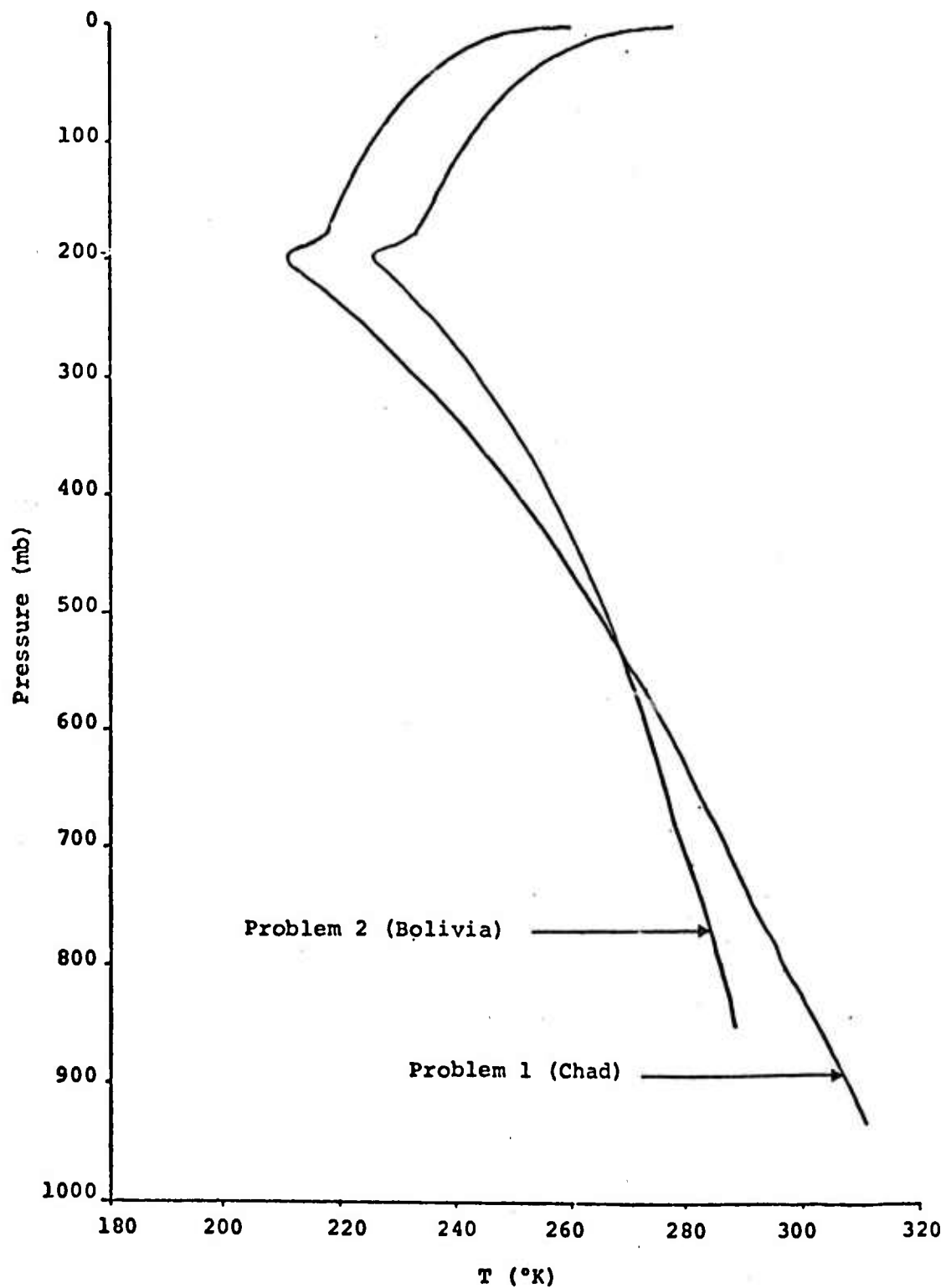


Figure 3.1 - Test Problem Temperature Profiles.

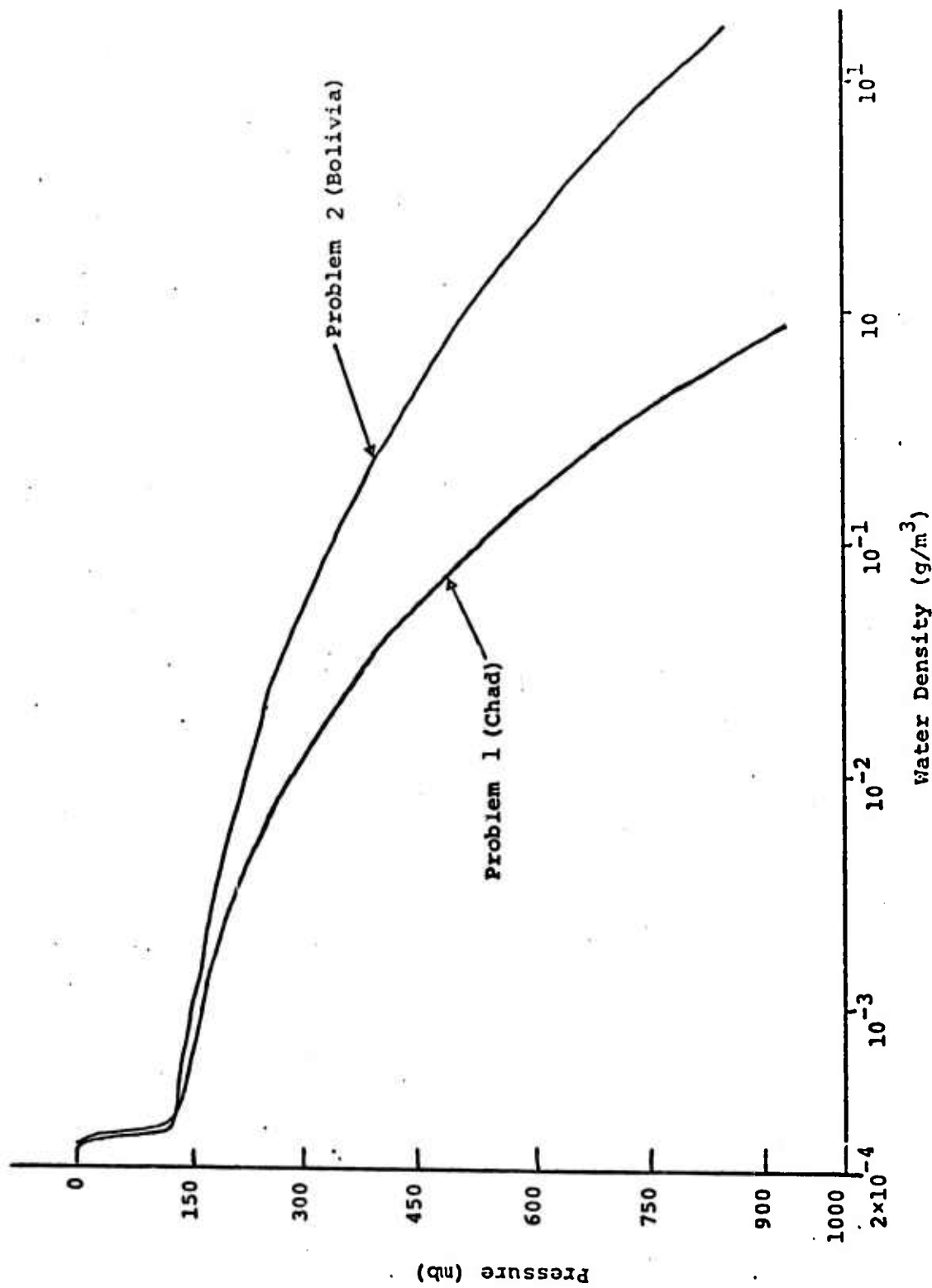


Figure 3.2 - Test Problem Water Vapor Density Profiles

$$\rho_{O_3}(z) = \frac{We \frac{(z-z_o)}{h}}{h \left[ 1 + e^{\frac{(z-z_o)}{h}} \right]^2}$$

was used with parameters  $W = 0.218$  atm-cm (total ozone),  $h = 4.5$  km (ozone layer half-width), and  $z_o = 23.25$  km (ozone maximum). This profile is shown in Figure 3.3.

The cosine of the solar zenith angle, ground temperature,  $T_g$ , and surface albedo for each problem were also taken directly from the M/A code. For Problem 1 they are

$$\mu_o = 0.84641818$$

$$T_g = 343.26^\circ K$$

$$\rho_v = \begin{cases} 0 & v < 2500 \text{ cm}^{-1} \\ 0.2 & v > 2500 \text{ cm}^{-1} \end{cases}$$

and for Problem 2,

$$\mu_o = 0.454845$$

$$T_g = 304.19^\circ K$$

$$\rho_v = \begin{cases} 0 & v \leq 2500 \text{ cm}^{-1} \\ 0.09 & v > 2500 \text{ cm}^{-1} \end{cases}$$

Note from Figure 3.1 that in both problems there is a temperature slip at the ground, of magnitude  $31.5^\circ K$  for Problem 1, and of magnitude  $15^\circ K$  for Problem 2.

Both problems were run with 39 zones, extending from the surface to 2 mb. A total of 116 frequency groups were

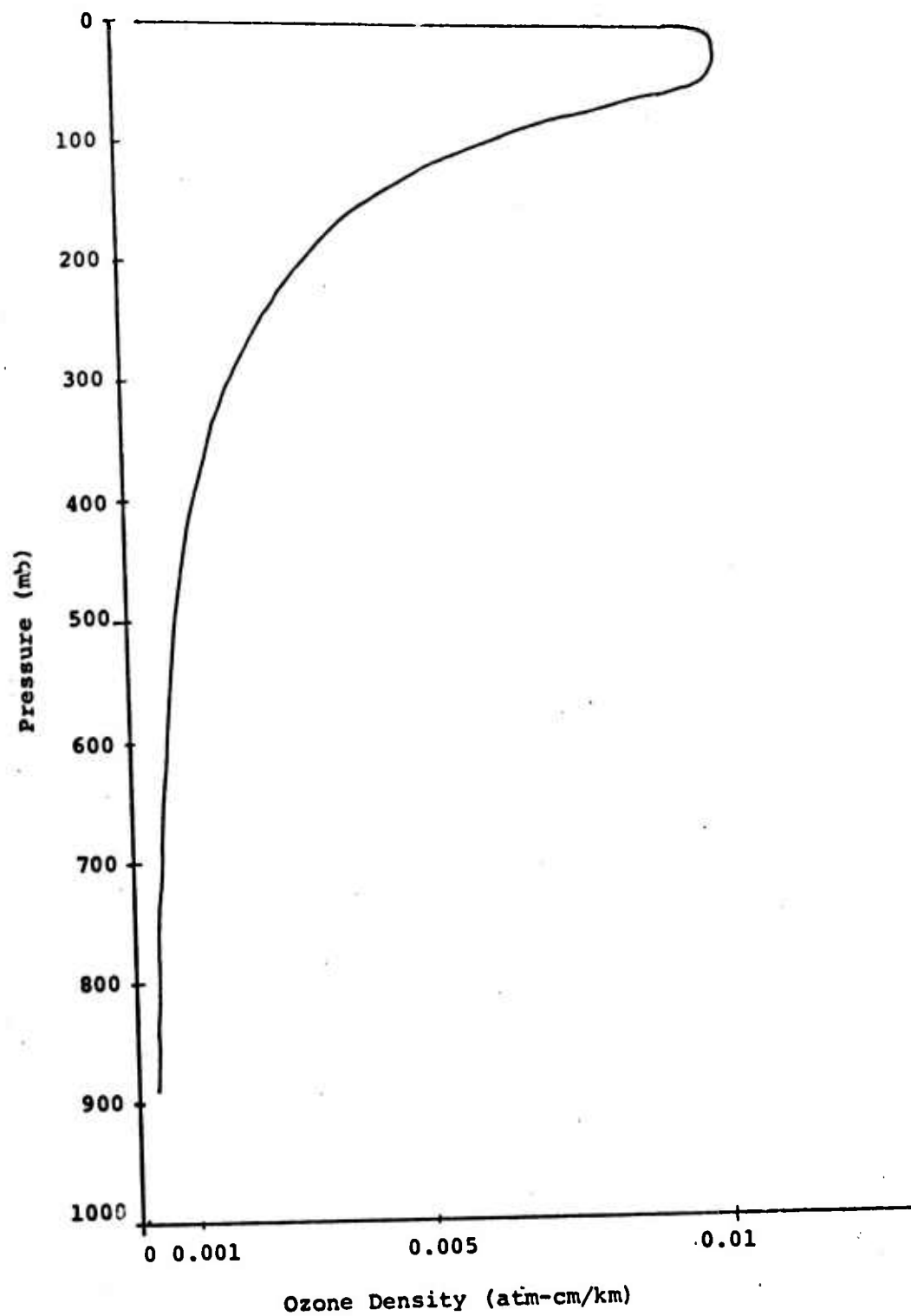


Figure 3.3 - Test Problem Ozone Density Profile

used, 32 in the IR ( $60\text{-}2500\text{ cm}^{-1}$ ) 29 in the near IR ( $2500\text{-}11,000\text{ cm}^{-1}$ ) and 55 in the "visible" ( $11,000\text{-}50,000\text{ cm}^{-1}$ ). A variable number of Gaussian angles was used: 6 between 60 and  $800\text{ cm}^{-1}$ , 10 between 800 and  $1400\text{ cm}^{-1}$ , 8 between 1400 and  $2500\text{ cm}^{-1}$ , and 10 between 2500 and  $50,000\text{ cm}^{-1}$ . Fewer angles were used in the strong water vapor and  $\text{CO}_2$  absorption bands, based on sample calculations showing a high degree of hemispherical isotropy in the intensity in these bands. Test calculations were run with more angles in selected frequency groups to determine if the number of angles being used was sufficient; in no case did the fluxes vary by more than a percent upon using more angles.

Test calculations were also performed to ascertain if the fluxes were sensitive to variations in the exponential fitting process. As we pointed out in Section 2.5, the exponents and coefficients resulting from this process are highly sensitive to perturbations in the transmission function data, but the conjecture was made that the fluxes and intensities would be insensitive to variations in the fit. In the test calculations, various small perturbations in the transmission function data, which produced large perturbations in the exponential fits, nevertheless produced only small perturbations (always less than 1 percent) in the fluxes. Hence, our previous conjecture has been borne out remarkably well.

The ATRAD frequency-integrated radiative flux  $F(z)$  for Problem 1 is given in Figure 3.4 as a function of pressure  $p(z)$ . (NOTE: positive fluxes are downward directed, negative fluxes are upward directed.) The Problem 1 atmosphere is very dry, which is manifested in the near constancy of  $F$  throughout most of the atmosphere. The large change in  $F$  near the surface can be explained in terms of the large temperature slip

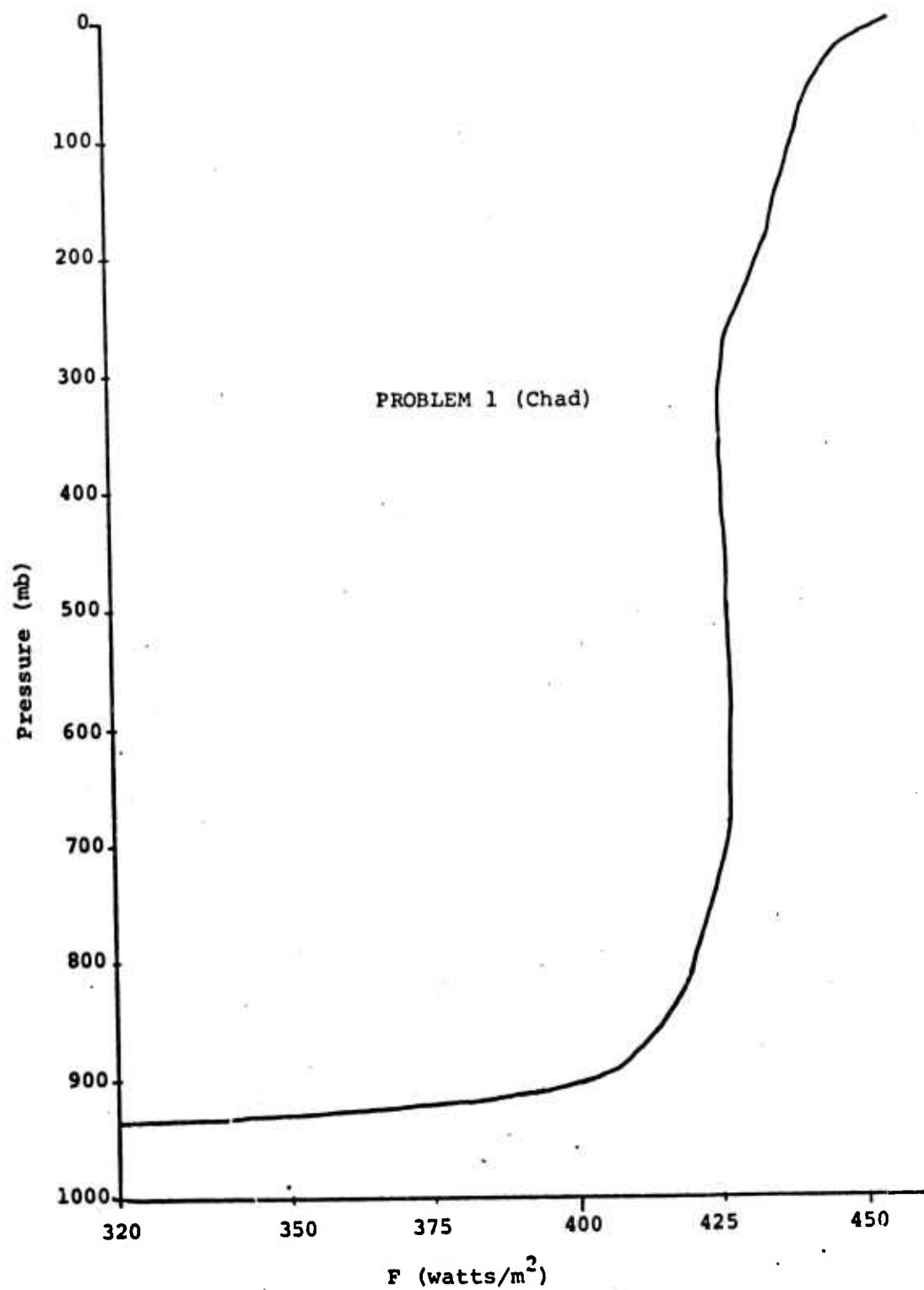


Figure 3.4 - Total (frequency-integrated) radiative flux profile from ATRAD, Problem 1



(31.5°) at the surface; this slip produces a large upward blackbody flux which decreases the downward flux and which penetrates several hundred meters upward before absorption and re-emission by water vapor can produce a cancelling downward flux.

The Problem 1 flux spectrum  $F_\nu(z)$  for  $z = 0$  (top of the atmosphere) and  $z = z_0$  (surface) is plotted as a function of wavenumber  $\nu$  in Figure 3.5. Actually, because of the logarithmic wavenumber scale,  $\nu F_\nu$  rather than  $F_\nu$  is plotted; the relationship

$$\int \nu F d(\ln \nu) = \int F d\nu$$

then insures that the area between the curve and the horizontal axis in any wavenumber interval is really the integrated flux. Prominent absorption features due to  $\text{CO}_2$  around  $700 \text{ cm}^{-1}$  ( $15\mu$  band),  $\text{O}_3$  around  $1000 \text{ cm}^{-1}$  ( $9.6\mu$  band),  $\text{H}_2\text{O}$  in the near IR (5 strong bands between  $2500$  and  $12,000 \text{ cm}^{-1}$ ), and  $\text{O}_3$  in the ultraviolet ( $35,000$ - $50,000 \text{ cm}^{-1}$ ) are all visible in this spectrum.

Comparisons between ATRAD's and Mintz-Arakawa's radiative fluxes and "heating rates" are presented in Table 3.1 for Problem 1. The "heating rate" table simply contains flux differences from the flux table above it. The error in the M/A net heating rate is quite large for this problem — it is too small by about a factor of 2 for the lower level, and too large by a factor of 4 and of the wrong sign for the upper level. The M/A flux into the ground is too large by almost  $100 \text{ watts/m}^2$ , or about 31 percent. The M/A fluxes are in general considerably more accurate than the M/A heating rates.

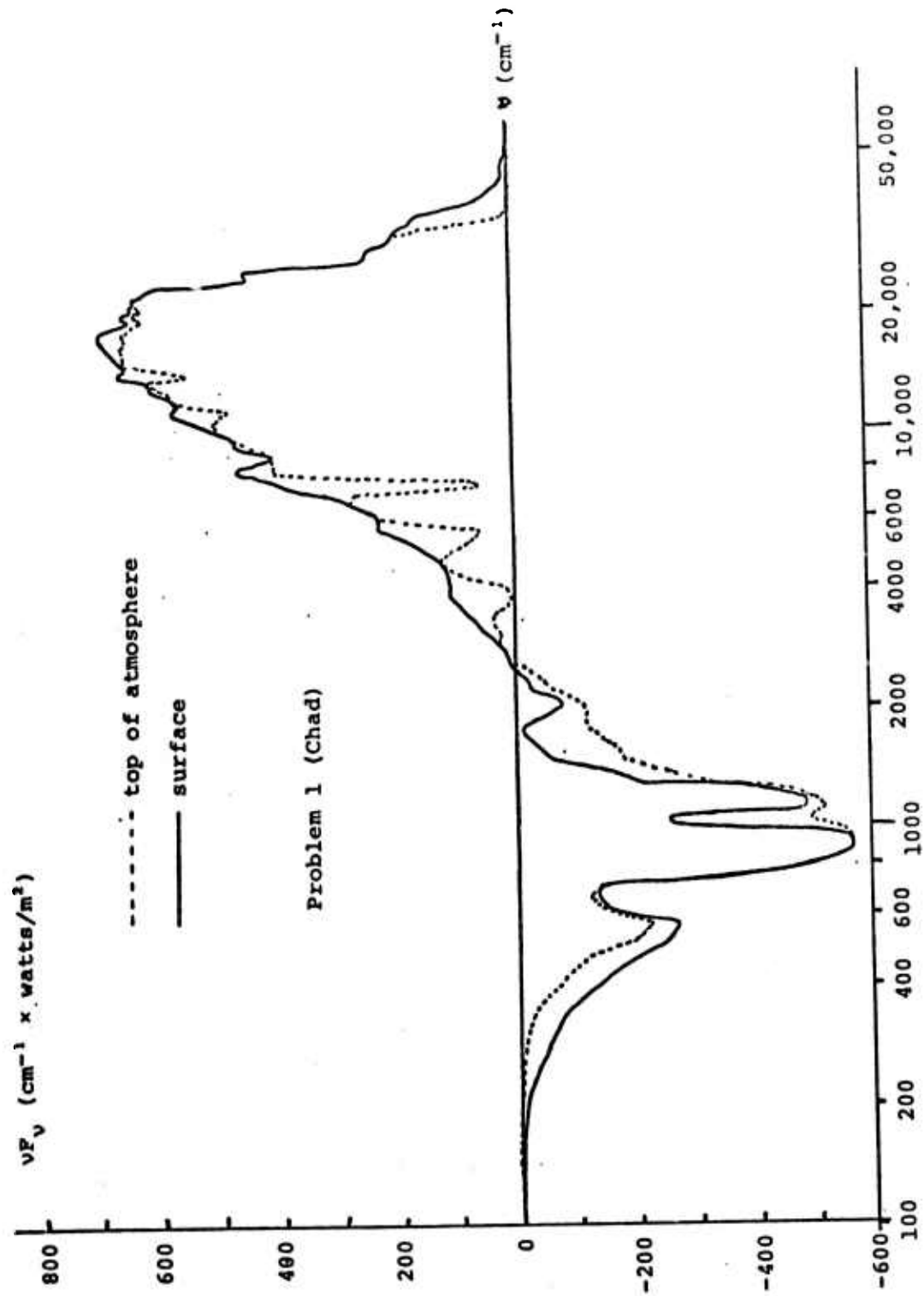


Figure 3.5 - Radiative flux spectrum at the surface and at the top of the atmosphere from ATRAD, Problem 1

TABLE 3.1

Comparison between ATRAD and Mintz-Arakawa (in parentheses)  
fluxes and heating rates, Problem 1

FLUX (WATTS/M<sup>2</sup>)

	$\sigma = 0$ (200 MB)	$\sigma = 0.5$ (567 MB)	$\sigma = 1.0$ (934 MB)
IR (60 - 2,500 CM <sup>-1</sup> )	-452.3 (-471.8)	-425.7 (-422.3)	-484.2 (-438.0)
NEAR IR (2,500 - 11,000 CM <sup>-1</sup> )	337.2 (343.6)	307.3 (319.0)	261.9 (283.1)
VISIBLE (11,000 - 50,000 CM <sup>-1</sup> )	548.1 (572.2)	545.4 (572.2)	542.3 (572.3)
VISIBLE + NEAR IR	885.3 (915.9)	852.6 (891.3)	804.2 (855.3)
NET	433.0 (444.1)	426.9 (469.0)	319.9 (417.3)

HEATING RATES (WATTS/M<sup>2</sup>)

	$\sigma = 0.25$	$\sigma = 0.75$	SURFACE
IR	-26.6 (-49.5)	58.5 (15.8)	-484.2 (-438.0)
NEAR IR	30.0 (24.6)	45.4 (35.9)	261.9 (283.1)
VISIBLE	2.7 (0)	3.1 (0)	542.3 (572.3)
NET	6.1 (-24.9)	107.0 (51.7)	319.9 (417.3)

$\sigma$  = dimensionless pressures

$$= \frac{P - P_{\text{reference}}}{P_{\text{surface}} - P_{\text{reference}}}$$

= 1.0 at surface

= 0 at  $p = 200$  mb

This illustrates the fact that crude models to obtain radiative fluxes perform reasonably well in practice but flux differences obtained from such models can be grossly in error. It is necessary to have quite an accurate flux computation if flux differences are desired, for in the process of differencing one or even two significant figures of accuracy may be lost.

The ATRAD frequency-integrated flux  $F(z)$  for Problem 2 is given in Figure 3.6. The Problem 2 atmosphere has considerably more water vapor at all levels than the Problem 1 atmosphere — a factor of 12 more in total water content and a factor of 19 more at the surface — which explains the slow decrease of  $F$  with altitude (the higher in the atmosphere one is, the stronger the upward flux due to water vapor emission becomes, which cancels more of the downward solar flux). As in Problem 1, the sharp flux change near the surface is ascribed to the temperature slip ( $15^\circ$ ). The change is much more abrupt in Figure 3.6 than in Figure 3.4 because the air near the surface is so much wetter, causing the water vapor emission to cancel the temperature slip flux a very short distance above the surface.

The Problem 2 flux spectrum  $F_\nu(z)$  is given in Figure 3.7 for  $z = 0$  and  $z = z_0$ . For the same reasons as in Figure 3.5,  $\nu F_\nu$  rather than  $F_\nu$  is plotted. Note that the near IR  $H_2O$  absorption features are enhanced, and that the  $CO_2$   $15\mu$  and  $O_3$   $9.6\mu$  features are more washed out, with respect to Problem 1. This is because of the increased amount of water vapor in Problem 2.

The comparison of ATRAD with M/A for Problem 2 is presented in Table 3.2. The M/A and ATRAD fluxes agree much more closely for Problem 2 than they did for Problem 1. The M/A

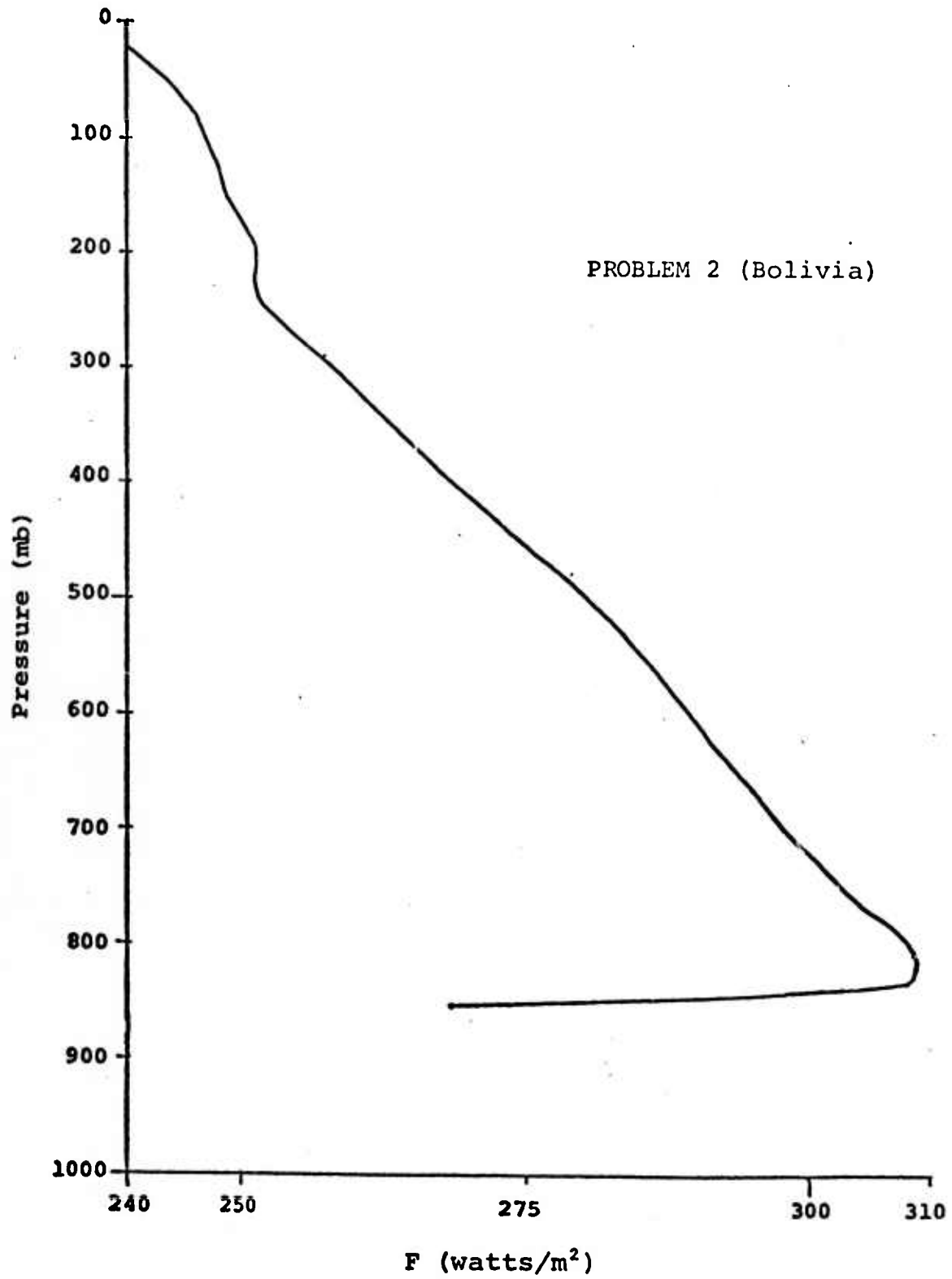


Figure 3.6 - Total (frequency-integrated) radiative flux profile, Problem 2

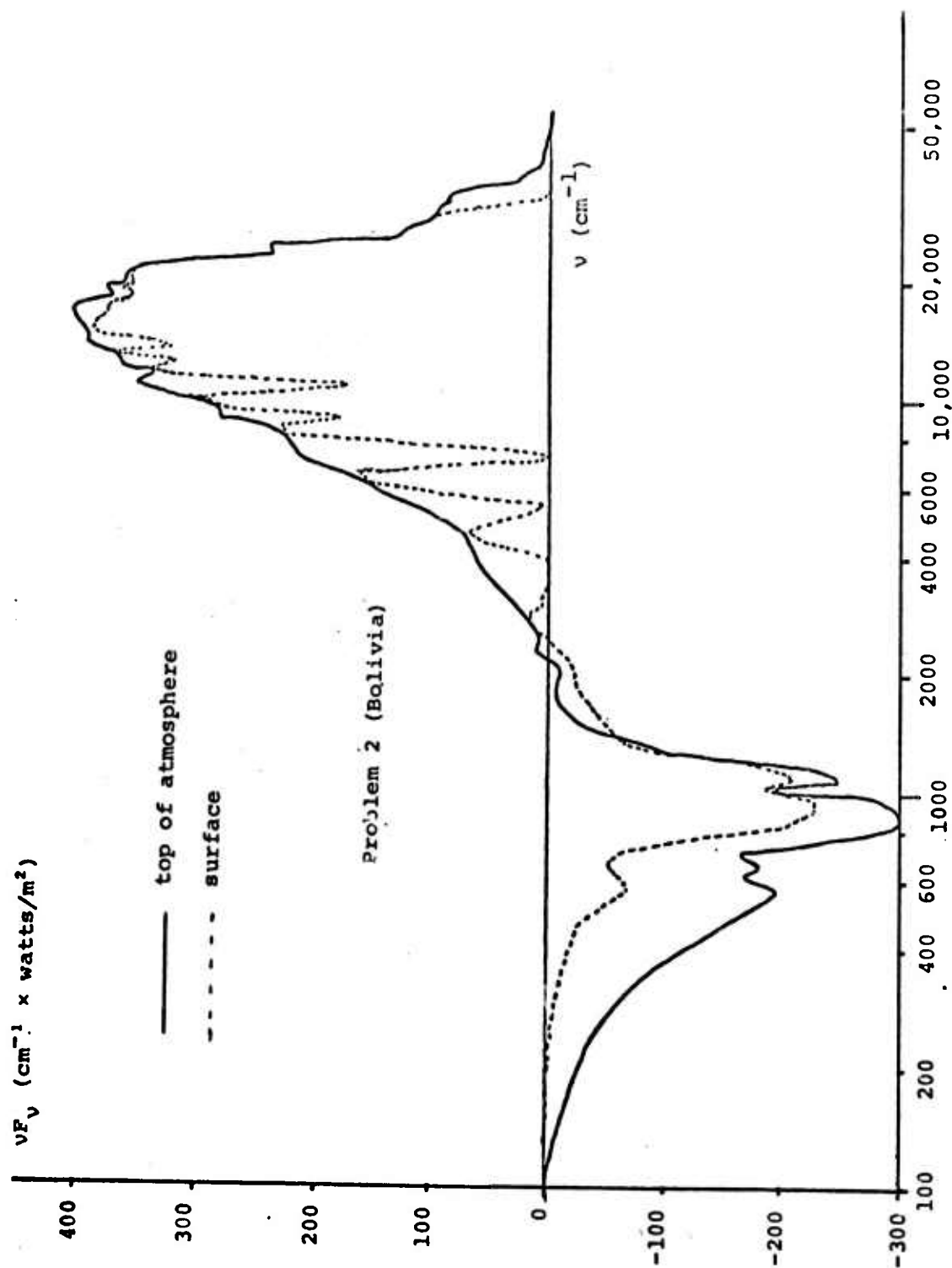


Figure 3.7 - Radiative flux spectrum at the surface and at the top of the atmosphere, Problem 2

TABLE 3.2

Comparison between ATRAD and Mintz-Arakawa (in parentheses)  
fluxes and heating rates, Problem 2

FLUX (WATTS/M<sup>2</sup>)

	$\sigma = 0$ (200 MB)	$\sigma = 0.5$ (526 MB)	$\sigma = 1.0$ (852 MB)
IR (60 - 2,500 CM <sup>-1</sup> )	-266.3 (-271.8)	-195.9 (-208.2)	-161.9 (-181.5)
NEAR IR (2,500 - 11,000 CM <sup>-1</sup> )	203.1 (209.2)	166.2 (179.3)	123.7 (121.2)
VISIBLE (11,000 - 50,000 CM <sup>-1</sup> )	314.5 (318.0)	312.4 (318.0)	306.6 (318.0)
VISIBLE + NEAR IR	517.6 (527.2)	478.6 (497.3)	430.3 (439.2)
NET	251.4 (255.5)	282.7 (289.2)	268.4 (257.7)

HEATING RATE (WATTS/M<sup>2</sup>)

	$\sigma = 0.25$	$\sigma = 0.75$	SURFACE
IR	-70.4 (-63.6)	-34.0 (-26.6)	-161.9 (-181.5)
NEAR IR	36.9 (29.9)	42.5 (58.1)	123.7 (121.2)
VISIBLE	2.2 ( 0 )	5.7 ( )	306.6 (318.0)
NET	-31.3 (-33.7)	14.3 (31.4)	268.4 (257.7)

$\sigma$  = dimensionless pressures

$$= \frac{p - p_{\text{reference}}}{p_{\text{surface}} - p_{\text{reference}}}$$

= 1.0 at surface

= 0 at  $p = 200$  mb

net flux errors are 1.6 percent for  $\sigma = 0$ , 2.3 percent for  $\sigma = 0.5$ , and 4 percent for  $\sigma = 1.0$ . Again, however, because of loss of significance in subtraction, the heating rate errors are substantially larger. The M/A heating rate in the lower level is too large by more than a factor of 2, and in the upper level is in error by 7.7 percent. The M/A surface flux ( $\sigma = 1$ ), which determines the heating of the ground, is in error by 4 percent. Thus, the M/A radiation model makes very good predictions of fluxes and heating of the lower level. It is not surprising that the M/A radiation model performs substantially better on Problem 2 than it did on Problem 1, for it devotes a great deal of attention to water vapor absorption, and Problem 2 is much more dominated by water vapor absorption than Problem 1.

It is clear that the M/A radiation model incurs substantial error in the case of dry atmospheres. However, no definitive conclusions with respect to the usefulness of the M/A radiation model for global climate calculations can be drawn from just these two problems. Many more test calculations, including cases with clouds, cases with realistic aerosol distributions, cases with high albedo (such as in the Arctic), and nighttime cases, need to be performed in order to obtain a more complete picture.

Even when this picture is obtained, other factors need to be considered. For example, the magnitude of the error in the total heating rate, including latent heating, adiabatic heating, etc., produced by errors in the radiative contribution must be ascertained. Also, it might be the case that a radiation model whose averaged (zonally, diurnally, etc.) predictions are correct is sufficient for climate dynamics calculations. In that case, it would be the average of many ATRAD calculations which would have to be compared with



the average of many M/A radiation calculations. The questions raised in this paragraph will have to be addressed before the amount of improvement necessary in the M/A radiation model can be ascertained.

### 3.3 ARCTIC STRATUS PROBLEM

The choice of an Arctic stratus problem for our first cloudy calculation with ATRAD may at first sight seem somewhat strange, but there are several good reasons for it. First, we were involved in some radiation studies for AIDJEX (Arctic Ice Dynamics Joint Experiment) upon which this problem bears directly. Second, Arctic problems come very close to satisfying the ATRAD assumption (see Section 2.1) of horizontal homogeneity, both with respect to the surface and with respect to the stratus cloud deck. Obviously, this assumption needs to be examined, but not before ATRAD is tested in situations which closely approximate horizontal homogeneity. Third, measurements were made on three different days with widely varying albedos, but similar cloud conditions so that a stringent test of ATRAD's response to albedo variation alone was possible. And, localized albedo measurements in the Arctic can, with greater assurance than in lower latitudes, be taken as representative of larger areas because of the lack of substantial variations in the terrain. Finally, cloud size distribution measurements were available, which is unfortunately not always the case when radiation measurements are made.

#### 3.3.1 Comparison of ATRAD with Experiment

The measurements to which we will compare ATRAD are reported in Weller, et. al.,<sup>[82]</sup> and were made near Pt. Barrow, Alaska, during the month of June 1971 when the snow was melting. The data consist of ground-level solar down-fluxes

(0.3 - 2.6 $\mu$ ), albedos, and solar elevations for three different days, and are shown in Table 3.3. Also shown are the flux measurements "interpolated to 30°" according to Weller, et. al., and the corresponding ATRAD predictions of both sets of fluxes.

TABLE 3.3

Comparison of flux measurements of Weller, et. al., [82] with flux predictions of ATRAD. (ATRAD fluxes have been rounded to two significant figures since measurements are only quoted to this accuracy). The double-headed arrow indicates the two flux values whose agreement was forced by adjusting the ATRAD cloud droplet number density.

Pt. Barrow, Alaska			
Date (1971)	June 2	June 10	June 29
Albedo	79%	58%	20%
Solar elevation	31°	24°	21°
Measured surface down-flux*	0.56	0.38	0.26
ATRAD surface down flux*	0.60	0.38	↕ 0.26
Measured surface down-flux,* interpolated to 30° solar elevation	0.54	0.47	0.37
ATRAD surface down-flux,* 30° solar elevation	0.58	0.51	0.43

\*All fluxes in cal/cm<sup>2</sup>/min

Before discussing Table 3.3, let us specify the atmospheric structure used in ATRAD for the Arctic stratus problem. This structure, consisting of altitude, pressure, temperature, water vapor density, ozone density, and aerosol (cloud) number density, as taken from an actual ATRAD run, is shown in Table 3.4. The offset of levels 20 and 21 indicates that the cloud layer is between those two levels. The profiles have been taken from various sources, since no radiosonde data was given in Reference [82]. The temperature and humidity profiles were taken from the supplemental Standard Atmosphere for 75°N for July,<sup>[83]</sup> except that the relative humidity values within and below the cloud were increased to 100 percent. Humidity values above 10 km were obtained from the stratospheric polar model of Reference [83], which presumes an exponential decrease in mixing ratio by a factor of 10 between 10 km and 12 km, a constant mixing ratio between 12 km and 17 km, and an exponential increase in mixing ratio by a factor of 30 between 17 km and 30 km. The total water vapor amount is 1.65 g/cm<sup>2</sup> of which 0.33 g/cm<sup>2</sup> is between the ground and the cloud base and 0.30 g/cm<sup>2</sup> is within the cloud. The ozone profile used was from the sub-arctic summer atmosphere of McClatchey, et. al.,<sup>[31]</sup> resulting in a total vertical ozone amount of 0.33 atm-cm. The cloud is located between  $\frac{1}{2}$  km and 1 km, which is typical for Arctic summer stratus according to Huschke.<sup>[84]</sup> The cloud size distribution is taken from Weller, et. al., and was measured near Pt. Barrow in September 1971. We are assured that these measurements are typical for summer stratus, however, so there is no difficulty in applying them to our June situations. The size distribution is reproduced in Figure 3.8; the histogram data, which is more fundamental, was used in preference to the smooth fit.

The ATRAD calculation used 22 levels and 75 spectral intervals. The spectral interval structure was (in cm<sup>-1</sup>): 3600(240)4800(320)8000(500)32000(1000)35000(1500)48500. This

TABLE 3.4

Actual ATRAD atmospheric structure used in Arctic stratus problem. Altitude is in km, pressure in mb, temperature in °K, H<sub>2</sub>O vapor density in g/m<sup>3</sup>, O<sub>3</sub> density in atm-cm/km, and aerosol density in particles/cm<sup>3</sup>

I N P U T    D A T A									
I	ALT	73N	PRESS	TEMP	H2O DEN	O3 DEN	AER DEN		
1	5.0000+01	0.0000	1.0000+00	2.8000+02	0.0000	2.0000-04	0.0000		
2	3.0000+01	2.0000+01	1.1980+01	2.3005+02	1.4000-03	6.5000-03	0.0000		
3	2.5000+01	2.5000+01	2.4580+01	2.3309+02	8.0000-04	1.2000-02	0.0000		
4	2.3000+01	2.7000+01	3.2000+01	2.3071+02	6.5000-04	1.4000-02	0.0000		
5	2.1000+01	2.9000+01	4.4280+01	2.3015+02	5.1500-04	1.7000-02	0.0000		
6	1.9000+01	3.1000+01	5.9500+01	2.3015+02	4.1000-04	1.9000-02	0.0000		
7	1.7000+01	3.3000+01	7.9900+01	2.3015+02	3.3000-04	1.8000-02	0.0000		
8	1.5000+01	3.5000+01	1.0752+02	2.3015+02	2.4000-04	1.5000-02	0.0000		
9	1.3000+01	3.7000+01	1.6770+02	2.2965+02	6.0000-04	1.7000-02	0.0000		
10	1.0000+01	4.0000+01	2.5251+02	2.2666+02	1.1000-02	6.1000-03	0.0000		
11	9.0000+00	4.1000+01	3.0525+02	2.2935+02	2.5000-02	4.9000-03	0.0000		
12	8.0000+00	4.2000+01	3.5349+02	2.3585+02	5.8000-02	3.7000-03	0.0000		
13	7.0000+00	4.3000+01	4.0777+02	2.4275+02	1.4000-01	3.5000-03	0.0000		
14	6.0000+00	4.4000+01	4.5862+02	2.4885+02	3.4000-01	3.3000-03	0.0000		
15	5.0000+00	4.5000+01	5.3667+02	2.5535+02	6.4000-01	3.0000-03	0.0000		
16	4.0000+00	4.6000+01	6.1249+02	2.5186+02	1.1000+00	2.8000-03	0.0000		
17	3.0000+00	4.7000+01	6.9671+02	2.4837+02	2.0600+00	2.7000-03	0.0000		
18	2.0000+00	4.8000+01	7.9020+02	2.4294+02	3.1200+00	2.6000-03	0.0000		
19	1.5000+00	4.8500+01	8.4067+02	2.4244+02	4.2400+00	2.5500-03	0.0000		
20	1.0000+00	4.9000+01	8.9502+02	2.4255+02	5.7679+00	2.5000-03	2.8350+01		
21	5.0000-01	4.9500+01	9.5195+02	2.4285+02	6.2023+00	2.4000-03	0.0000		
22	5.0000-01	4.9500+01	9.5195+02	2.4285+02	6.2023+00	2.4000-03	0.0000		
23	0.0000	5.0000+01	1.0125+03	2.4285+02	6.8500+00	2.3000-03	0.0000		

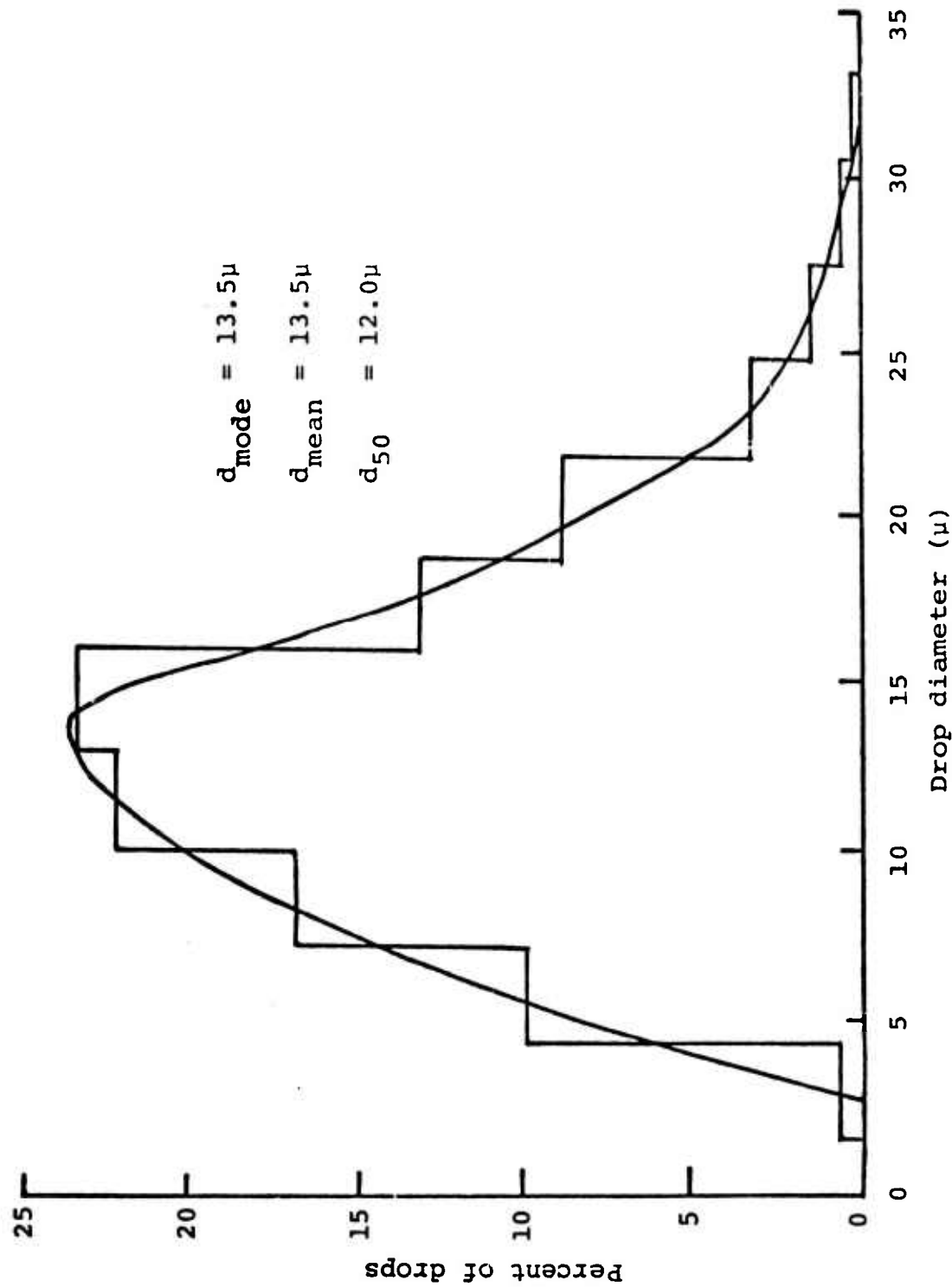


Figure 3.8 - Number distribution of Arctic stratus clouds at Barrow.

structure covers the instrumental response range of  $0.2 - 2.6\mu$ . Twelve Gaussian angles were used in each spectral interval.

Since the atmospheric structure chosen for ATRAD is, to say the least, somewhat eclectic, some comments need to be made about the sensitivity of the computed fluxes to the input data. The surface fluxes are almost totally insensitive to the cloud height and the ozone profile, within physically realistic limits. (The measurements of Weller, et., al., bear this out from the experimental side, as far as the insensitivity to stratus ceiling height goes). Sensitivity to the size distribution has not been investigated; however, based on the success of calculations which go so far as to approximate Mie scattering by isotropic scattering, and on the success of simple models such as we shall discuss shortly, one gains the impression that it is only a few gross cloud parameters (droplet density, mean droplet radius, etc.) which are really important. It might even reasonably be hypothesized that any size distribution which leads to the same set of gross cloud properties will also lead to the same flux predictions. (ATRAD will be used in the future to try and formulate this hypothesis more rigorously). Since we are dealing only with the solar spectrum  $0.3 - 2.6\mu$  (the instrumental response range), the temperature profile only enters the calculation through the effective absorber amount of water vapor and through the Rayleigh scattering coefficient, and in both cases the derived quantities are insensitive to realistic temperature variations.

The input data to which the calculation is sensitive are the albedo, solar elevation, moisture profile, droplet density, and cloud thickness. The albedo and solar elevation are known (see Table 3.3). The moisture profile, while not known, cannot differ too greatly from the standard one that we use, for Arctic summer conditions are considerably less

variable than mid-latitude and tropical regimes, where cumulus convection and frontal systems are important. And, furthermore, the absorption of solar radiation by water vapor is decidedly a secondary effect in this problem compared to the reflection of solar radiation at the cloud top and bottom and at the surface. As for the droplet density and cloud thickness, it is really just their product, which is proportional to the optical thickness of the cloud, that is important. The cloud thickness was fixed at  $\frac{1}{2}$  km; then we varied the (unknown) droplet density until we obtained exact agreement between the ATRAD surface down-flux prediction and the measurement in Table 3.3 for June 29. The droplet density necessary was  $28.35 \text{ cm}^{-3}$ . Based on the observation in Ref. [82], that the cloud was similar on the three days, the same droplet density was used for the other two days.

The ATRAD flux prediction for June 10 agrees exactly with the measurement to the two significant figures given in the measurement. For June 2, the ATRAD flux prediction differs from the measurement by 7%. Considering the difficulty of the problem, this sort of agreement is remarkable and constitutes an excellent experimental verification of ATRAD.

The source of the 7 percent disagreement on June 2 could be any combination of several factors. One factor of course is errors in ATRAD itself. However, the disagreement could also be eliminated by: (a) changing the solar elevation from  $31^\circ$  to  $29^\circ$ , (b) decreasing the albedo from 79 percent to 65 percent, or (c) increasing the droplet density from  $28.35 \text{ cm}^{-3}$  to  $43.5 \text{ cm}^{-3}$ . It seems highly unlikely that the albedo measurement could have been in error by anything like the 14 percent necessary to completely account for the discrepancy; neither does it seem very likely that the droplet concentration was some 53 percent higher on June 2 than on the other two days. Therefore, if we are to ascribe the disagreement to measurement errors (other than errors in the

pyranometer itself), it is clear that (a) is the most likely candidate. The computed surface fluxes are particularly sensitive to the solar elevation (and surprisingly insensitive to the albedo and the droplet concentration). The measured values of solar elevation in Reference [82] are referred to as 'mean solar angles', implying that the solar elevation varied during the course of the measurement and that subsequently some sort of average was taken. If the weighting function used in this average was improper and the correct average was, say,  $30^\circ$ , already half of the discrepancy would have been accounted for. The rest of the discrepancy could then more easily be accounted for, perhaps by a combination of a too-high measured albedo and a higher cloud optical thickness on June 2 than on June 10 and June 29 (note that the droplet concentration could have been nearly the same, but with a geometrically thicker cloud on June 2).

The ATRAD sensitivity studies of the last paragraph have an important bearing on any radiation measurements which are conducted under Arctic summer stratus. They indicate that great accuracy is not required in either the albedo or the cloud droplet concentration when one wishes to predict the downward radiation flux at the surface. In the above examples, an 18 percent decrease in the albedo or, alternatively, a 53 percent increase in the cloud droplet concentration, were necessary in order to produce a mere 7 percent drop in the down-flux. On the other hand, accurate knowledge of the solar elevation  $\theta_s$  is very important. This is because the down-flux above the cloud varies closely as  $\sin \theta_s$ , while, according to ATRAD computations, the down-flux at the surface has the even stronger dependence  $(\sin \theta_s)^{3/2}$ . The enhanced  $\theta_s$ -dependence of the surface flux is due partly to the diffusion of the radiation within the cloud and partly to the strong



dependence of cloud-top albedo on  $\theta_s$ . At any rate, because of this sensitivity to  $\theta_s$ , care must be exercised in the taking and processing of experimental data involving even small ( $1^\circ - 2^\circ$ ) variations in sun angle.

### 3.3.2 Dependence of Surface Flux on Solar Elevation

The last two lines of Table 3.3 indicate the pitfalls of extrapolating data taken at one sun angle to other sun angles. The first of these lines contains the original measurements 'interpolated to  $30^\circ$  solar elevation', [82] and the second contains the ATRAD predictions for  $\theta_s = 30^\circ$ , all other parameters remaining the same. While we cannot be absolutely certain, it appears that the 'interpolated' values were actually extrapolated according to an assumed  $\sin \theta_s$  dependence, as witness the following comparisons:

$$\frac{0.56}{0.54} = 1.04$$

$$\frac{\sin 31^\circ}{\sin 30^\circ} = 1.03$$

$$\frac{0.38}{0.47} = 0.81$$

$$\frac{\sin 24^\circ}{\sin 30^\circ} = 0.81$$

$$\frac{0.26}{0.37} = 0.70$$

$$\frac{\sin 21^\circ}{\sin 30^\circ} = 0.72$$

The left-hand ratios are of measured to 'interpolated' fluxes, and the right-hand ratios are of the sines of the corresponding measured  $\theta_s$ 's to the sine of  $30^\circ$ . It is obvious from Table 3.3 that ATRAD does not predict a  $\sin \theta_s$  variation of surface down-flux, nor should such a variation really be expected except for a clear sky. Therefore, an extensive series of ATRAD calculations were made for varying albedo and sun angle in order to investigate the actual functional form of the extrapolation to other sun angles.

The results of this parameter study are shown in Table 3.5. Both the full down-flux  $F_g^\downarrow$  and the purely scattered part  $^sF_g^\downarrow$  at the ground are included. The droplet concentration is  $28.35 \text{ cm}^{-3}$ . Suppose that  $F_g$  varies as some power  $\alpha$  of  $\sin \theta_s$ ,

TABLE 3.5

ATRAD predicted down-fluxes at the ground ( $F_g^\downarrow$ ) for the full instrumental range  $3600 - 48500 \text{ cm}^{-1}$  and for<sup>g</sup>the purely-scattering spectral range  $11000 - 48500 \text{ cm}^{-1}$ , as a function of albedo and solar elevation ( $\theta_s$ )

albedo	$\theta_s$	$F_g^\downarrow$ $3600 - 48500 \text{ cm}^{-1}$ (watts/m <sup>2</sup> )	$^sF_g^\downarrow$ $11000 - 48500 \text{ cm}^{-1}$ (watts/m <sup>2</sup> )
0	40°	410.5	299.6
	30°	277.3	203.3
	20°	156.6	115.5
0.20	40°	443.1	324.1
	30°	299.4	220.0
	20°	169.9	125.5
0.58	40°	529.3	389.5
	30°	357.8	264.3
	20°	202.6	150.5
0.79	40°	593.6	438.6
	30°	401.3	297.7
	20°	226.9	169.1

$$F_g^\downarrow = F_o (\sin \theta_s)^\alpha \quad (3.1)$$

Then for fixed albedo, each pair of values of  $F_g^\downarrow$  can be used to eliminate  $F_o$  and solve for  $\alpha$ . It is found that  $\alpha$  varies in the narrow range 1.50 - 1.58, with a tendency to decrease slightly from  $\sim 1.56$  for  $\theta_s \in (30^\circ, 40^\circ)$  to  $\sim 1.51$  for  $\theta_s \in (20^\circ, 30^\circ)$ . The best over-all value of  $\alpha$  for  $\theta_s \in (20^\circ, 40^\circ)$  is 1.53.  $\alpha$  is furthermore entirely independent of albedo. Thus the entire albedo variation resides in  $F_o$ ; however, we do not have sufficient data to empirically fit this variation. Neither do we know the dependence of either  $F_o$  or  $\alpha$  on cloud droplet concentration. Both of these dependencies shall be investigated in the future.

If a relation similar to Equation (3.1) is postulated for just the purely scattered component  $^sF_g^\downarrow$  of Table 3.5 exactly similar results are obtained. The exponent  $\alpha$  varies between 1.49 and 1.56, with a best over-all value of 1.51. It decreases slightly from 1.54 in the  $30^\circ - 40^\circ$  range of  $\theta_s$  to 1.49 in the  $20^\circ - 30^\circ$  range. And it is independent of albedo. The fact that the exponent is almost the same as for the full solar spectrum is surprising, and must indicate that the scattering is the relatively dominant influence upon the  $\theta_s$ -variation, with absorption playing only a minor role.

### 3.3.3 Comparisons of ATRAD with Simpler Models

Weller, et. al., propose a multiple cloud-ground reflection model with which to predict their experimental results. This model is practically identical to that used for cloudy cases in the Mintz-Arakawa GCM, <sup>[80]</sup> and for that reason the discussion below takes on added interest.

The model of Weller, et. al., is illustrated in Figure 3.9. The cloud albedo, as seen

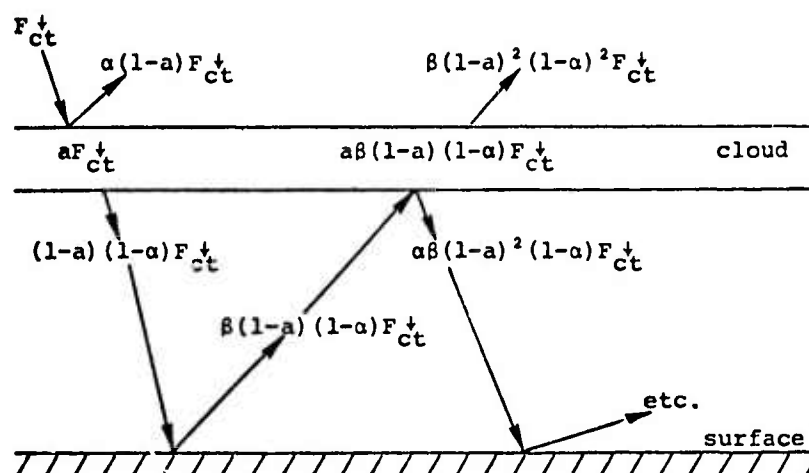


Figure 3.9 - Multiple cloud-ground reflection model of Weller, et. al. [82]  $F_{ct}^\downarrow$  is the down-flux at the cloud top,  $a$  and  $\alpha$  are related to the cloud absorption and albedo, respectively, and  $\beta$  is the surface albedo.

from either the top or the bottom, is equal to  $\alpha(1-a)$ . The cloud absorbs a fraction  $a$  of the down-flux  $F_{ct}^\downarrow$  incident on the cloud top.  $\beta$  is the surface albedo. No absorption between the cloud and the surface is assumed and therefore the down-flux  $F_g^\downarrow$  at the surface resulting from the multiple reflection is:

$$\begin{aligned}
 F_g^\downarrow &= F_{ct}^\downarrow (1-a)(1-\alpha) \sum_{n=0}^{\infty} [\alpha\beta(1-a)]^n \\
 &= F_{ct}^\downarrow \frac{(1-a)(1-\alpha)}{1 - \alpha\beta(1-a)} \quad (3.2)
 \end{aligned}$$

Unfortunately, Reference [82] attempts to fit this model to the fluxes which were incorrectly extrapolated to  $30^\circ$ , arriving thereby at parameter values  $\alpha = 0.55$  and  $a = 0.07$ . For completeness, however, the predictions with these parameter values are included in Table 3.6.

In order to ascertain the predictive capabilities of Equation (3.2) as a function of  $\beta$ , for fixed sun angle, the parameters  $a$  and  $\alpha$  were chosen to give the ATRAD values of cloud top albedo and cloud absorption when  $\beta = 0$ ,  $\theta_s = 30^\circ$ . Referring to Figure 3.9, it may be seen that:

$$\alpha(1-a) = \frac{F_{ct}^{\uparrow}(\beta = 0)}{F_{ct}^{\downarrow}(\beta = 0)} \quad (3.3)$$

$$(1-\alpha)(1-a) = \frac{F_g^{\downarrow}(\beta = 0)}{F_{ct}^{\downarrow}(\beta = 0)} \quad (3.4)$$

The ratios on the right-hand sides were taken from an ATRAD calculation with  $\beta = 0$ ,  $\theta_s = 30^\circ$ , yielding for  $a$  and  $\alpha$ ,

$$\alpha = 0.4541 ,$$

and

$$a = 0.0274 .$$

Using these values of  $a$  and  $\alpha$ , the predictions of Equation (3.2) and the predictions of ATRAD for the ratio  $F_g^{\downarrow}/F_{ct}^{\downarrow}$  are compared in Table 3.6 for various values of  $\beta$ . (The other columns in Table 3.6 shall be discussed later).

The parameters  $\alpha = 0.55$ ,  $a = 0.07$ , clearly lead to poor predictions vis á vis ATRAD. The parameters  $\alpha = 0.4541$ ,  $a = 0.0274$  of course lead to agreement with ATRAD for  $\beta = 0$ , since this has been rigged, but as  $\beta$  increases, the predictions of Equation (3.2) increasingly exceed those of ATRAD. Some physical effect is apparently being ignored in the simple model, Equation (3.2).

TABLE 3.6

Ratio of the down-flux at the ground to the down-flux at the Arctic stratus cloud top, as predicted by various models for solar elevation,  $30^\circ$ , for several values of surface albedo,  $\beta$

$\beta$	$F_g^\downarrow / F_{ct}^\downarrow$				
	Eq. (3.2) $\alpha=0.4541,$ $a=0.0274$	Eq. (3.2) $\alpha=0.55,$ $a=0.07$	ATRAD	Eq. (3.12) parameters from Eq. (3.10)	Eq. (3.17) parameters from Eq. (3.21)
0	0.5310	0.4185	0.5310	0.5310	0.5310
0.20	0.5824	0.4662	0.5731	0.5817	0.5731
0.58	0.7138	0.5950	0.6748	0.7106	0.6749
0.79	0.8155	0.7023	0.7484	0.8098	0.7484

There are two physical effects which an examination of the ATRAD fluxes show to be marginally important. One is the absorption of solar radiation within the cloud-to-ground (c $\rightarrow$ g) layer (by the near IR bands of water vapor) and the other is the Rayleigh back-scattering from the c $\rightarrow$ g layer. Therefore, a more complex multiple reflection model accounting for c $\rightarrow$ g absorption and back-scatter has been derived. (Note that the  $a$  and  $\alpha$  derived from Equations (3.3) and (3.4) contain these effects in some crude fashion, since the ATRAD fluxes do; however, until the effects are made explicit, the extent to which they are accounted for can only be conjectured). In the process, the notation of Figure 3.9 has been rejected in favor of the following:

$\alpha_c$  = cloud albedo,

$a_c$  = cloud fractional absorption,

$\alpha_R$  = albedo of c $\rightarrow$ g layer,

and

$a_w$  = fractional absorption in c $\rightarrow$ g layer.

These quantities are related to those of Figure 3.9 by:

$$\alpha_c = \alpha(1-a),$$

and

$$a_c = \frac{a}{1-\alpha_c}.$$

We also define:

$$\begin{aligned} T_c &= \text{transmission of cloud} \\ &= (1-\alpha_c)(1-a_c), \end{aligned}$$

and

$$\begin{aligned} T_a &= \text{transmission of c} \rightarrow \text{g layer} \\ &= (1-\alpha_R)(1-a_w). \end{aligned}$$

Consider now the case  $\beta = 0$ , illustrated in Figure 3.10. The upward-directed fluxes at the cloud bottom are then entirely ascribable to Rayleigh back-scattering, since the surface contributes nothing. If we sum the infinite geometric series implied by the "etc." in Figure 3.10, we arrive at the equations:

$$\gamma_1 \equiv \frac{F_g^{\uparrow}(\beta=0)}{F_{ct}^{\uparrow}(\beta=0)} = \Gamma_c T_a T_c, \quad (3.5)$$

$$\gamma_2 \equiv \frac{F_{ct}^{\uparrow}(\beta=0)}{F_{ct}^{\uparrow}(\beta=0)} = \alpha_c + \Gamma_c \alpha_R T_c^2, \quad (3.6)$$

$$\gamma_3 \equiv \frac{F_{cb}^{\uparrow}(\beta=0)}{F_{ct}^{\uparrow}(\beta=0)} = \Gamma_c T_c, \quad (3.7)$$

and

$$\gamma_4 \equiv \frac{F_{cb}^{\uparrow}(\beta=0)}{F_{ct}^{\uparrow}(\beta=0)} = \Gamma_c \alpha_R T_c \quad (3.8)$$

where

$$\Gamma_c \equiv \frac{1}{1 - \alpha_R \alpha_c} \quad (3.9)$$

and "cb" refers to the cloud base.

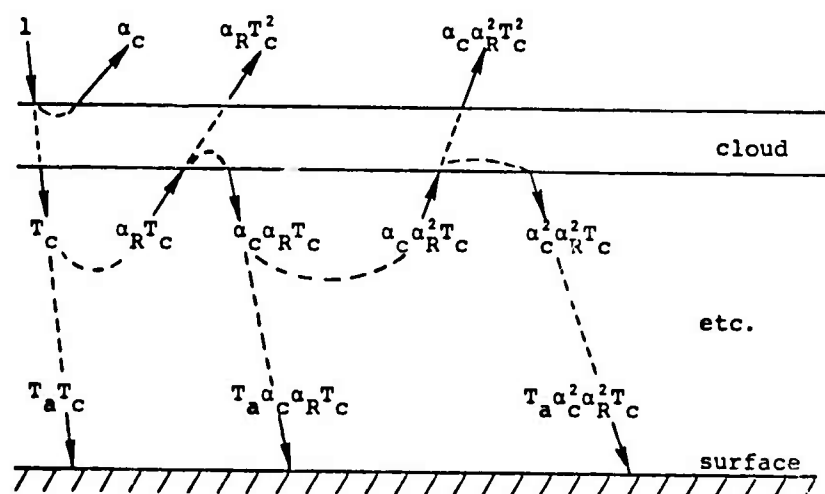


Figure 3.10 - Multiple cloud-ground reflection model including the effects of absorption and back-scattering from the cloud-to-ground layer for the case of zero surface albedo,  $\beta = 0$ . The incident flux at the cloud top is taken to be unity.

If the ratios  $\gamma_1, \gamma_2, \gamma_3, \gamma_4$  are regarded as known from an ATRAD calculation with  $\beta = 0$ , then Equations (3.5) to (3.8) uniquely determine the four parameters  $\alpha_c, a_c, \alpha_R$ , and  $a_w$ . For the  $\theta_s = 30^\circ, \beta = 0$  ATRAD calculation of the Arctic stratus problem, the parameters are found to be:



$$\alpha_R = \frac{\gamma_4}{\gamma_3} = 0.005687 ,$$

$$a_w = 1 - \frac{\gamma_1/\gamma_3}{1 - \alpha_R} = 0.006850 ,$$

(3.10)

$$\alpha_c = \frac{\gamma_2 - (\gamma_4^2/\alpha_R)}{1 - \gamma_4^2} = 0.43998 ,$$

and

$$a_c = 1 - \left( \frac{1 - \alpha_c \alpha_R}{1 - \alpha_c} \right) \gamma_3 = 0.04229 .$$

Both the Rayleigh back-scatter  $\alpha_R$  and the absorption  $a_w$  are small; they could only be important when the surface albedo is high and the radiation bounces between cloud and ground many times.

Now we extend the model to  $\beta > 0$ . In order to avoid confusion, all the multiple reflections between the cloud and the c→g layer are summed up by use of the factor  $\Gamma_c$  of Equation (3.9). All the multiple reflections between the ground and the c→g layer are summed up by use of the factor

$$\Gamma_g = \frac{1}{1 - \alpha_R \beta} \quad (3.11)$$

With these simplifications, the model is presented in Figure 3.11. The algorithm used in its construction is as follows:

- (a) a down-flux at the cloud base coming from the cloud top is enhanced by the factor  $\Gamma_c$ , then a fraction  $\alpha_R$  of this is reflected upward and proceeds without further reflection (but attenuated by the factor  $T_c$ ) to the cloud top;

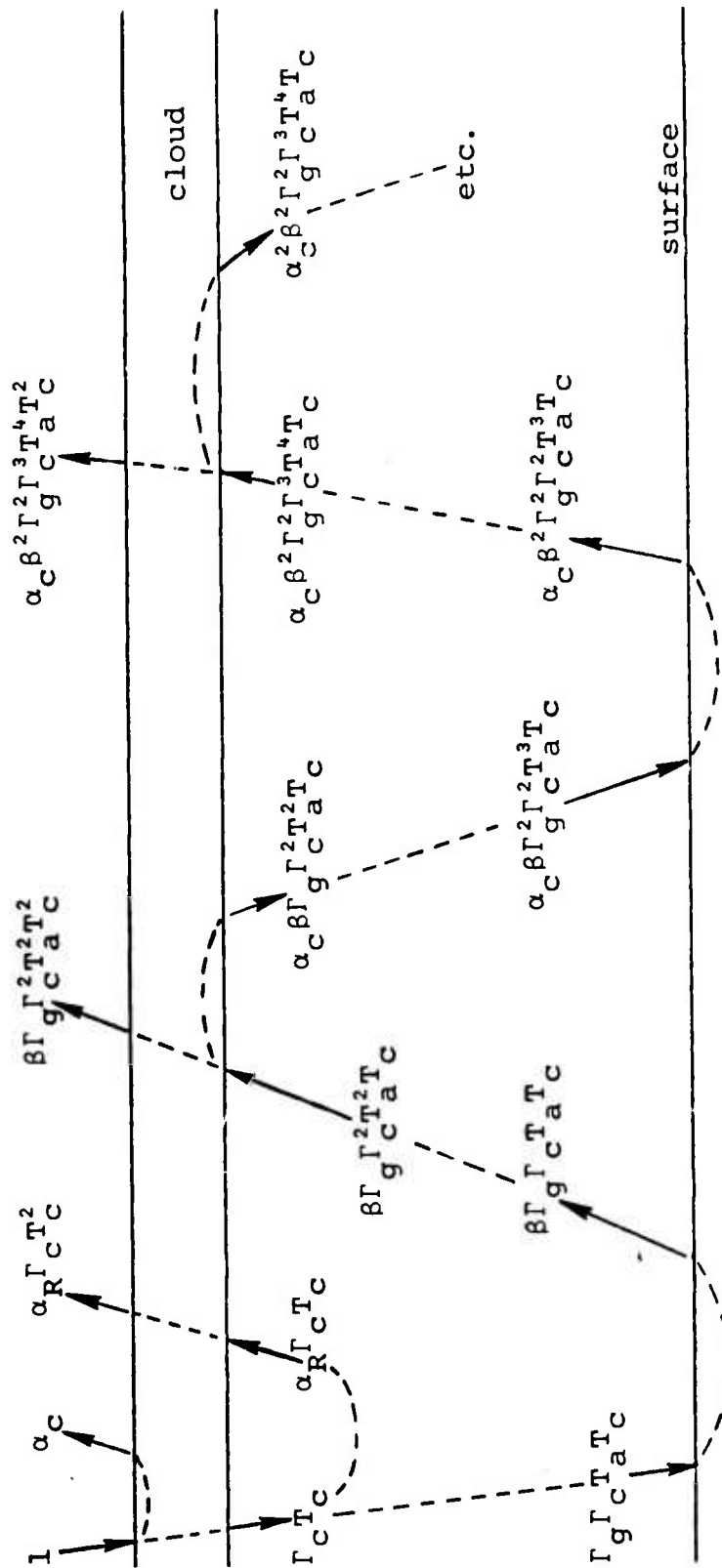


Figure 3.11 - Multiple reflection model which includes the effects of absorption and back-scattering in the cloud-to-ground layer, for arbitrary surface albedo,  $\beta$ .

- (b) a down-flux at the ground is enhanced by the factor  $\Gamma_g$ , then a fraction  $\beta$  of this is reflected upward and proceeds without further reflection (but attenuated by the factor  $T_a$ ) to the cloud base;
- (c) an up-flux at the cloud base coming from the ground is enhanced by the factor  $\Gamma_c$ , then a fraction  $\alpha_c$  of this is reflected downward and proceeds without further reflection (but attenuated by the factor  $T_a$ ) to the ground.

Note that part (a) of the algorithm is only exercised once, since we are neglecting Rayleigh back-scattering of the up-fluxes at the cloud top. This neglect is justifiable because, first, the effect is small, and second, the error is partially compensated by looking only at the ratios of fluxes to the down-flux at the cloud top ( $F_{ct}^\downarrow$ ).

Summing the infinite geometric series implied in Figure 3.11, we arrive at the model:

$$\frac{F_g^\downarrow}{F_{ct}^\downarrow} = \frac{\Gamma_g \Gamma_c T_a T_c}{1 - \alpha_c \beta \Gamma_g \Gamma_c T_a^2} \quad , \quad (3.12)$$

$$\frac{F_{ct}^\uparrow}{F_{ct}^\downarrow} = \alpha_c + \alpha_R \Gamma_c T_c^2 + \frac{\beta \Gamma_g \Gamma_c^2 T_a^2 T_c^2}{1 - \alpha_c \beta \Gamma_g \Gamma_c T_a^2} \quad , \quad (3.13)$$

$$\frac{F_{cb}^\downarrow}{F_{ct}^\downarrow} = \frac{\Gamma_c T_c}{1 - \alpha_c \beta \Gamma_g \Gamma_c T_a^2} \quad , \quad (3.14)$$

and

$$\frac{F_{cb}^\uparrow}{F_{ct}^\downarrow} = \alpha_R \Gamma_c T_c + \frac{\beta \Gamma_g \Gamma_c^2 T_a^2 T_c}{1 - \alpha_c \beta \Gamma_g \Gamma_c T_a^2} \quad (3.15)$$

That Equations (3.12) to (3.15) reduce properly in various limiting cases may be verified. Obviously for  $\beta = 0$ , they reduce to Equations (3.5) to (3.8). For  $\alpha_R = 0$ , Equation (3.12) reduces to:

$$\frac{F_g^+}{F_{ct}^+} = \frac{(1-a_w)(1-\alpha_c)(1-a_c)}{1 - (1-a_w)^2 \alpha_c \beta} .$$

which is similar to the simple model, Equation (3.2), except that the transmission of the c+g layer is  $(1-a_w)$  rather than unity.

Using Eq. (3.12) with parameter values from Eq. (3.10) leads to the column which is so labeled in Table 3.6. The flux ratios predicted by Eq. (3.12) are slightly lower for  $\beta > 0$  than those predicted by the simpler model of Eq. (3.2), and the adjustments are in the right direction to bring the ratios into agreement with ATRAD. However, the adjustments are much too small. Hence we must look further for the physical effect which has been ignored.

A fact which is often overlooked vis á vis the parameter which we call 'albedo' is that this quantity is not an intrinsic property, but depends on the angular distribution of the incident radiation. This is true whether we are speaking of surfaces or of clouds, but for clouds the angular dependence is particularly strong. For example, for the Arctic stratus cloud, ATRAD predicts a cloud-top albedo of ~52 percent when  $\theta_s = 20^\circ$  and of ~44 percent when  $\theta_s = 30^\circ$ . Hence it is unreasonable to expect the top and bottom of a cloud to have the same albedo, for they experience quite different fields of radiant intensity. The intensity at the cloud top is primarily collimated, while that at the cloud bottom is thoroughly diffuse. In order to account for this effect, we

shall define:

$\alpha_d$  = diffuse albedo of cloud

and use  $\alpha_d$  for the albedo of the cloud bottom. Defining the new symbols:

$t_c$  = transmission of cloud from bottom to top

$$= (1 - \alpha_d)(1 - \alpha_c)$$

$$\Gamma_d = \frac{1}{1 - \alpha_R \alpha_d} \quad , \quad (3.16)$$

the revised model becomes:

$$\frac{F_{gt}^\downarrow}{F_{ct}^\downarrow} = \frac{\Gamma_g \Gamma_d T_a T_c}{1 - \alpha_d \beta \Gamma_g \Gamma_d T_a^2} \quad , \quad (3.17)$$

$$\frac{F_{ct}^\uparrow}{F_{ct}^\downarrow} = \alpha_c + \alpha_R \Gamma_d T_c t_c + \frac{\beta \Gamma_g \Gamma_d^2 T_a^2 T_c t_c}{1 - \alpha_d \beta \Gamma_g \Gamma_d T_a^2} \quad , \quad (3.18)$$

$$\frac{F_{cb}^\downarrow}{F_{ct}^\downarrow} = \frac{\Gamma_d T_c}{1 - \alpha_d \beta \Gamma_g \Gamma_d T_a^2} \quad , \quad (3.19)$$

$$\frac{F_{cb}^\uparrow}{F_{ct}^\downarrow} = \alpha_R \Gamma_d T_c + \frac{\beta \Gamma_g \Gamma_d^2 T_a^2 T_c}{1 - \alpha_d \beta \Gamma_g \Gamma_d T_a^2} \quad . \quad (3.20)$$

With the addition of  $\alpha_d$ , Equations (3.17) to (3.20) are now a five-parameter model. Therefore the four values of the above ratios at  $\beta = 0$  ( $\gamma_1, \gamma_2, \gamma_3, \gamma_4$ ; see Equations (3.5) to (3.8)) are insufficient to determine all five parameters.

One finds, however, that  $\alpha_R$  and  $a_w$  are given by the same expressions as in Equation (3.10) and therefore they have the same numerical values as given there (for  $\theta_s = 30^\circ$ ). This is as it should be since the model alteration concerns the cloud and not the air beneath it. To solve for  $\alpha_c$ ,  $\alpha_d$ , and  $a_c$ , we shall take, as an additional datum, the value of  $F_g^\downarrow/F_{ct}^\downarrow$  from an ATRAD calculation for  $\theta_s = 30^\circ$ ,  $\beta = 0.20$ ,

$$\gamma_5 = \frac{F_g^\downarrow(\beta=0.20)}{F_{ct}^\downarrow(\beta=0.20)} .$$

It is then possible to deduce that:

$$\alpha_R = 0.005687 ,$$

$$a_w = 0.006850 ,$$

$$\alpha_d = 0.3706 ,$$

(3.21)

$$\alpha_c = 0.4398 ,$$

and

$$a_c = 0.04226 .$$

Using this parameter set in Equation (3.17), the last column of Table 3.7 is generated. The agreement with ATRAD is exact for the two albedos 0.58 and 0.79 for which the result is not rigged. Thus, the model seems very promising.

In order to test the model further, ATRAD calculations were made at solar elevations  $\theta_s$  of  $20^\circ$  and  $40^\circ$ . Clearly, we expect  $\alpha_c$  to vary with  $\theta_s$ . If the model is correct, however, we should expect  $\alpha_d$  to remain practically unchanged. Therefore, we hold  $\alpha_d$  fixed at 0.3706 and recalculate only the other four parameters, forcing them to agree with the  $\beta = 0$  ATRAD calculation as before. For  $\theta_s = 20^\circ$ , the parameters are:

TABLE 3.7

Comparisons of ATRAD and Eq. (3.17) predictions of flux ratio  $F_g^\downarrow/F_{ct}^\downarrow$  (down-flux at the surface to down-flux at the cloud top) for solar elevations  $20^\circ$  and  $40^\circ$ , for various albedos.

Albedo	$F_g^\downarrow/F_{ct}^\downarrow$			
	$\theta_s = 20^\circ$		$\theta_s = 40^\circ$	
	Equation (3.17) and Equation (3.22)	ATRAD	Equation (3.17) and Equation (3.23)	ATRAD
0	0.4578	0.4578	0.5984	0.5984
0.20	0.4942	0.4945	0.6459	0.6454
0.58	0.5824	0.5835	0.7603	0.7586
0.79	0.6460	0.6482	0.8429	0.8402

$$\alpha_c = 0.5165$$

$$a_c = 0.04443$$

$$\alpha_R = 0.005705$$

$$a_w = 0.005562$$

(3.22)

and for  $\theta_s = 40^\circ$  they are:

$$\alpha_c = 0.3702$$

$$a_c = 0.03888$$

$$\alpha_R = 0.005587$$

$$a_w = 0.007819$$

(3.23)

Using these parameter sets, the multiple-reflection model (Eq. 3.17) predictions of the ratio of surface down-flux to cloud-top down-flux are compared with the corresponding ATRAD predictions in Table 3.6. The agreement is excellent. The differences are considerably less than 1%. Thus, the multiple-reflection model (Eq. 3.17) incorporates all the major physical effects and can be relied upon to extrapolate the surface flux to any albedo, if its parameters are adjusted to predict the correct fluxes for  $\beta = 0$ .

It is of interest to study the variations of the parameters  $\alpha_c$ ,  $a_c$ ,  $\alpha_R$ ,  $a_w$  with solar elevation, since ultimately it is desirable to parameterize these variations and free the multiple-reflection model entirely from its dependence on ATRAD. Insufficient calculational data prevents our making any definitive conclusions as yet, however, the following trends are evident for typical Arctic solar elevations:

- (a)  $\alpha_R$  is practically independent of  $\theta_s$ ;
- (b)  $a_w$  increases slowly with  $\theta_s$ , approximately as  $(\sin\theta_s)^{0.54}$ ;
- (c)  $\alpha_c$  decreases markedly as  $\theta_s$  increases, and its variation is not even close to a power of  $\sin\theta_s$  or  $\cos\theta_s$ ;
- (d)  $a_c$  decreases slowly as  $\theta_s$  increases, very approximately as  $(\cos\theta_s)^{0.65}$ .

The behavior (c) of the cloud-top albedo is very similar to the behavior of the albedo of natural surfaces, including snow, ice, and water. Therefore, empirical formulas which have been found useful for fitting the albedo of natural surfaces should be applicable to  $\alpha_c$  also. The behavior of  $a_w$ , which should be strictly constant if the under-cloud radiation



field is strictly diffuse, indicates that some deviation from diffuseness exists under the cloud. And, finally, the decrease of cloud absorption as the sun rises higher is understandable in terms of the relatively shorter average path traversed by a photon impinging on the cloud top at a large angle.

#### 3.4 ATRAD COMPARED WITH KATAYAMA MODELS FOR CLEAR-SKY CASES

In Section 3.2 we presented comparisons between the predictions of ATRAD and those of the older Katayama radiation model as used in the 2-level Mintz-Arakawa GCM at RAND. Two clear-sky problems, a wet one and a dry one, were discussed. Further analysis has subsequently been performed on those problems, and, in addition, comparisons have been made with the newer Katayama radiation model used in the 3-level Mintz-Arakawa GCM at UCLA. The latter model has been found to give dramatically better results in the IR as compared to the older version. Problems remain, however, in the parameterization of near IR solar absorption, and in the choice of a pressure scaling factor.

The atmospheric structures for the two clear sky problems are shown in tabular form in Tables 3.8a and 3.8b, which were taken from actual ATRAD runs. (It would facilitate inter-comparison of models if all authors would present their model's atmospheric profiles in tabular as well as graphical form.) The temperature and humidity profiles from actual M/A (Mintz-Arakawa) 2-level grid locations in Chad (North Africa) and Bolivia were interpolated to the 39 ATRAD levels according to formulas given by Gates, et. al.,<sup>[80]</sup> as discussed at some length in Section 3.2. The Chad and Bolivia problems are opposite extremes in terms of water vapor content; the total vertical water vapor amount for Chad is  $0.204 \text{ g/cm}^2$ , while for Bolivia it is  $2.530 \text{ g/cm}^2$ , or 12.4 times as much. The ozone profile is the same for both problems.

TABLE 3.8a

Atmospheric profiles of altitude (km), pressure (mb), temperature ( $^{\circ}$ K), water vapor ( $\text{g/m}^3$ ), ozone density ( $\text{atm-cm/km}$ ), and aerosol density ( $= 0$ ) for Chad problem.

INPUT DATA							
I	ALT	ZDN	PRESS	TEMP	H2ODEN	O3DEN	AER DEN
1	4.4373+01	0.0000	2.0000+00	2.6011+02	2.7642-04	4.3524-04	0.0000
2	2.6584+01	1.7789+01	2.1800+01	2.4276+02	2.9618-04	1.0590-02	0.0000
3	2.2051+01	2.2323+01	4.1600+01	2.3629+02	3.0429-04	1.1899-02	0.0000
4	1.9383+01	2.4990+01	6.1400+01	2.3198+02	3.0994-04	1.0124-02	0.0000
5	1.7499+01	2.6874+01	8.1200+01	2.2868+02	3.1441-04	8.2558-03	0.0000
6	1.6048+01	2.8325+01	1.0100+02	2.2599+02	3.1815-04	6.7687-03	0.0000
7	1.4870+01	2.9503+01	1.2080+02	2.2371+02	3.3427-04	5.6377-03	0.0000
8	1.3881+01	3.0492+01	1.4060+02	2.2171+02	6.2082-04	4.7755-03	0.0000
9	1.3030+01	3.1343+01	1.6040+02	2.1994+02	1.0628-03	4.1081-03	0.0000
10	1.2284+01	3.2089+01	1.8020+02	2.1834+02	1.7093-03	3.5820-03	0.0000
11	1.1628+01	3.2745+01	2.0000+02	2.1169+02	2.6807-03	3.1649-03	0.0000
12	1.0731+01	3.3642+01	2.3060+02	2.1944+02	4.5834-03	2.6599-03	0.0000
13	9.9187+00	3.4455+01	2.6121+02	2.2642+02	7.3306-03	2.2639-03	0.0000
14	9.1748+00	3.5198+01	2.9181+02	2.3278+02	1.1131-02	1.9481-03	0.0000
15	8.4874+00	3.5886+01	3.2242+02	2.3862+02	1.6213-02	1.6922-03	0.0000
16	7.8474+00	3.6526+01	3.5302+02	2.4404+02	2.2826-02	1.4820-03	0.0000
17	7.2479+00	3.7125+01	3.8362+02	2.4909+02	3.1237-02	1.3075-03	0.0000
18	6.6834+00	3.7690+01	4.1423+02	2.5382+02	4.1733-02	1.1609-03	0.0000
19	6.1496+00	3.8224+01	4.4483+02	2.5828+02	5.4620-02	1.0367-03	0.0000
20	5.6429+00	3.8730+01	4.7543+02	2.6250+02	7.0222-02	9.3067-04	0.0000
21	5.1603+00	3.9213+01	5.0604+02	2.6650+02	8.8881-02	8.3937-04	0.0000
22	4.6993+00	3.9674+01	5.3664+02	2.7031+02	1.1096-01	7.6025-04	0.0000
23	4.2577+00	4.0115+01	5.6725+02	2.7394+02	1.3683-01	6.9127-04	0.0000
24	3.9385+00	4.0435+01	5.9020+02	2.7656+02	1.5896-01	6.4520-04	0.0000
25	3.6285+00	4.0745+01	6.1315+02	2.7910+02	1.8362-01	6.0332-04	0.0000
26	3.3272+00	4.1046+01	6.3610+02	2.8156+02	2.1100-01	5.6517-04	0.0000
27	3.0340+00	4.1339+01	6.5906+02	2.8395+02	2.4126-01	5.3031-04	0.0000
28	2.7485+00	4.1625+01	6.8201+02	2.8627+02	2.7461-01	4.9839-04	0.0000
29	2.4703+00	4.1903+01	7.0496+02	2.8853+02	3.1124-01	4.6909-04	0.0000
30	2.1988+00	4.2174+01	7.2791+02	2.9072+02	3.5135-01	4.4214-04	0.0000
31	1.9339+00	4.2439+01	7.5087+02	2.9286+02	3.9514-01	4.1730-04	0.0000
32	1.6748+00	4.2698+01	7.7382+02	2.9537+02	4.4216-01	3.9434-04	0.0000
33	1.4212+00	4.2952+01	7.9677+02	2.9767+02	4.9315-01	3.7306-04	0.0000
34	1.1728+00	4.3201+01	8.1973+02	3.0030+02	5.4831-01	3.5332-04	0.0000
35	9.2925-01	4.3444+01	8.4268+02	3.0268+02	6.0786-01	3.3497-04	0.0000
36	6.9041-01	4.3683+01	8.6563+02	3.0502+02	6.7202-01	3.1788-04	0.0000
37	4.5605-01	4.3917+01	8.8858+02	3.0731+02	7.4100-01	3.0195-04	0.0000
38	2.2598-01	4.4147+01	9.1154+02	3.0956+02	8.1503-01	2.8708-04	0.0000
39	0.0000	4.4373+01	9.3449+02	3.1177+02	8.9433-01	2.7318-04	0.0000

TABLE 3.8 b

Atmospheric profiles of altitude (km), pressure (mb), temperature ( $^{\circ}$ K), water vapor ( $\text{g}/\text{m}^3$ ), ozone density ( $\text{atm-cm}/\text{km}$ ), and aerosol density ( $= 0$ ) for Bolivia problem.

I N P U T   D A T A									
	ALT	ZDN	PRESS	TEMP	H2O DEN	O3 DEN	AER DEN		
1	4.5875+01	0.0000	2.0000+00	2.7765+02	2.5896-04	3.1335-04	0.0000		
2	2.6884+01	1.8989+01	2.1800+01	2.5913+02	2.7747-04	1.0331-02	0.0000		
3	2.2047+01	2.3828+01	4.1600+01	2.5223+02	2.8506-04	1.1897-02	0.0000		
4	1.9199+01	2.6676+01	6.1400+01	2.4762+02	2.9036-04	9.9547-03	0.0000		
5	1.7189+01	2.8686+01	8.1200+01	2.4411+02	2.9454-04	7.9341-03	0.0000		
6	1.5639+01	3.0236+01	1.0100+02	2.4123+02	2.9805-04	6.3654-03	0.0000		
7	1.4382+01	3.1493+01	1.2080+02	2.3879+02	3.1661-04	5.2012-03	0.0000		
8	1.3327+01	3.2548+01	1.4060+02	2.3667+02	7.5566-04	4.3325-03	0.0000		
9	1.2418+01	3.3457+01	1.6040+02	2.3477+02	1.6083-03	3.6726-03	0.0000		
10	1.1622+01	3.4253+01	1.8020+02	2.3367+02	3.1353-03	3.1610-03	0.0000		
11	1.0922+01	3.4953+01	2.0000+02	2.2601+02	5.8406-03	2.7611-03	0.0000		
12	1.0070+01	3.5805+01	2.2717+02	2.3167+02	1.1734-02	2.3333-03	0.0000		
13	9.2960+00	3.6579+01	2.5433+02	2.3669+02	2.1777-02	1.9967-03	0.0000		
14	8.5868+00	3.7288+01	2.8150+02	2.4120+02	3.8037-02	1.7272-03	0.0000		
15	7.9314+00	3.7944+01	3.0866+02	2.4528+02	6.3077-02	1.5082-03	0.0000		
16	7.3217+00	3.8553+01	3.3583+02	2.4900+02	1.0026-01	1.3279-03	0.0000		
17	6.7514+00	3.9124+01	3.6299+02	2.5241+02	1.5376-01	1.1777-03	0.0000		
18	6.2153+00	3.9660+01	3.9016+02	2.5555+02	2.2869-01	1.0513-03	0.0000		
19	5.7093+00	4.0166+01	4.1732+02	2.5847+02	3.3124-01	9.4396-04	0.0000		
20	5.2301+00	4.0645+01	4.4449+02	2.6117+02	4.6879-01	8.5201-04	0.0000		
21	4.7747+00	4.1100+01	4.7165+02	2.6370+02	6.5003-01	7.7268-04	0.0000		
22	4.3409+00	4.1534+01	4.9882+02	2.6606+02	8.8514-01	7.0376-04	0.0000		
23	3.9265+00	4.1949+01	5.2599+02	2.6827+02	1.1859+00	6.4352-04	0.0000		
24	3.6274+00	4.2248+01	5.4636+02	2.6984+02	1.4026+00	6.0319-04	0.0000		
25	3.3377+00	4.2537+01	5.6673+02	2.7134+02	1.7902+00	5.6646-04	0.0000		
26	3.0566+00	4.2818+01	5.8711+02	2.7278+02	2.1758+00	5.3292-04	0.0000		
27	2.7837+00	4.3091+01	6.0748+02	2.7416+02	2.6271+00	5.0223-04	0.0000		
28	2.5186+00	4.3356+01	6.2786+02	2.7548+02	3.1525+00	4.7405-04	0.0000		
29	2.2607+00	4.3614+01	6.4823+02	2.7674+02	3.7612+00	4.4814-04	0.0000		
30	2.0096+00	4.3865+01	6.6860+02	2.7796+02	4.4633+00	4.2426-04	0.0000		
31	1.7650+00	4.4110+01	6.8898+02	2.7913+02	5.2697+00	4.0219-04	0.0000		
32	1.5265+00	4.4349+01	7.0935+02	2.8053+02	6.1860+00	3.8176-04	0.0000		
33	1.2936+00	4.4581+01	7.2973+02	2.8188+02	7.2290+00	3.6279-04	0.0000		
34	1.0660+00	4.4809+01	7.5010+02	2.8319+02	8.4121+00	3.4516-04	0.0000		
35	8.4355-01	4.5031+01	7.7047+02	2.8446+02	9.7494+00	3.2873-04	0.0000		
36	6.2592-01	4.5249+01	7.9085+02	2.8569+02	1.1256+01	3.1342-04	0.0000		
37	4.1291-01	4.5462+01	8.1122+02	2.8689+02	1.2949+01	2.9911-04	0.0000		
38	2.0434-01	4.5671+01	8.3160+02	2.8806+02	1.4845+01	2.8572-04	0.0000		
39	0.0000	4.5875+01	8.5197+02	2.8919+02	1.6963+01	2.7318-04	0.0000		

$$\frac{We \frac{(z-z_0)}{h}}{h \left[ 1 + e^{\frac{(z-z_0)}{h}} \right]^2} \quad \text{atm-cm/km}$$

with  $W = 0.218$  atm-cm,  $z_0 = 23.23$  km, and  $h = 4.5$  km. Due to insufficient resolution in the ozone layer, ATRAD actually computes a total ozone amount of 0.200 atm-cm rather than 0.218 atm-cm. The remaining model parameters for Chad and Bolivia, consisting of sun angle, albedo, and surface temperature, are given in Table 3.9. Note the discontinuities in temperature at the surface in both problems. The  $\sigma$ -levels 0, 1/2, and 1 correspond to levels 11, 23, and 39 in the ATRAD atmosphere.

The 120 spectral intervals used by ATRAD for the Chad and Bolivia problems are 60(60)600(20)800(40)1200(80)1600(160)2400(240)4800(320)8000(500)11000(120)11120(380)11500(500)32000(1000)35000(1500)48500  $\text{cm}^{-1}$ . Anywhere from 6 to 12 Gaussian angles are used, depending on the degree of isotropy of the intensity in each hemisphere (upward and downward).

A point which was not noted in the previous comparisons between ATRAD and the older Katayama ('OK') model was that the two models use different solar constants. ATRAD uses the more current value of 1.94 ly/min<sup>[15]</sup> while the older Katayama model uses 2.00 ly/min. This has obvious consequences for the fluxes,

TABLE 3.9

Solar elevation ( $\theta_s$ ), albedo ( $\beta$ ), and surface temperature ( $T_g$ ) for Chad and Bolivia problems. ( $\beta=0$  for  $\lambda \geq 3\mu$ ).

	$\theta_s$	$\beta$	$T_g (^{\circ}\text{K})$
Chad	57.824	0.20	343.26
Bolivia	27.055	0.09	304.19

and, in fact, correcting the 'OK' solar fluxes to the more modern solar constant produces much better flux agreement between the two models in the solar spectrum. The revised flux tables are presented in Table 3.10. In spite of better agreement in the solar spectrum (differences no larger than 2.6% at any level), the poor agreement in the IR still causes the net fluxes to differ by as much as 20%. The average net flux disagreement between the two models, for all three levels and for both problems, is 8-1/2%. At their face value, errors of even as much as 20% may not seem disturbing. However, it is well to remember that we have been discussing fluxes and not flux differences. The picture as regards flux differences is much more bleak, as we shall see below.

Some comments on Table 3.10 are needed here, in light of the fact that these fluxes, and others like them, are used to construct the flux difference tables to follow. The first fact to note is the accuracy to which the fluxes are quoted. It has been found possible, in varying the spectral interval structure used in ATRAD for the Chad and Bolivia problems, to produce changes in the fluxes in the first place after the decimal point. Such changes are ascribed primarily to the exponential fitting algorithm, and to the way the intervals are arranged relative to the absorption bands. Perhaps when some of the problems are ironed out of the fitting algorithm (cf. Section 2.5) this limitation on the accuracy of ATRAD flux predictions will become less important. In the meantime, the ATRAD fluxes quoted in Table 3.10 are estimated to have an uncertainty of  $\pm 0.5$  watts/m<sup>2</sup> due essentially to the lack of infinitely fine spectral resolution. The impact of other errors (such as in the McClatchey transmission data<sup>[31]</sup> used by ATRAD) upon the fluxes has not been estimated as yet.

TABLE 3.10

Comparison between ATRAD (unparenthesized) and older Katayama model (parenthesized) flux predictions, in watts/m<sup>2</sup>, for Chad and Bolivia problems.

## CHAD (14°N, 20°E)

	$\sigma = 0$ (200 mb)	$\sigma = 1/2$ (567 mb)	$\sigma = 1$ (934 mb)
(1) IR (60 - 2640 cm <sup>-1</sup> )	-447.6 (-471.6)	-419.3 (-422.1)	-481.5 (-437.9)
(2) Near-IR (2640 - 11,120 cm <sup>-1</sup> )	345.6 ( 333.4)	316.2 ( 308.3)	270.5 ( 272.9)
(3) Visible (11,120 - 48,500 cm <sup>-1</sup> )	541.8 ( 554.9)	539.1 ( 554.9)	536.4 ( 554.9)
Solar [(2)+(3)]	887.4 ( 888.3)	855.3 ( 863.7)	806.9 ( 827.8)
Net [(1)+(2)+(3)]	440.4 ( 416.7)	436.0 ( 441.6)	325.4 ( 389.9)

## BOLIVIA (18°S, 65°W)

	$\sigma = 0$ (200 mb)	$\sigma = 1/2$ (526 mb)	$\sigma = 1$ (852 mb)
(1) IR (60 - 2640 cm <sup>-1</sup> )	-260.5 (-271.7)	-190.3 (-208.1)	-156.8 (-181.5)
(2) Near-IR (2640 - 11,120 cm <sup>-1</sup> )	207.0 ( 203.0)	170.7 ( 173.1)	128.2 ( 115.1)
(3) Visible (11,120 - 48,500 cm <sup>-1</sup> )	310.8 ( 308.4)	308.7 ( 308.4)	303.5 ( 308.4)
Solar [(2)+(3)]	517.8 ( 511.4)	479.4 ( 481.5)	431.7 ( 423.5)
Net [(1)+(2)+(3)]	257.3 ( 239.7)	289.1 ( 273.4)	274.9 ( 242.0)

The dividing point between the IR and solar spectra is not specified in the Katayama models, and so the value  $2640 \text{ cm}^{-1}$  ( $3.79\mu$ ) was selected based on the observation that in the interval  $2400\text{--}2640 \text{ cm}^{-1}$  the ATRAD net fluxes were primarily upward while in  $2640\text{--}2880 \text{ cm}^{-1}$  they were all downward. Moving the IR dividing point to  $2880 \text{ cm}^{-1}$  ( $3.47\mu$ ) would cause a uniform decrease in the magnitude of the IR fluxes of about  $1.7 \text{ w/m}^2$  for Chad and between  $1.1$  and  $1.6 \text{ w/m}^2$  for Bolivia. Moving it to  $2400 \text{ cm}^{-1}$  ( $4.17\mu$ ) would cause an increase in the magnitude of the IR fluxes of less than  $0.95 \text{ w/m}^2$  for both Chad and Bolivia. Of course, there would be compensatory changes in the solar-flux in both cases. The other dividing point, at  $11,120 \text{ cm}^{-1}$  ( $0.8993\mu$ ), is not exactly equal to the Katayama separation point of  $0.9\mu$ . Again, the change in visible vs. near IR flux resulting from this discrepancy is less than  $0.5 \text{ w/m}^2$ . These figures are quoted to show that the flux breakdown is not sensitive to the choice of either dividing point.

Not only the 'OK' value for the solar constant ( $2.00 \text{ ly/min}$ ), but also the fractional breakdown of the solar flux between  $\lambda > 0.9\mu$  and  $\lambda < 0.9\mu$ , can be called into question. Since either fraction determines the other, consider only the  $\lambda < 0.9\mu$  fraction,  $f_o$ . For the older and the newer Katayama models,  $f_o = 0.651$ . From the detailed spectral data of Thekaekara,<sup>[15]</sup>  $f_o = 0.634$ . But since the Katayama models neglect ozone, and since the stratospheric ozone layer will absorb all solar flux in the wavelength region  $\lambda < 0.3\mu$ , which amounts to  $1.2\%$  of the solar constant,<sup>[15]</sup> it should be reasonable to take  $f_o = 0.634 - 0.012 = 0.622$  (while leaving the  $\lambda > 0.9\mu$  fraction at  $1 - 0.634 = 0.366$ ). Or, if ozone were to be included in the same way that stratospheric water vapor is, the  $\lambda < 0.9\mu$  part of the solar flux could be appropriately attenuated between the top of the atmosphere and  $\sigma = 0$  ( $200 \text{ mb}$ ),

in which case  $f_0 = 0.634$  would be appropriate. However, because of the way in which absorption of solar flux is parameterized in the Katayama models, the atmospheric heating rates in the solar spectrum are independent of both  $f_0$  and the solar constant. Hence, the only impact of changing  $f_0$  and/or the solar constant is that the flux into the surface is changed. Let us derive the appropriate formulas for this surface flux from the treatment in Gates, et.al.,<sup>[80]</sup> for clear-sky situations.

We begin by defining the effective water vapor amount  $u^*$  between the surface and any level  $n$ :<sup>[80]</sup>

$$u_n^* = \frac{1}{g} \int_{p_n}^{p_s} q(p) \left( \frac{p}{p_0} \right)^\alpha dp \quad (3.24)$$

$q$  is the water vapor mixing ratio,  $\alpha$  is the pressure scaling factor,  $g$  is the acceleration due to gravity,  $p_s$  is the surface pressure, and  $u_n^*$  must be in units of  $g/cm^2$ . For the 'OK' model,  $\alpha = 1$ .  $n = \infty$  will refer to the top of the atmosphere. Also define

$$S_\infty^{sca} = f_0 S_0 \mu_0 \quad (3.25)$$

$$S_\infty^{abs} = (1 - f_0) S_0 \mu_0$$

which are the 'scattered' and 'absorbed' parts of the solar flux in terms of the fraction  $f_0$  discussed in the last paragraph, the solar constant  $S_0$ , and the cosine of the solar zenith angle  $\mu_0$ . The fractional absorption of the 'absorbed' part due to an amount  $u^*$  of water vapor is parameterized by



$$A(u^*, \mu_o) = \frac{0.189}{(1 - f_o) \bar{S}_o} (u^*/\mu_o)^{0.303} \quad (3.26)$$

where  $\bar{S}_o$  is the mean solar constant in ly/min. The 'absorbed' flux at any level  $n$  is therefore

$$S_n^{abs} = S_\infty^{abs} [1 - A(u_\infty^* - u_n^*, \mu_o)] \quad (3.27)$$

The flux differences between  $\sigma = 0$  and  $\sigma = 1/2$  and between  $\sigma = 1/2$  and  $\sigma = 1$  are then, respectively,

$$\begin{aligned} \Delta_1 &= S_0^{abs} - S_2^{abs} \\ &= 0.189 \mu_o (S_o/\bar{S}_o) \left[ \left( \frac{u_\infty^* - u_2^*}{\mu_o} \right)^{0.303} - \left( \frac{u_\infty^* - u_0^*}{\mu_o} \right)^{0.303} \right] \end{aligned} \quad (3.28)$$

$$\begin{aligned} \Delta_3 &= S_2^{abs} - S_4^{abs} \\ &= 0.189 \mu_o (S_o/\bar{S}_o) \left[ \left( \frac{u_\infty^*}{\mu_o} \right)^{0.303} - \left( \frac{u_\infty^* - u_2^*}{\mu_o} \right)^{0.303} \right] \end{aligned} \quad (3.29)$$

The ratio  $(S_o/\bar{S}_o)$  depends only on the Earth-sun distance. Therefore,  $\Delta_1$  and  $\Delta_3$  are independent of  $f_o$  and  $S_o$ . The scattered flux at all levels is

$$s^{sca} = s_{\infty}^{sca} \frac{(1-\beta)(1-\alpha_o)}{1-\beta\alpha_o} \quad (3.30)$$

where

$$\alpha_o = 0.085 - 0.247 \log_{10} \left( \frac{P_s \text{ (mb)}}{1000} \mu_o \right) \quad (3.31)$$

and where  $\beta$  is the surface albedo. The net solar flux into the surface is, therefore,

$$\begin{aligned} S_4 &= S_4^{abs} + S^{sca} \\ &= S_o \mu_o \left\{ (1-f_o) [1-A(u_{\infty}^*, \mu_o)] + f_o \frac{(1-\beta)(1-\alpha_o)}{1-\beta\alpha_o} \right\} \end{aligned} \quad (3.32)$$

The surface flux is proportional to  $S_o$ . (Lest the importance of using the best possible value of  $S_o$  to calculate  $S_4$  be underestimated, suffice it to say that the SMIC Report[85] associates a 1% decrease in  $S_o$  with a decrease in global average surface temperature of 1.5°C.) The dependence of  $S_4$  on  $f_o$  is slightly more complicated. The rate of change of  $S_4$  with  $f_o$  is

$$\frac{dS_4}{df_o} = S_o \mu_o \left\{ \frac{(1-\beta)(1-\alpha_o)}{1-\beta\alpha_o} - 1 \right\}$$

For  $\beta \in (0,1)$  and  $\alpha_o \in (0,1)$ , it can be shown that

$$\frac{dS_4}{df_o} < 0 \quad .$$

Therefore, if we decreased  $f_o$ , as proposed in the last paragraph, the surface flux  $S_4$  would increase. For both the Chad and Bolivia problems,  $S_4$  was calculated from Eq. (3.32) for  $f_o = 0.625$  and  $f_o = 0.651$  in order to determine the quantitative change in  $S_4$  produced. The results for Chad were

$$S_4 = \begin{cases} 827.1 \text{ w/m}^2 & f_o = 0.651 \\ 829.3 \text{ w/m}^2 & f_o = 0.625 \end{cases}$$

and for Bolivia,

$$S_4 = \begin{cases} 423.1 \text{ w/m}^2 & f_o = 0.651 \\ 425.6 \text{ w/m}^2 & f_o = 0.625 \end{cases}$$

The change in  $S_4$  in both cases is about 2 watts/m<sup>2</sup>, or 0.3% for Chad and 0.6% for Bolivia. This change is produced by a 4% change in  $f_o$ . Hence, it must be concluded that the results of the Katayama models are insensitive to  $f_o$ , except perhaps for extreme values of albedo, sun angle, etc.

While flux values have an intrinsic interest, it is really only flux differences between atmospheric levels which are used in a general circulation model (the only exception being that the net flux at the surface is used to compute surface heating). In our experience, the taking of such differences almost always leads to the loss of one (and sometimes two) significant digits, even when the levels are as widely separated as in the M/A 2-level GCM. Thus a flux-prediction model which is accurate to, say, 1% will have uncertainties in its flux difference predictions of the order of 10%. Even though the 'OK' model produces reasonable flux predictions, therefore, one cannot for that reason alone expect good flux difference predictions.

In Tables 3.11 and 3.12, the flux differences and surface fluxes as computed by ATRAD and by the newer and older Katayama models are presented. ATRAD computations were made with and without the ozone profile included, in order to assess the influence of ozone on heating rates. Before discussing these tables, however, some remarks need to be made on the newer Katayama ('NK') model.

The 'NK' model is described in an as yet unpublished manuscript written by Katayama at UCLA. Parts of this manuscript as well as a FORTRAN listing for the model were kindly furnished to us by Mr. Hans Giroux. The FORTRAN version of the model is used in UCLA's 3-level version of the M/A GCM. Rather than re-coding the 'NK' model for 2 levels, which is non-trivial, we ran it 'as-is' by putting one level between  $\sigma = 0$  and  $\sigma = 1/2$  and two levels ( $\sigma = 1/2$  to  $\sigma = 3/4$ ,  $\sigma = 3/4$  to  $\sigma = 1$ ) between  $\sigma = 1/2$  and  $\sigma = 1$ . This puts the increased resolution where most of the water vapor resides. The extra temperature values required (as compared to the 2-level model) were obtained using the temperature interpolation formulas of the 'OK' model.<sup>[80]</sup>

Two options were included for the 'NK' humidity profile. The first was to obtain the three mixing ratio values ( $Q_1$ ,  $Q_3$ ,  $Q_5$ ) required by the 'NK' model from the interpolation formula used in the 'OK' model.<sup>[80]</sup> The second was to insert the effective water vapor amounts ( $u^*$ ) into the 'NK' model directly, using the 'OK' values of  $q$  and  $\alpha$  ( $\alpha = 1$ ) in Eq. (3.24). The first option will be called the 'q-option,' the second the 'u\*-option.' Results from both options are given in Tables 3.11 and 3.12. Since both options use Eq. (3.24) to compute  $u^*$ , there are only two reasons for their absorber amounts to differ: (1) they use different  $q$ -profiles; or (2) they use different pressure scaling factors  $\alpha$ . In fact, the differences in absorber amount between the options are almost

TABLE 3.11

Flux differences and surface fluxes (watts/m<sup>2</sup>) for Chad as predicted by ATRAD with and without an ozone profile, and by the newer and older Katayama models ('NK' and 'OK' respectively). The unparenthesized 'NK' values are for the q-option, while the parenthesized ones are for the u\*-option. The upper level is  $\sigma = 0$  to  $\sigma = 1/2$ , the lower level is  $\sigma = 1/2$  to  $\sigma = 1$ .

	UPPER LEVEL				LOWER LEVEL			
	ATRAD	ATRAD (no O <sub>3</sub> )	'NK'	'OK'	ATRAD	ATRAD (no O <sub>3</sub> )	'NK'	'OK'
IR	-27.7	-33.1	-28.2 (-30.5)	-49.5	62.2	61.4	59.5 (53.5)	15.8
Solar	32.1	31.2	25.2 (24.6)	24.6	48.4	48.3	35.0 (35.9)	35.9
Net	4.4	-1.9	-2.9 (-6.0)	-24.9	110.6	109.7	94.5 (89.4)	51.7
Flux into Surface	325.4	335.4	329.7 (327.6)	389.9				

TABLE 3.12

Flux differences and surface fluxes (watts/m<sup>2</sup>) for Bolivia as predicted by ATRAD with and without an ozone profile, and by the newer ('NK') and older ('OK') Katayama models, with the same conventions applying as for Table 3.11.

	UPPER LEVEL				LOWER LEVEL			
	ATRAD	ATRAD (no O <sub>3</sub> )	'NK'	'OK'	ATRAD	ATRAD (no O <sub>3</sub> )	'NK'	'OK'
IR	-70.2	-72.2	-71.6 (-73.2)	-63.6	-33.5	-35.8	-25.5 (-31.2)	-26.6
Solar	38.4	38.0	31.3 (29.9)	29.9	47.7	47.6	58.4 (58.0)	58.0
Net	-31.7	-34.1	-40.3 (-43.4)	-33.7	14.1	11.8	32.9 (26.8)	31.4
Flux into Surface	274.9	282.1	240.7 (240.1)	242.0				

entirely due to different  $\alpha$ 's. (For 'OK',  $\alpha = 1$ ; for 'NK',  $\alpha = 0.6$ ; and for ATRAD, the McClatchey scheme<sup>[26]</sup> uses  $\alpha = 0.9$ , but with  $p/p_0$  replaced by  $p/p_0 (T_0/T)^{1/2}$  to account for the temperature variation of line half-width.) The mixing ratio profiles used in the 'OK' and 'NK' calculations were identical up to pressure level  $p_1$  ( $\sigma = 3/4$ ) in both models, and almost all the effective water vapor amount lies below this level.

The 'NK' model contains no improvements in the parameterization of the solar spectrum when clouds are absent. Hence the 'OK' solar flux differences agree with the 'NK'  $u^*$ -option flux differences. The 'NK' model, however, contains a considerably more sophisticated treatment of the IR, and its predictions of IR flux differences agree much more closely with ATRAD than do the 'OK' predictions. In the Chad problem, the net (solar + IR) flux differences and net surface flux predicted by 'NK' agree well with ATRAD and are a vast improvement over 'OK'. In the Bolivia problem, the 'NK' and 'OK' net flux difference predictions are close to each other in the lower level ( $\sigma = 1/2$  to  $\sigma = 1$ ) and both differ by roughly a factor of 2 from ATRAD. In the upper Bolivia layer, a fortuitous cancellation of errors in the solar and IR flux differences causes the net 'OK' flux difference to be very close to the ATRAD value(s); the 'NK' net flux difference is too large by roughly a factor of 4/3. Both the 'NK' and 'OK' surface flux predictions are off by about 14% for Bolivia. Thus, the following general conclusions emerge from the comparisons in Tables 3.11 and 3.12:

- (1) for a dry or a wet atmosphere, the IR treatment in the newer Katayama model is far superior to that in the older model;

- (2) there is no clear-cut advantage in the IR of the q-option over the u\*-option, that is, of a pressure scaling factor of 0.6 over one of 1.0; in the (dry) lower level of Chad, 0.6 is clearly preferable, while in the (wet) lower level of Bolivia, 1.0 is clearly preferable; in the (dry) upper levels of both problems, neither 0.6 nor 1.0 has a clear advantage;
- (3) the solar absorption treatment common to both Katayama models causes too little flux to be absorbed in dry levels (upper and lower Chad, upper Bolivia) and too much in wet levels (lower Bolivia);
- (4) for a dry atmosphere, the newer Katayama model is vastly superior to the older one in predicting net heating rates and surface fluxes; for a wet atmosphere, the newer Katayama model may actually be slightly worse than the older one in predicting those same quantities;
- (5) ozone has a substantial impact on the heating rates of the upper levels, and even affects the heating rate of the Bolivian lower level non-negligibly; the effect is concentrated almost entirely in the IR and thus is due to the  $O_3$  9.6 $\mu$  band.



In order to quantify the statements above referring to 'dry' and 'wet,' let us note that the effective water vapor amounts for Chad and Bolivia are as given in Table 3.13. Thus, 'dry' means having effective water vapor content less than  $\sim 0.2$  g/cm<sup>2</sup> and 'wet' means having effective water vapor content larger than  $\sim 1.7$  g/cm<sup>2</sup>.

TABLE 3.13

Effective water vapor amounts in g/cm<sup>2</sup> in upper ( $\sigma = 0$  to  $\sigma = 1/2$ ) and lower ( $\sigma = 1/2$  to  $\sigma = 1$ ) levels for Chad and Bolivia, for pressure scaling factors ( $\alpha$ ) of 0.6 to 1.0 and for ATRAD.

	CHAD		BOLIVIA	
	Upper	Lower	Upper	Lower
'NK' $\sigma = 0.6$	0.01715	0.15294	0.10267	2.00645
'OK' $\sigma = 1.0$	0.01217	0.13775	0.07249	1.73746
ATRAD $\alpha = 0.9$	0.01341	0.13538	0.07983	1.76058

In view of the fact that the IR seems to be in fairly good shape for clear-sky situations, if the newer Katayama treatment is used, the main difficulty in predicting clear-sky heating rates centers around the absorption of solar radiation in the atmosphere. In order to localize the source of the error, we first checked the Katayama model assumption that Rayleigh scattering could be ignored for  $\lambda > 0.9\mu$ . For the spectral interval 3360 - 11,000 cm<sup>-1</sup> for the Chad problem, we found that ignoring Rayleigh scattering increased all the net fluxes by 0.5 watts/m<sup>2</sup> and did not affect the heating rates

at all. This is truly a negligible effect, although a more thorough study might show a marginally non-negligible effect, perhaps at high albedos and/or low sun angles. Similarly, an examination of ATRAD runs with and without ozone (Tables 3.11 and 3.12) showed that the largest solar flux difference change as a result of neglecting ozone was  $0.9 \text{ watts/m}^2$ , which cannot begin to account for the errors in solar heating rate. The only other important absorbers in the solar spectrum beside ozone are water vapor and  $\text{CO}_2$ . Thus, the Katayama model errors must be due to some combination of the following causes:

- (1) the parameterization of the absorption of solar down-flux by water vapor [Eq. (3.26)];
- (2) the neglect of the absorption of the surface-reflected solar up-flux;
- (3) the neglect of  $\text{CO}_2$  absorption.

A comparison of the solar up- and down-flux differences for Chad and Bolivia is presented in Table 3.14. We have broken these results down further into  $\lambda < 0.9\mu$  and  $\lambda > 0.9\mu$  values, but this breakdown is rather artificial since as we have shown in Eqs. (3.28) and (3.29) the Katayama parameterization is independent of any partitioning of the solar spectrum. The breakdown is shown primarily to illustrate the error incurred if one were to lump all absorption into  $\lambda > 0.9\mu$ .

The salient facts which emerge from Table 3.14 are:

- (1) there is a fundamental disagreement between ATRAD and the Katayama parameterization of absorbed solar flux [Eqs. (3.28) and (3.29)] whether or not we include the absorbed near IR ( $\lambda > 0.9\mu$ ) up-flux and absorbed 'visible' ( $\lambda < 0.9\mu$ ) flux; (2) the absorbed near-IR up-flux is at most an 8%

TABLE 3.14

Flux differences (watts/m<sup>2</sup>) in the near-IR (2640 - 11,120 cm<sup>-1</sup>) and 'visible' (11,120 - 48,500 cm<sup>-1</sup>) for the Chad and Bolivia problems. Near-IR values are broken down into contributions from up-flux and down-flux. ATRAD with no ozone (unparenthesized) predictions are compared with Katayama model (parenthesized) predictions.

## CHAD

		$\sigma=0$ to 1/2	$\sigma=1/2$ to 1
(1)	2640 - 11,120 cm <sup>-1</sup> , down	29.2 (24.6)	41.6 (35.9)
(2)	2640 - 11,120 cm <sup>-1</sup> , up	0.1 (0)	4.1 (0)
(3)	11,120 - 48,500 cm <sup>-1</sup>	1.8 (0)	2.6 (0)
	Solar [(1)+(2)+(3)]	31.2 (24.6)	48.3 (35.9)

## BOLIVIA

		$\sigma=0$ to 1/2	$\sigma=1/2$ to 1
(1)	2640 - 11,120 cm <sup>-1</sup> , down	36.4 (29.9)	41.7 (58.0)
(2)	2640 - 11,120 cm <sup>-1</sup> , up	-0.1 (0)	0.9 (0)
(3)	11,120 - 48,500 cm <sup>-1</sup>	1.7 (0)	5.1 (0)
	Solar [(1)+(2)+(3)]	38.0 (29.9)	47.6 (58.0)

effect (in the Chad lower level) but may be decidedly non-negligible for dry problems with albedos substantially larger than the 0.20 of Chad; and (3) the absorbed 'visible' flux is at most an 11% effect (in the Bolivian lower level) and is thus marginally negligible. Clearly there are fundamental difficulties with the function  $A(u^*, \mu_0)$  of Eq. (3.26); it simply causes too much absorption in wet levels and not enough in dry ones. The simplified model which we shall present below offers an attractive alternative in the search for a replacement for  $A$ . Also, we shall comment on the possibility of simply improving on  $A$  itself, by changing its parameters.

The simple model to which we refer ignores Rayleigh scattering and thermal emission in the spectral region  $2640 - 11,120 \text{ cm}^{-1}$ . ATRAD calculations have demonstrated that including Rayleigh scattering in this region produces a very small net flux decrease at all levels. The Planck function effect is even smaller, even for the high temperatures of Chad. Hence, the radiative transfer equation reduces to

$$\mu_{\nu} \frac{\partial I_{\nu}}{\partial z} = - \alpha'_{\nu}(z) I_{\nu} \quad , \quad \nu \in [2640 - 11,120] \quad .$$

where  $\alpha'_{\nu}$  is the absorption coefficient. If the boundary condition at the top of the atmosphere is

$$I_{\nu} \Big|_{z=0} = S_{\nu} \delta(\vec{\Omega} - \vec{\Omega}_0)$$

(for solar flux  $S_{\nu}$ ) then the down-flux is simply

$$F_{\nu}^{\downarrow} = \mu_0 S_{\nu} \exp \left[ - \frac{1}{\mu_0} \int_0^z \alpha'_{\nu}(z) dz \right] \quad (3.33)$$

If an albedo  $\beta_v$  and diffuse reflection at the surface  $z = z_g$  are assumed, the up-flux is

$$F_v^\uparrow = 2\beta_v F_v^\uparrow(z_g) E_3 \left[ \int_z^{z_g} \alpha'_v(z) dz \right] \quad (3.34)$$

where  $E_3$  is the exponential integral of third degree. Equations (3.33) and (3.34) constitute a simple model for the near-IR when the atmosphere is aerosol-free. Calculations have so far been performed only with Eq. (3.33) in order to compare both with ATRAD and with the Katayama model.

The calculations for Eq. (3.33) were actually performed with the frequency-averaged form

$$F_{\Delta v}^\uparrow(z) = \mu_o S_{\Delta v} T_{\Delta v}^{H_2O} \left[ u^*(0 \rightarrow z) / \mu_o \right] T_{\Delta v}^{CO_2} \left[ w^*(0 \rightarrow z) / \mu_o \right] \quad (3.35)$$

where

$$S_{\Delta v} = \frac{1}{\Delta v} \int_v^{v+\Delta v} S_v dv$$

(as estimated by cubic interpolation in Thekaekara's tables<sup>[15]</sup> and where  $T_{\Delta v}$  is the transmission function for either water vapor, for vertical  $H_2O$  amount  $u^*(0 \rightarrow z)$  between 0 and  $z$ , or for vertical  $CO_2$  amount  $w(0 \rightarrow z)$ , taken from McClatchey, et. al.<sup>[26]</sup> Using an interval  $\Delta v = 20 \text{ cm}^{-1}$ , the fluxes from Eq. (3.35) were summed across the entire spectral region 2640 - 11,120  $\text{cm}^{-1}$  to yield the results of Table 3.15. Calculations were made with and without  $CO_2$ . Comparison values of down-flux and down-flux difference are presented as predicted by ATRAD and by Katayama (Eqs. (3.26) and (3.29)). The ATRAD spectral

TABLE 3.15

2640 - 11,120  $\text{cm}^{-1}$  down-fluxes in  $\text{watts/m}^2$  at the top of the atmosphere ( $F_{\text{top}}^{\dagger}$ ) and at  $\sigma = 0, 1/2$ , and 1 ( $F_0^{\dagger}, F_{1/2}^{\dagger}, F_1^{\dagger}$ ), and down-flux differences across the upper and lower levels ( $\Delta F_0^{\dagger} - 1/2$  and  $\Delta F_{1/2}^{\dagger} - 1$  respectively) for the Chad and Bolivia problems, as predicted by three different models [Eq. (3.35) with  $\Delta\nu = 20 \text{ cm}^{-1}$ , ATRAD and Katayama].

## CHAD

	$F_{\text{top}}^{\dagger}$	$F_0^{\dagger}$	$F_{1/2}^{\dagger}$	$F_1^{\dagger}$	$\Delta F_0^{\dagger} - 1/2$	$\Delta F_{1/2}^{\dagger} - 1$
Equation (3.35), no $\text{CO}_2$	416.3	414.1	386.4	344.8	27.7	41.6
Equation (3.35)	416.3	409.4	381.3	340.0	28.1	41.3
ATRAD	416.3	410.4	381.2	339.6	29.2	41.6
Katayama	408.7	401.6	377.0	341.1	24.6	35.9

## BOLIVIA

	$F_{\text{top}}^{\dagger}$	$F_0^{\dagger}$	$F_{1/2}^{\dagger}$	$F_1^{\dagger}$	$\Delta F_0^{\dagger} - 1/2$	$\Delta F_{1/2}^{\dagger} - 1$
Equation (3.35), no $\text{CO}_2$	223.7	221.4	185.3	143.2	36.1	42.1
Equation (3.35)	223.7	218.5	183.1	141.3	35.3	41.8
ATRAD	223.7	219.4	183.0	141.3	36.4	41.7
Katayama	219.6	214.4	184.5	126.5	29.9	53.0

interval structure for these calculations was 2640(240) 4800 (320) 8000(500) 11,000(120) 11,120  $\text{cm}^{-1}$ , so that the ATRAD frequency resolution was considerably coarser than that of Eq. (3.35). The predictions of Eq. (3.35) confirm the ATRAD predictions remarkably well, and in fact Table 3.15 furnishes an excellent validation of the exponential fitting idea upon which ATRAD is based. The residual differences between ATRAD and Eq. (3.35) must be partly due to Rayleigh scattering, partly due to the approximation of  $T_{\Delta v}$  by an exponential sum in ATRAD, and partly due to ATRAD's coarser spectral resolution. Removing  $\text{CO}_2$  from the atmosphere causes the near-IR down-flux to change by at most  $1 - 1\frac{1}{2}\%$ , and the largest tropospheric change in down-flux difference is  $0.8 \text{ watt/m}^2$ . The primary impact of  $\text{CO}_2$  in the near-IR is to change the stratospheric heating, which is grossly mis-estimated if only water vapor is considered. Note that the inclusion of  $\text{CO}_2$  in the model of Eq. (3.35) actually decreases the heating rate due to near-IR down-flux in the upper and lower Bolivian and lower Chad levels. This points up the unreliability of simple intuition in complex radiative transfer problems. The only reliable intuitive deduction is that the fluxes must decrease when the effects of  $\text{CO}_2$  are added, and Table 3.15 of course bears this out. In the discussion of the solar absorption function A which follows, the Eq. (3.35) predictions without  $\text{CO}_2$  shall be used as benchmark values.

None of the results of Table 3.15 contradict the observation, made in connection with Table 3.14, that the function A [Eq. (3.26)] is deficient in both wet and dry situations. An obvious direction one might take in order to improve the parameterization would be to study the predictions of the simple model Eq. (3.35) and derive a new empirical function to replace A. In the long run, this will be the only satisfactory way to proceed. Undoubtedly, this new function should be of a tabular nature in order to eliminate

the computing costs associated with analytic functions like Eq. (3.26).

In the shorter term, however, it would be desirable to re-parameterize  $A$  in order to make it more accurate. There are three possible ways to do this: (1) change the definition of  $u^*$ ; (2) change the coefficient (0.187); and (3) change the exponent (0.303). As far as changing  $u^*$  goes, although there are infinitude of exotic formulas one might consider, we shall restrict ourselves to observing what change in the pressure scaling factor  $\alpha$  (see Eq. (3.24)) would improve matters. But we already have sufficient information at hand in Table 3.11 and 3.12 to observe how changing  $\alpha$  from 1.0 (parenthesized 'NK' values) to 0.6 (unparenthesized 'NK' values) affects the absorbed solar flux. The conclusion one is forced to draw is that there is no net gain with  $\alpha = 0.6$  - the results in both the Chad and Bolivia upper levels are slightly improved, in both lower levels slightly worse. Furthermore, the changes in Katayama's model solar absorption resulting from varying  $\alpha$  are much too small to offer any hope that agreement with ATRAD can be obtained in this fashion.

Next we consider if  $A$  can be improved by changing its exponent. To this end, we present in Table 3.16 calculations of the upper and lower level flux differences ( $\Delta_1$  and  $\Delta_3$ ) from Eqs. (3.28) and (3.29) with varying exponent. The values of  $u^*$  used are those of the 'OK' model in Table 3.13. For Chad, a value of the exponent between 0.25 and 0.303 would lead to agreement of  $\Delta_1$  with Eq. (3.35), but the value of  $\Delta_3$  would be made worse thereby. On the other hand, there is no exponent which would lead to agreement of  $\Delta_3$  with Eq. (3.35); the maximum  $\Delta_3$  attainable by varying the exponent (36.3 watts/m<sup>2</sup>) is still 12% below the Eq. (3.35) value. As for Bolivia, there is no exponent which will bring  $\Delta_1$  into agreement with Eq. (3.35); no



TABLE 3.16

Predictions of Eqs. (3.28) and (3.29) for solar flux differences (watts/m<sup>2</sup>) across upper ( $\Delta_1$ ) and lower ( $\Delta_3$ ) layers as we vary the exponent from the Katayama value of 0.303, for Chad and Bolivia problems. The predictions of Eq. (3.35) are included for comparison.

CHAD			BOLIVIA		
Exponent	$\Delta_1$	$\Delta_3$	Exponent	$\Delta_1$	$\Delta_3$
0.10	29.2	21.3	0.10	23.8	19.4
0.15	31.7	27.6	0.15	28.4	28.9
0.20	30.8	31.8	0.20	30.4	38.3
0.25	28.1	34.4	0.215	30.6	41.2
0.303	24.6	35.9	0.25	30.7	47.9
0.325	23.1	36.2	0.303	29.9	58.0
0.35	21.4	36.3	0.325	29.4	62.3
0.375	19.7	36.3	0.35	28.7	67.2
0.40	18.1	36.1	0.40	27.0	77.1
0.45	15.1	35.4	0.50	23.4	97.8
0.50	12.6	34.3	0.60	19.9	120.0
0.60	8.5	31.4			
Equation (3.35)	27.7	41.6	Equation (3.35)	36.1	42.1

matter how we vary the exponent,  $\Delta_1$  remains at least 15% too small. However, an exponent of about 0.215 will force  $\Delta_3$  into agreement with Eq. (3.35), and this exponent also leads to a slightly better value of  $\Delta_1$ . But an exponent of 0.215 leads to definitely worse values of  $\Delta_1$  and  $\Delta_3$  for Chad. Hence, there seems to be no exponent which is consistently better than 0.303.

Next, we ask if any value of the coefficient of  $A$  would be better than 0.189. But the error we are dealing with is not monosigned. A larger coefficient is needed for levels with a small amount of water vapor, and vice versa.

Finally, there remains the possibility that some judicious variation of both the coefficient and exponent might improve  $A$ . The exponent first must be changed so that all the errors are monosigned, then the coefficient changed to bring  $A$  into agreement with Eq. (3.35). An examination of Table 3.16 reveals that  $\Delta_3$  for Chad can never be larger than 36.3 watts/m<sup>2</sup> (and needs to be 41.6 watts/m<sup>2</sup>) and that  $\Delta_1$  for Bolivia can never exceed 30.7 watts/m<sup>2</sup> (and needs to be 36.1 watts/m<sup>2</sup>) no matter how we vary the exponent. Thus, the exponent can be varied so that all values of  $\Delta_1$  and  $\Delta_3$  are less than Eq. (3.35) predictions, but not vice versa. In order to make  $\Delta_3$  for Bolivia less than 42.1 watts/m<sup>2</sup>, the exponent must be less than  $\sim 0.215$ . But for exponents  $< 0.215$ , we find  $\Delta_1 \geq \Delta_3$  (roughly) for Chad so that no coefficient adjustment could ever produce agreement with Eq. (3.35).

Thus, the resolution of the difficulty really awaits the creation of the new tabular function of which we spoke earlier.

### 3.5 ATRAD COMPARED WITH KATAYAMA MODEL FOR ARCTIC STRATUS PROBLEM

The Arctic stratus problem was discussed in detail in Section 3.3. We continue that discussion here by briefly

comparing some of the Katayama model cloudy-sky approximations against ATRAD.

### 3.5.1 Scattering in the IR

It is assumed in the Katayama model, and indeed by practically all extant radiation models, that scattering in the IR can be neglected. However, until the advent of ATRAD, no model was capable of actually checking this assumption, for the combined line absorption-scattering problem was viewed as insuperable. As a start towards examining this assumption quantitatively, therefore, two ATRAD calculations were made for the IR ( $60 - 1920 \text{ cm}^{-1}$ ) spectral region for the Arctic stratus problem. The first included Mie scattering in the normal fashion, the second was identical to the first in all respects save that the Mie scattering coefficient (but not the Mie absorption coefficient) was set to zero. Selected results from these calculations for down-flux, up-flux, net flux, and heating rate (flux difference) are presented in Table 3.17. The impact of ignoring scattering may be summarized as follows:

- (a) the down-flux below the cloud is decreased by  $1.5 \text{ watts/m}^2$ , or 0.5%; above the cloud, it is unchanged;
- (b) the up-flux above the cloud is increased by  $1-2 \text{ watts/m}^2$ , or 0.5%; below the cloud, it is unchanged;
- (c) the net flux becomes more negative by  $1.1-2.2 \text{ watts/m}^2$ ;
- (d) heating rates are unaffected except in the cloud (0.7%) and immediately above the cloud (3.3%).

TABLE 3.17

Comparison between ATRAD predictions for down-flux  $F\downarrow$ , up-flux  $F\uparrow$ , net flux  $F$ , and net flux differences  $\Delta F$  (all in  $\text{watts/m}^2$ ) as a function of altitude  $z$  (km) and pressure  $p$  (mb) for  $60 - 1920 \text{ cm}^{-1}$  for the Arctic stratus problem. Unparenthesized values are for full Mie treatment and parenthesized values are for Mie scattering zeroed out. (The cloud is located between 0.5 and 1.0 km,  $T_g = 273^\circ\text{K}$  except where noted.)

$z$	$p$	$F\downarrow$	$F\uparrow$	$F$
0.0	1012.5	327.5 (326.0)	311.7 (311.7)	15.8 ( 14.2)
0.5	951.9	323.9 (322.3)	322.4 (322.4)	1.5 ( -0.1)
1.0	895.0	236.7 (236.5)	322.0 (324.0)	-85.3 ( -87.5)
2.0	790.2	210.1 (210.1)	316.4 (318.0)	-106.4 (-107.9)
5.0	536.7	127.5 (127.5)	244.8 (246.0)	-153.7 (-155.0)
10.0	262.6	43.7 ( 43.7)	244.8 (246.0)	-201.1 (-202.3)
50.0	1.0	1.2 ( 1.2)	245.5 (246.6)	-244.3 (-245.4)

$\Delta z$	$\Delta F$	$\Delta F (T_g = 300^\circ\text{K})$
0.0 - 0.5	-14.3 (-14.3)	65.2
0.5 - 1.0	-86.8 (-87.4)	-31.3
1.0 - 2.0	-21.1 (-20.4)	-20.7
2.0 - 5.0	-47.3 (-47.1)	-47.1
5.0 - 10.0	-47.4 (-47.3)	-47.2
10.0 - 50.0	-43.2 (-43.1)	-43.0

Thus, the neglect of Mie scattering is borne out extremely well for water clouds at least as optically thick as the Arctic stratus cloud. The strong absorption due to liquid water in the IR is, of course, responsible for the suppression of scattering in the cloud, and thus this result might not apply to an aerosol material with transmission windows in the IR. It may also be inapplicable to optically thin clouds, particularly cirrus.

### 3.5.2 Sensitivity to Surface Temperature

Because of the large inaccuracies involved in the computation of the Mintz-Arakawa surface temperature  $T_g$ , it is of interest to assess the sensitivity of radiative heating and cooling rates in the atmosphere to this parameter. A normal ATRAD calculation of the Arctic stratus problem for  $60 - 1920 \text{ cm}^{-1}$ , with  $T_g = 273^\circ\text{K}$  was, therefore, compared with a similar calculation with  $T_g = 300^\circ\text{K}$ . In the first case, the surface is  $\sim 5^\circ\text{K}$  colder than the cloud-to-ground layer and  $\sim 3^\circ\text{K}$  colder than the cloud; in the second case, the surface is  $\sim 22^\circ\text{K}$  warmer than the cloud-to-ground layer and  $\sim 24^\circ$  warmer than the cloud. The changes in heating rate between the two cases may be observed in Table 3.16. The cloud-to-ground layer, which was cooling for  $T_g = 273^\circ$ , is heating for  $T_g = 300^\circ$ , and at almost five times the rate at which it was formerly cooling. The cloud is cooling in both cases, but only one-third as rapidly for  $T_g = 300^\circ$  as for  $T_g = 273^\circ$ . The cooling of all levels above the cloud is practically unchanged, so that the cloud effectively shields these upper levels from the effects of a surface temperature change. In spite of this shielding, however,  $\Delta F$  for 0 to 5 Km is  $-169.5 \text{ watts/m}^2$  for  $T_g = 273^\circ\text{K}$  and  $-33.9 \text{ watts/m}^2$  for  $T_g = 300^\circ\text{K}$ , so that the cooling of the

whole lower half of the atmosphere is dramatically reduced (by a factor of 5) as a result of a 10% increase in surface temperature.

These results establish the sensitivity of IR heating and cooling to surface temperature. There is very little point in having a reasonably sophisticated IR treatment in the Mintz-Arakawa GCM if it is only to be coupled with an inadequate predictive scheme for  $T_g$ .

### 3.5.3 Cloud Albedo

A quantity which is required in all the Katayama parameterizations relating to clouds is the cloud albedo,  $\alpha_c$ . In the 'OK' model  $\alpha_c$  is always either 0.6 or 0.7. In the 'NK' model  $\alpha_c$  assumes different values for  $\lambda > 0.9\mu$  and  $\lambda < 0.9\mu$ , and ranges all the way from 0.19 (for high cloud) to 0.76 (for cumulonimbus cloud). For low cloud, into which class the Arctic stratus cloud must fall, the 'NK' model assumes  $\alpha_c = 0.66$  for  $\lambda < 0.9\mu$  and  $\alpha_c = 0.50$  for  $\lambda > 0.9\mu$ .

Section 3.3 contained an extensive discussion of cloud albedo, particularly as it related to surface fluxes. A model was developed for cloud 'albedo' ( $F_{ct}^{\uparrow}/F_{ct}^{\downarrow}$ ) as it would actually be observed, as a function of surface albedo  $\beta$ . Only for  $\beta = 0$  do we recover the actual cloud albedo  $\alpha_c$ , which is an intrinsic property of the cloud, from a measurement of  $F_{ct}^{\uparrow}/F_{ct}^{\downarrow}$  (ct = cloud top). The Katayama model does not include this dependence on  $\beta$ , nor indeed does it include any dependence on droplet concentration, cloud thickness, and solar elevation  $\theta_s$ . ATRAD is an ideal vehicle for studying these various dependencies with a view to parameterizing them. As an example, consider the results

of Table 3.18, in which the variation of  $F_{ct}^{\uparrow}/F_{ct}^{\downarrow}$  over a limited range of sun angles and albedos is shown. It is important to remember that all of these albedo values are for exactly the same cloud. The hopelessness of approximating cloud 'albedo' as a single number, rather than a function of several parameters, is brought home with particular force here. We feel that the lack of a parameterization for cloud albedo in the Katayama model is its most serious deficiency for cloudy-sky situations. Until such a parameterization is obtained, the other formulas in the Katayama model which use cloud 'albedo' can only be believed insofar as they have a certain climatological correctness built into them.

TABLE 3.18

The ATRAD-predicted ratio of up-flux at the cloud-top ( $F_{ct}^{\uparrow}$ ) to down-flux at the cloud top ( $F_{ct}^{\downarrow}$ ) for the Arctic stratus problem, for various values of solar elevation  $\theta_s$  and surface albedo  $\beta$ . Unparenthesized values are for the full spectral interval  $3600 - 48,500 \text{ cm}^{-1}$ . The first parenthesized value refers to  $3600 - 11,000 \text{ cm}^{-1}$  only, the second parenthesized value refers to  $11,000 - 48,500 \text{ cm}^{-1}$  only.

$F_{ct}^{\uparrow}/F_{ct}^{\downarrow}$			
$\theta_s$ $\beta$	20°	30°	40°
0.	0.52 (0.52,0.52)	0.44 (0.44,0.44)	0.37 (0.36,0.38)
0.20	0.58 (0.57,0.58)	0.51 (0.49,0.52)	0.45 (0.43,0.46)
0.58	0.72 (0.69,0.74)	0.68 (0.64,0.70)	0.64 (0.59,0.66)
0.79	0.83 (0.78,0.85)	0.80 (0.74,0.83)	0.78 (0.71,0.81)

### 3.5.4 Albedo of a Cloudy Atmosphere

Presume that we know the cloud albedo

$$R' = \frac{F_{ct}^{\uparrow}}{F_{ct}^{\downarrow}}$$

for  $\lambda < 0.9\mu$ . Then let us enquire into the accuracy of the Katayama approximation

$$\alpha_{atm} = 1 - (1-R')(1-\alpha_0) \quad (3.36)$$

for the albedo  $\alpha_{atm}$  of the whole atmosphere in the presence of a single cloud layer.  $\alpha_0$  is the albedo of the corresponding clear atmosphere due to Rayleigh scattering, and is approximated as in Eq. (3.31) by the Katayama model. In Table 3.19 are assembled values of  $\alpha_{atm}$  for the Arctic stratus problem as predicted by ATRAD and by Eq. (3.36) for the spectral region  $11,000 - 48,500 \text{ cm}^{-1}$ . The large error in the formula (3.36) is clearly apparent. In these examples, Eq. (3.36) seriously overestimates the cloudy atmospheric albedo, whether one compares it with the ATRAD value at the top of the atmosphere (1 mb) or at 167 mb (the difference in the ATRAD values at 1 mb and 167 mb is due to Rayleigh scattering and ozone absorption between the two levels). Our parameter studies have not been extensive enough, however, to say with certainty whether Eq. (3.36) always overestimates the cloudy atmospheric albedo. One interesting observation, however, is that the error cannot be laid on the approximation (3.31) for  $\alpha_0$ . According to the unpublished Katayama manuscript describing the new model, the correct  $\alpha_0$  should be even larger than Eq. (3.31) predicts for  $\theta_s = 33.6^\circ$ .



TABLE 3.19

Comparisons of cloudy atmospheric albedo  $\alpha_{\text{atm}}$  as calculated by Eq. (3.36) (using the  $R'$  values shown) and by ATRAD at 1 mb and 167 mb, for  $11,000 - 48,500 \text{ cm}^{-1}$  for the Arctic stratus problem with surface albedo  $\beta = 0$  and various values of solar elevation  $\theta_s$ .

$\theta_s$	$R'$ (ATRAD)	$\alpha_{\text{atm}}$ (Eq. 3.36)	$\alpha_{\text{atm}}$ (1 mb) (ATRAD)	$\alpha_{\text{atm}}$ (167 mb) (ATRAD)
20°	0.5162	0.612	0.497	0.534
30°	0.4438	0.531	0.430	0.459
40°	0.3758	0.457	0.369	0.391

Thus, at least for the  $\theta_s = 30^\circ$  case in Table 3.19, the prediction of  $\alpha_{\text{atm}}$  in Eq. (3.36) would be even worse if the correct  $\alpha_o$  were used.

It need hardly be emphasized that significant errors in  $\alpha_{\text{atm}}$  have serious consequences for the prediction of climate. Even simple global climatic models, such as that of Budyko,<sup>[85]</sup> point up the sensitivity of the Earth's surface temperature to fluctuations in the atmospheric albedo.

## REFERENCES

1. Howell, H. and H. Jacobowitz, "Matrix Method Applied to Multiple Scattering of Polarized Light," J. Atmos. Sci. (1970), Vol. 27, p. 1195.
2. Dave, J. "Subroutines for Computing the Parameters of the Electromagnetic Radiation Scattered by a Sphere," IBM Program 360D - 17.4.002 (December 1968).
3. Kerker, M., The Scattering of Light and Other Electromagnetic Radiation, Academic Press, New York (1969).
4. Hodkinson, F., Proceedings of Inter-disciplinary Conference on Electromagnetic Scattering, Potsdam, N.Y., 1962, Pergamon Press, London (1963).
5. Ellison, J., Proc. Phys. Soc. B, (1957), Vol. 10, p. 102.
6. Holland, A. and G. Gagne, "The Scattering of Polarized Light by Polydisperse Systems of Irregular Particles," Appl. Opt. (1970), Vol. 9, p. 1113.
7. Hall, F., Appl. Opt. (1968), Vol. 7, p. 891.
8. Houghton, J. and G. Hunt, "The Detection of Ice Clouds From Remote Measurements of Their Emission in the Far Infrared," Qtrly. J. R. Met. Soc. (1971), Vol. 97, p. 1.
9. Jacobowitz, H., "A Method for Computing the Transfer of Solar Radiation Through Clouds of Hexagonal Ice Crystals," JQSRT (1971), Vol. 11, p. 691.
10. Kondrat'yev, K., Radiation in the Atmosphere, Academic Press, New York (1969).
11. Hoover, G., et. al., "Infrared Absorption by Overlapping Bands of Atmospheric Gases," Appl. Opt. (1967), Vol. 6, p. 481.
12. Milne, E. A., Thermodynamics of the Stars, in Selected Papers on the Transfer of Radiation, D. Menzel, Editor, Dover, New York (1966).

13. Siegel, R. and J. Howell, "Thermal Radiation Heat Transfer, Vol. III," SP-164, NASA (1971).
14. Woolf, H., "On the Computation of Solar Elevation Angles and the Determination of Sunrise and Sunset Times," TM-X-1646, NASA (1968).
15. Thekaekara, M., et. al., "The Solar Constant and the Solar Spectrum Measured From a Research Aircraft," Technical Report TR-R-351, NASA (1970).
16. Siegel, R. and J. Howell, "Thermal Radiation Heat Transfer, Vol. I," Special Publication SP-164, NASA (1968).
17. Cox, C. and W. Munk, "Slopes of the Sea Surface Deduced From Photographs of Sun Glitter," Bull. Scripps Inst. Oceanog., Vol. 6 (1956), p. 401.
18. Boileau, A. and J. Gordon, "Atmospheric Properties and Reflectances of Ocean Water and Other Surfaces for a Low Sun," Appl. Opt., Vol. 5 (1966), p. 803.
19. McStravick, D., "The Effect of Surface Roughness on the Reflected and Emitted Energy From a Rough Surface," Ph.D. Thesis, Rice University, Texas (1972).
20. Paltridge, T., J. Geophys. Res., Vol. 76 (1971), p. 2857.
21. Earing, D. and J. Smith, "Target Signatures, Analysis Center: Data Compilation," Willow Run Labs., Institute of Science and Techn., Univ. of Mich., Ann Arbor (1966).
22. Kyle, T., "Calculations of Atmospheric Transmittance From 1.7 to 20  $\mu$ ," JQSRT, Vol. 9 (1969), p. 1477.
23. Goody, R., Atmospheric Radiation, Oxford Univ. Press, London (1964).
24. Wyatt, P., et. al., Appl. Opt., Vol. 3 (1964), p. 229.
25. Smith, W., "A Polynomial Representation of CO<sub>2</sub> and H<sub>2</sub>O Vapor Transmission," ESSA Tech. Report NESC-47, National Environmental Satellite Service, Washington, D.C. (1969).
26. McClatchey, R., et. al., "Optical Properties of the Atmosphere," AFCRL-70-0527, Air Force Cambridge Research Labs., Cambridge, Mass. (1970).

27. Kondratyev, K. Ya. and Yu. M. Timofeev, "Numerical Experiments on Studying Transmission Functions of Atmospheric Gases," in Radiation Including Satellite Techniques, Proceedings of WMO/IUGG Symposium, WMO Tech. Note 104 (1968).
28. Armstrong, B., "Analysis of the Curtis-Godson Approximation and Radiation Transmission Through Inhomogeneous Atmospheres," J. Atmos. Sci., Vol. 25 (1968), p. 312.
29. Zdunkowski, W. and W. Raymond, "Exact and Approximate Transmissio. Calculations for Homogeneous and Non-Homogeneous Atmospheres," Beitr zur Phys. der Atmos., Vol. 43 (1970), p. 185.
30. Cantor, D. and J. Evans, "On Approximation by Positive Sums of Powers," SIAM J. Appl. Math., (1970), Vol. 18, p. 380.
31. Penndorf, R., "Tables of the Refractive Index for Standard Air and the Rayleigh Scattering Coefficient for the Spectral Region Between .2 and 20  $\mu$ ," J. Opt. Soc., Amer., Vol. 47 (1957), p. 176.
32. Peck, E. and K. Reeder, "Dispersion of Air," J. Opt. Soc., Amer., Vol. 62 (1972), p. 958.
33. Gucker, F., et. al., "Intensity and Polarization of Light Scattered by Some Permanent Gases and Vapors," J. Chem. Phys., Vol. 50 (1969), p. 2526.
34. Dave, J., "Subroutines for Computing the Parameters of the Electromagnetic Radiation Scattered by a Sphere," IBM Program 360D-17.4002, IBM Scientific Center, Palo Alto, Calif. (1968).
35. Kattawar, G. and G. Plass, "Electromagnetic Scattering From Absorbing Spheres," Appl. Opt., Vol. 6 (1967), p. 1377.
36. Denman, H., W. Heller, and W. Pangonis, Angular Scattering Functions for Spheres, Wayne State Univ. Press, Detroit (1966).
37. Deirmendjian, "Tables of Mie Scattering Cross Sections and Amplitudes," Rand Report R-407-PR, Rand Corp., Santa Monica, Calif. (1963).

38. Irvine, W. and J. Pollack, "Infrared Optical Properties of Water and Ice Spheres," Icarus, Vol. 8 (1968), p. 324.
39. Rusk, A., D. Williams, and M. Querry, "Optical Constants of Water in the Infrared," J. Opt. Soc., Amer., Vol. 61 (1971), p. 895.
40. Robertson, C. and D. Williams, "Lambert Absorption Coefficients of Water in the Infrared," J. Opt. Soc., Amer., Vol. 61 (1971), p. 1316.
41. Querry, M., et. al., "Optical Constants in the Infrared for Aqueous Solutions of NaCl," J. Opt. Soc., Amer., Vol. 62 (1972), p. 349.
42. Twitty, J. and J. Weinman, "Radiative Properties of Carbonaceous Aerosols," J. Appl. Met., Vol. 10 (1970), p. 725.
43. Dalzell, W. and A. Sarofim, "Optical Constants of Soot and Their Application to Heat-Flux Calculations," J. Heat Transfer, (February 1969), p. 100.
44. Spitzer, W. and D. Kleinman, "Infrared Lattice Bands of Quartz," Phys. Rev., Vol. 121 (1961), p. 1324.
45. Volz, F., "Infrared Absorption by Atmospheric Aerosol Substances," JGR, Vol. 77 (1972), p. 1017.
46. Volz, F., "Infrared Refractive Index of Atmospheric Aerosol Substances," Appl. Opt., Vol. 11 (1972), p. 755.
47. Blanco, A. and G. Hoidale, "Infrared Absorption Spectra of Atmospheric Dust," ECOM-5193, 1968, Atmospheric Sciences Lab, White Sands Missile Range, New Mexico.
48. Flanigan, D. and H. DeLong, "Spectral Absorption Characteristics of the Major Components of Dust Clouds," EATR-4430, 1970, Edgewood Arsenal, Maryland.
49. Hunt, J., M. Wisherd, and L. Bonham, "Infrared Absorption Spectra of Minerals and Other Inorganic Compounds," Anal. Chem., Vol. 22 (1950), p. 1478.
50. Went, F., "On the Nature of Aitken Condensation Nuclei," Tellus, XVIII (1966), p. 549.
51. Junge, C. E., Air Chemistry and Radioactivity, Academic Press, New York (1963).

52. Deirmendjian, D., Electromagnetic Scattering on Spherical Polydispersions, Elsevier, New York (1969).
53. Khragian, ed., Cloud Physics, Israel Program for Scientific Translations, Jerusalem (1963), p. 83.
54. Germogenova, O. A., "Atmospheric Haze: A Review," Report 1821, Bolt Beranek and Newman, Cambridge, Mass. (1970).
55. Twomey, S., H. Jacobowitz, and H. Howell, "Light Scattering by Cloud Layers, J. Atmos. Sci., Vol. 24 (1967), p. 70.
56. Blifford, I. H., "Tropospheric Aerosols," JGR, Vol. 75 (1970), p. 3099.
57. Chang, D. and R. Wexler, "Meteorological Relationships to Tropospheric and Stratospheric Turbidity Profiles," AFCRL-70-0197, Air Force Cambridge Research Labs., Cambridge, Mass. (1970).
58. Kondratyev, K. Ya., et. al., "Aerosol Structure of the Troposphere and Stratosphere," WMO Technical Note No. 104, Radiation Including Satellite Techniques (1968).
59. Dufour, L., "The Atmospheric Aerosol," translated at Atmospheric Sciences Laboratory, White Sands Missile Range, New Mexico (1969).
60. Selezneva, E. S., Atmospheric Aerosols, translated and published for ESSA (now NOAA) by Indian National Scientific Documentation Center, New Delhi, India (1970).
61. Eltermann, L., "Parameters for Attenuation in the Atmospheric Windows for Fifteen Wavelengths," Appl. Opt., Vol. 3 (1964), p. 745.
62. Meszaros, A., "On the Variation of the Size Distribution of Large and Giant Atmospheric Particles as a Function of the Relative Humidity," Tellus, XVIII (1971), p. 436.
63. Hanel, G., "The Real Part of the Mean Complex Refractive Index and the Mean Density of Samples of Atmospheric Aerosol Particles," Tellus, XX (1968), p. 371.
64. Ralston, A. and H. Wilf, eds., Mathematical Methods for Digital Computers, Vol. II (1967), Wiley, New York.
65. Dave, J., "Effect of Coarseness of the Integration Increment on the Calculation of the Radiation Scattered by Polydispersed Aerosols," Appl. Opt., Vol. 8 (1969), p. 1161.

66. Dave, J., "Effect of Varying Integration Increment on the Computed Polarization Characteristics of the Radiation Scattered by Polydispersed Aerosols," Appl. Opt., Vol. 8 (1969), p. 2153.
67. Hansen, J., J. Atm. Sci., Vol. 26 (1969), p. 478.
68. Potter, J., "The Delta Function Approximation in Radiative Transfer Theory," J. Atm. Sci., Vol. 27 (1970), p. 943.
69. Grant, I. and G. Hunt, "Solution of Radiative Transfer Problems Using the Invariant  $S_n$  Method," Mon. Not. Roy. Astron. Soc., Vol. 141 (1968), p. 27.
70. Grant, I. and G. Hunt, "Discrete Space Theory of Radiative Transfer I. Fundamentals," Proc. Roy. Soc. Lond. A., Vol. 313 (1969), p. 183.
71. Grant, I. and G. Hunt, "Discrete Space Theory of Radiative Transfer II. Stability and Non-Negativity," Proc. Roy. Soc. Lond. A., Vol. 313 (1969), p. 199.
72. Grant, I. and G. Hunt, "Solution of Radiative Transfer Problems in Planetary Atmospheres," Icarus, Vol. 9 (1968), p. 526.
73. Hunt, G., "The Effect of Coarse Angular Discretization on Calculations of Radiation Emerging from A Model Cloudy Atmosphere," JQSRT, Vol. 11 (1971), p. 309.
74. McCleese, D., J. Margolis, and G. Hunt, "Laboratory Simulation of Absorption Spectra in Cloudy Atmospheres," Nature (Phys. Sci.), Vol. 233 (1971), p. 102.
75. Preisendorfer, R. W., Radiative Transfer on Discrete Spaces, Pergamon Press, Oxford (1965).
76. van de Hulst, H. C., "A New Look at Multiple Scattering," unpublished report (1963), NASA Inst. for Space Studies, New York.
77. Rybicki, G. and P. Usher, "The Generalized Ricatti Transformation as a Simple Alternative to Invariant Imbedding," Astrophys. J., Vol. 146 (1966), p. 871.
78. Lathrop, K. and B. Carlson, "Numerical Solution of the Boltzmann Transport Equation," J. Comp. Phys., Vol. 2 (1967), p. 173.
79. Krook, M. "On the Solution of Equations of Transfer I," Astrophys. J., Vol. 122 (1955), p. 488.



80. Gates, W. L., et. al., "A Documentation of the Mintz-Arakawa Two-Level Atmospheric General Circulation Model," Report R-877-ARPA, Rand (December 1971).
81. Green, A., Appl. Opt., Vol. 3 (1964), p. 203.
82. Weller, G., S. Bowling, K. Jayaweera, T. Ohtaki, S. Parker, G. Shaw, and G. Wendler, "Studies of the Solar and Terrestrial Radiation Fluxes Over Arctic Pack Ice," (1972), Geophysical Institute, University of Alaska, Fairbanks, Alaska.
83. Valley, S., ed., Handbook of Geophysics and Space Environments, McGraw-Hill, New York (1965).
84. Huschke, R., "Arctic Cloud Statistics from 'Air-Calibrated' Surface Weather Observations," RAND Memorandum RM-6173-PR (1969), The RAND Corporation, Santa Monica, California.
85. "Inadvertent Climate Modification: Report of the Study of Man's Impact on Climate (SMIC)," (1971), MIT Press, Cambridge, Mass.